Improved Neoclassical Transport Simulation for Helical Plasmas

BOTSZ HUANG

Doctor of Philosophy

Department of Fusion Science
School of Physical Sciences
SOKENDAI (The Graduate University for Advanced Studies)

SOKENDAI (The Graduate University for Advanced Studies)
School of Physical Sciences
Department of Fusion Science

Improved Neoclassical Transport Simulation for Helical Plasmas

BOTSZ HUANG

Submitted in partial fulfilment of the requirements for the degree of
Doctor of Philosophy of SOKENDAI and
School of Physical Sciences, January 2017

Contents

List of Tables

List of Figures

Chapter 1

Introduction

Thermonuclear fusion is a candidate for the relatively steady and sustainable energy source because fusion power is not restricted by weather unlike renewable energy, such as photovoltaic power, and its fuels are abundantly present in seawater. There are two typical styles of thermonuclear fusion reactor: tokamak and stellarator/heliotron. Tokamak is a toroidally symmetric device and the coil system is simpler than a stellarator/heliotron. The large toroidal current in tokamak is necessary to sustain the magnetohydrodynamic (MHD) equilibrium magnetic field, which confines the plasma. On the other hand, stellarator/heliotron has an advantage for steady-state operation because only the coil systems can maintain its confinement magnetic field. For the design of helical reactor that sufficiently satisfies the fusion triple product, the optimization of the field geometry is necessary, as follows: (1) minimize the neoclassical and turbulent transport, (2) stabilize the magnetohydrodynamics (MHD) equilibrium, (3) improve the fast particle confinement, and (4) mitigate the heat load to the divertor.

In toroidal magnetic plasmas, the guiding-center motion of charged particles and Coulomb collisions give rise to a characteristic diffusion process, which is called neoclassical transport. The neoclassical transport in helical plasmas depends strongly

on the magnetic geometry and the helical ripple enhances the neoclassical radial particle and energy transport. In the helical plasmas, the neoclassical transport is comparable to the turbulent transport. Therefore, the neoclassical transport analysis is important for the optimization of particle and energy confinement, and it is fundamental for designing the helical reactor.

The future fusion reactor planned as FFHR-d1 will be operated in the higher-β and temperature condition than that in the present experimental devices. In a collisionless and high pressure gradient plasma, the bootstrap current is supposed to be strong enough to affect the MHD equilibrium. The effect of the bootstrap current in FFHR-d1 has not been investigated yet.

Unfortunately, there is no exact analytical formula to calculate the bootstrap current in helical plasmas and it is difficult to diagnose the current experimentally. To design and optimize a helical fusion reactor, a self-consistent method is required to track the interaction between MHD equilibrium and bootstrap current. Both good efficiency and reliability in the neoclassical simulation is required to conduct a quantitative study.

The global neoclassical model has been developed in recent decades. Though it is accurate and reliable because of minimum approximations considered in solving the drift-kinetic equation, it requires immense amounts of computing resources. On the other hand, the local neoclassical models discussed below resolve the computing resource problem, but their reliability is still in question. The quantitative precision of the local models has not been examined in detail yet.

The motivation of this work are shown as follows: (1)Benchmark of the Neoclassical Transport Models and Clarify the Impact of Several Approximations on Drift-Kinetic Equation in the Evaluation of Neoclassical Transport in Helical Plasmas. (2)Apply the Local Models for a Quantitative Evaluation of Bootstrap Current in a FFHR-d1 DEMO.

This work is composed of two parts as follows. (1) In part 1, it performs the benchmark of neoclassical parallel flow between the conventional and the new model (ZOW) in LHD, HSX, and W7-X. (2) In part 2, it demonstrates the the parallel momentum conservation on the bootstrap current by the benchmarks between the ZOW and PENTA models. Then, it verifies the reliability of the bootstrap current calculation with the ZOW and PENTA models for FFHR-d1 and axisymmetirc tokamaks.

Part I

Verification of the Neoclassical Transport Models in Helical Plasmas

Chapter 2

Introduction

The magnetic field geometry of a fusion device is given by the external coil system and the plasma current. One of the advantages of stellarator/heliotron configuration compared to asymmetric tokamaks is that plasma current is not necessary to sustain the confinement magnetic field. However, owing to the geometry, the helical ripple enhances the neoclassical radial particle and energy transport. Therefore, optimization of the field geometry is required for minimizing the neoclassical transport together with stabilizing the magnetohydrodynamics (MHD) equilibrium and improving the fast particle confinement.[13] The future fusion device will be operated in the higher-beta and higher-temperature condition compared to that in the present experimental devices. In such a collisionless and high pressure gradient plasma, the neoclassical bootstrap current is supposed to increase enough to interact with the MHD equilibrium. A self-consistent algorithm is required to investigate both the optimization of the neoclassical transport and the MHD equilibrium. The algorithm must satisfy both the efficiency and the accuracy in order to evaluate a quantitative study for the design of a fusion reactor.

From this viewpoint, neoclassical transport in helical plasmas has been investigated by transport codes based on several local approximations, for example, DKES[46]

[15], GSRAKE[3], EUTERPE[8], and NEO-2[21] et al. A comprehensive cross-benchmark of several local codes has been presented in Ref. [4] In the local models, the tangential grad-B and curvature drift on the flux surfaces is often assumed to be negligibly small compared to the parallel motion and $\boldsymbol{E} \times \boldsymbol{B}$ drift. Further, the mono-energy assumption is sometimes employed in the local neoclassical codes, in which the momentum conservation of the collision operator is broken because the Lorentz pitch-angle scattering operator is adopted. Note that momentum correction techniques by Taguchi[43], Sugama-Nishimura[42][39][38], and Maaßberg[28] have been devised to recover the parallel momentum balance. Several benchmarks have shown that the momentum correction affects the quantitative accuracy of neoclassical transport calculations in helical plasmas[28][44], especially in the quasi-axisymmetric HSX plasma.[27][6]

The recent studies have carried the contribution of the magnetic tangential drift[29][23][41] in the evaluation of radial neoclassical transport when the $\boldsymbol{E} \times \boldsymbol{B}$ drift velocity is slower than the magnetic drift. Matsuoka[29] has devised a way to include the tangential magnetic drift in the local drift-kinetic equation solver. There are also some global neoclassical codes which treat the full 3-dimensional guiding-center motion including both the radial and tangential magnetic drift term. However, only a few global neoclassical codes have been applied on helical plasmas.[35][33][45] Compared with the local codes, the global codes are stricter solutions to evaluate the drift-kinetic equation with the finite magnetic drift effect, but it takes more computational resources than the local codes. Therefore, it is almost impossible to utilize the global codes to investigate the interaction between bootstrap current and MHD equilibrium because it requires iterations between neoclassical transport and MHD simulations. The local approximations are appropriate for the purpose, but this has not been thoroughly verified among the neoclassical local models with global ones to guarantee the quantitative reliability of the neoclassical radial flux and parallel flow obtained from these local drift-kinetic models.

In Part I, following the previous study by Matsuoka[29], the neoclassical transport is examined with four types of neoclassical transport codes in Large Helical Device(LHD), Helically Symmetric Experiment(HSX), and Wendelstein 7-X(W7-X). The series of numerical simulations are carried out by the δf drift-kinetic equation solver FORTEC-3D. In the beginning, FORTEC-3D was developed as a global neoclassical transport code; recently, it has been extended to treat several types of the local drift-kinetic models[29]. The following approximations are employed to evaluate the neoclassical transport. (a) The global model takes the minimum assumption, which considers both the tangential and radial magnetic drift on the convective derivative term on the perturbed distribution, $\boldsymbol{v}_m \cdot \nabla \delta f$. The global model solves the drift-kinetic equation in 5-dimensional phase space. (b) The zero orbit width model (ZOW) excludes the radial component of magnetic drift, and it becomes a local neoclassical model. The magnetic drift term is treated as

$$\hat{\boldsymbol{v}}_m \equiv \boldsymbol{v}_m - (\boldsymbol{v}_m \cdot \nabla \psi)\boldsymbol{e}_\psi, \tag{2.1}$$

where ψ is a flux-surface label and $\boldsymbol{e}_\psi \equiv \partial \boldsymbol{X}/\partial \psi$. The *local* indicates the neglect of radial drift in the guiding-center equation of motion. Therefore, the ZOW model becomes a 4-dimensional model and reduces computational resources. However, the ZOW model breaks Liouville's theorem in the phase space. The ZOW model requires a modification in the delta-f method to solve the model properly as will be explained in Sec. 5.1. (c) The zero magnetic drift (ZMD) model takes a further approximation. The ZMD model ignores not only the radial magnetic drift but also the tangential magnetic drift from a particle orbit. Then, the magnetic drift term in the drift-kinetic equation is treated as $\boldsymbol{v}_m \cdot \nabla \delta f = 0$. Liouville's theorem is satisfied in the ZMD. (d) The DKES model further employs mono-energetic assumption, i.e., $\dot{v}(\partial \delta f/\partial) v = 0$, and the incompressible $\boldsymbol{E} \times \boldsymbol{B}$ drift approximation.[46][15] With the Lorentz pitch-angle scattering operator, the drift-kinetic equation in DKES model reduces to a 3-dimensional model.

The remainder of this work is organized as follows. In Sec.3,the drift kinetic equations based on global, ZOW, ZMD and DKES models are described. The conservation properties of the phase-space volume of each model is also discussed in this section. The particle, parallel momentum, and energy balance equations in each drift-kinetic model are examined in Sec.4. Furthermore, the derivation of viscosity tensor for each model is presented in Sec.A. Then, the numerical scheme of the δf method is explained briefly in Sec.5.1. In Sec.5.2 and 5.3, the linearized collision operators and the source/sink term are discussed, respectively. In Sec.6, the simulation results are presented. The drift-kinetic models are benchmarked by the neoclassical fluxes such as the radial particle flux, radial energy flux, and flux-surface average parallel mean flow. The effect of $\boldsymbol{E}\times\boldsymbol{B}$, the effect of magnetic drift, and the electron neoclassical transport are analyzed. Finally, the bootstrap current is presented. A summary is given in Sec.7.

Chapter 3

DRIFT-KINETIC MODELS

The neoclassical transport simulations are carried out by the δf method under the following transport ordering assumptions. The gyro-radius ρ is small compared with the typical scale length L, i.e., $\rho/L \sim \mathcal{O}(\delta)$, where δ represents a small ordering parameter. It is assumed that the plasma time evolution is slow,

$$\frac{\partial}{\partial t} \sim \mathcal{O}\left(\delta^2 \frac{v_{th}}{L}\right)$$

where $v_{th} = \sqrt{2T/m}$ is thermal velocity. The order of magnitude of the $\boldsymbol{E} \times \boldsymbol{B}$ drift velocity is assumed as

$$\frac{v_E}{v_{th}} \sim \mathcal{O}\left(\frac{\rho}{L}\right) \sim \mathcal{O}(\delta),$$

where the $\boldsymbol{E} \times \boldsymbol{B}$ drift velocity is given as

$$v_E \equiv \frac{|\boldsymbol{E} \times \boldsymbol{B}|}{B^2}.$$

The poloidal Mach number of $\boldsymbol{E} \times \boldsymbol{B}$ drift is defined as

$$\mathcal{M}_p \equiv \frac{v_E}{v_{th}} \frac{B}{B_p} \sim \frac{E_r}{v_{th} B_{ax}} \frac{q R_{ax}}{r} \tag{3.1}$$

where B_p and B_{ax} are the poloidal magnetic field strength and the magnetic field strength on the magnetic axis, respectively. The minor radius, the major radius of the magnetic axis, and the safety factor are denoted as r, R_{ax}, and q, respectively. In the present work, the order of magnitude $\mathcal{M}_p \sim 1$ for ions is allowed on the local drift-kinetic simulations because (a) the ion thermal velocity is much slower than the electron and (b) the order of the poloidal magnetic field magnitude is approximately

$$B_p \sim \frac{r}{qR_{ax}} B_{ax} \sim \mathcal{O}(\delta B).$$

Even though $\mathcal{M}_p \sim 1$ is allowed, it still assumes that the slow-flow ordering is valid, $v_E/v_{th} \ll 1$.

The guiding-center distribution function of species a is denoted as $f_a(\boldsymbol{Z}, t)$. The guiding-center variable $\boldsymbol{Z}$ are chosen as $\boldsymbol{Z} \equiv (\boldsymbol{X}, v, \xi; t)$ with the guiding-center position $\boldsymbol{X}$, guiding-center velocity v, and the cosine component of parallel velocity pitch-angle $\xi \equiv v_\parallel/v$. The parallel velocity $v_\parallel$ is defined as $v_\parallel \equiv \boldsymbol{v} \cdot \boldsymbol{b}$ where $\boldsymbol{b} \equiv \boldsymbol{B}/|\boldsymbol{B}|$ is a unit vector of the magnetic field. In Boozer coordinates, the position vector $\boldsymbol{X}$ is assigned as $\boldsymbol{X} \equiv (\psi, \theta, \zeta)$, where ψ, θ, and ζ are toroidal magnetic flux, poloidal angle, and toroidal angles, respectively. The magnetic field $\boldsymbol{B}$ is given as

$$\begin{aligned} \boldsymbol{B} &= \nabla\psi \times \nabla\theta + \iota(\psi)\nabla\zeta \times \nabla\psi \\ &= I(\psi)\nabla\theta + G(\psi)\nabla\zeta + \beta^*(\psi, \theta, \zeta)\nabla\psi. \end{aligned}$$

where $\iota(\psi)$ is the rotational transform. The radial covariant component $\beta^*(\psi, \theta, \zeta)$ is assumed to be negligible because it does not influence the drift equation of motion up to the standard drift ordering $\mathcal{O}(\rho/L)$.

3.1 Liouville's Theorem

The guiding center drift-kinetic equation of species a is given by

$$\frac{\partial f_a}{\partial t} + \frac{dZ_i}{dt}\frac{\partial f_a}{\partial Z_i} = \mathcal{C}_a + \mathcal{S}_a, \tag{3.2}$$

where $\mathcal{C}_a$ is Coulomb collision operator and $\mathcal{S}_a$ is a source/sink term. The conservation law in the phase-space or Liouville's equation is presented as [26]

$$\frac{\partial \mathcal{J}}{\partial t} + \frac{\partial}{\partial Z_i}\left(\mathcal{J}\frac{dZ_i}{dt}\right) = \mathcal{J}\mathcal{G}. \tag{3.3}$$

Here, $\mathcal{J}$ represents the Jacobian of the phase space. $\mathcal{G}$ is given in order to generalize Liouville's equation to satify $\mathcal{G} \neq 0$. $\mathcal{G} = 0$ if the trajectory follows the guiding center Hamiltonian property. As the recent studies showed, the local drift-kinetic models are derived from approximation of the guiding center motion but do not satisfy the Hamiltonian. Therefore, $\mathcal{G} = 0$ is not guaranteed in general. For some local neoclassical models, the approximated guiding-center equations of motion dZ_i/dt are chosen ingeniously to maintain $\mathcal{G} = 0$. To consider a general case, $\mathcal{G} \neq 0$ is retained in the following derivation. Combining Eqs.(3.2) and (3.3), the conservative form of drift-kinetic equation is obtained as

$$\frac{\partial(\mathcal{J} f_a)}{\partial t} + \frac{\partial}{\partial Z_i}\left(\mathcal{J} f_a \frac{dZ_i}{dt}\right) = \mathcal{J}\left[\mathcal{C}_a + \mathcal{S}_a\right] + \mathcal{J} f_a \mathcal{G}, \tag{3.4}$$

which is used in taking the moments of drift-kinetic equation in Chapter 4.

3.2 Global Drift Kinetic Model

The original FORTEC-3D is a global drift-kinetic code of which guiding center motion satisfies the Hamiltonian property. In the FORTEC-3D model, the perturbed

distribution function is given as follows: the distribution function f_a is decomposed into a Maxwellian $f_{a,M}$ and perturbation $f_{a,1}$

$$f_{a,1}(\boldsymbol{X}, v, \xi, t) \equiv f_a(\boldsymbol{X}, v, \xi, t) - f_{a,M}(\psi, v), \tag{3.5}$$

where the local Maxwellian $f_{a,M}$ is defined as

$$f_{a,M} = n_a(\psi) \left(\frac{m_a}{2\pi T_a(\psi)} \right)^{3/2} \cdot \exp \left(- \frac{m_a v^2}{2T_a(\psi)} \right) \tag{3.6}$$

The drift-kinetic equation is treated as

$$\left(\frac{\partial}{\partial t} + \dot{\boldsymbol{Z}} \cdot \frac{\partial}{\partial \boldsymbol{Z}} \right) f_{a,1} = \mathcal{S}_{a,0} + \mathcal{C}^L(f_{a,1}) + \mathcal{S}_{a,1}, \tag{3.7}$$

where $\dot{\boldsymbol{Z}} = \frac{d}{dt}(\boldsymbol{X}, v, \xi)$ and $\mathcal{C}^L(f_{a,1})$ is a linearized Fokker-Planck collision operator

$$\mathcal{C}^L(f_a) = \sum_b \mathcal{C}(f_{a,M}, f_{b,1}) + \mathcal{C}(f_{a,1}, f_{b,M}). \tag{3.8}$$

$\mathcal{S}_{a,0}$ is the source/sink term which is is discussed in Sec.5.3. $\mathcal{S}_{a,1}$ is an additional source/sink term, which helps the numerical simulation to reach a quasi-steady state. The $\mathcal{S}_{a,1}$ is discussed in Sec. 4.1 and 4.2.

The guiding-center trajectory is given as follows:[26]

$$\dot{\boldsymbol{X}} = v\xi \boldsymbol{b} + \frac{1}{e_a B_\parallel^*} \boldsymbol{b} \times \left\{ m_a (v\xi)^2 \boldsymbol{b} \cdot \nabla \boldsymbol{b} + \mu \nabla B - e_a \boldsymbol{E}^* \right\}, \tag{3.9a}$$

$$\frac{dv}{dt} = \frac{e_a}{m_a v} \dot{\boldsymbol{X}} \cdot \boldsymbol{E}^* + \frac{\mu}{m_a v} \frac{\partial B}{\partial t}, \tag{3.9b}$$

$$\frac{d\xi}{dt} = -\frac{\xi}{v}\frac{dv}{dt} - \frac{\boldsymbol{b}}{m_a v} \cdot (\mu \nabla B - e_a \boldsymbol{E}^*) + \xi \frac{d\boldsymbol{X}}{dt} \cdot \boldsymbol{\kappa}, \tag{3.9c}$$

where, m_a and e_a denote the mass and charge of the species a. respectively. Fur-

thermore,

$$\mu \equiv \frac{m_a v^2}{2B}(1-\xi^2), \tag{3.10a}$$

$$\boldsymbol{A}^* \equiv \boldsymbol{A} + \frac{m_a v \xi}{e_a}\boldsymbol{b}, \tag{3.10b}$$

$$\boldsymbol{E}^* \equiv -\frac{\partial \boldsymbol{A}^*}{\partial t} - \nabla\Phi, \tag{3.10c}$$

$$\boldsymbol{B}^* \equiv \nabla \times \boldsymbol{A}^*, \tag{3.10d}$$

$$B_\parallel^* \equiv \boldsymbol{b}\cdot\boldsymbol{B}^*, \tag{3.10e}$$

$$\boldsymbol{\kappa} \equiv (\boldsymbol{b}\cdot\nabla)\,\boldsymbol{b}. \tag{3.10f}$$

The trajectory is derived from Hamiltonian so that it satisfies the Liouville equation, i.e.,

$$\mathcal{J}\mathcal{G} = 0 \tag{3.11}$$

Note that the phase-space Jacobian in Boozer coordinates is

$$\mathcal{J} = \frac{2\pi B_\parallel^* v^2}{B}\frac{G+\iota I}{B^2}. \tag{3.12}$$

3.3 Zero Orbit Width Model (ZOW)

The zero orbit width (ZOW) approximation[29] is a local drift-kinetic model, which ignores only the radial drift $\dot{\psi}\,\partial f_1/\partial\psi$. The subscript of particle species is omitted here and hereafter unless it is necessary. The drift-kinetic equation Eq.(3.7) becomes

$$\left(\frac{\partial}{\partial t} + \dot{\boldsymbol{Z}}^{\mathrm{zow}}\cdot\frac{\partial}{\partial \boldsymbol{Z}}\right) f_1 = \mathcal{S}_0 + \mathcal{C}^L(f_1) + \mathcal{S}_1 \tag{3.13}$$

where $\dot{\boldsymbol{Z}}^{\mathrm{zow}} = \frac{d}{dt}(\theta,\zeta,v,\xi)$. In the present study, stationary electromagnetic field approximation is assumed

$$\frac{\partial B}{\partial t} = \frac{\partial \Phi}{\partial t} = 0. \tag{3.14}$$

Thus, the electric field is approximated as

$$\boldsymbol{E}^* \simeq -\nabla\psi\frac{d\Phi}{d\psi} \tag{3.15}$$

where $\Phi = \Phi(\psi)$ is the electrostatic potential, which is assumed to be a flux-surface function for simplicity. Other approximations employed in local models are $\boldsymbol{B}^* \cdot \boldsymbol{b} \simeq B$ and

$$\boldsymbol{\kappa} \simeq \frac{\nabla_\perp B}{B}. \tag{3.16}$$

Here, the $\mathcal{O}(\delta)$ correction in $B^*_\parallel$ is neglected. When $\beta \equiv p/(B^2/2\mu_0)$, one has

$$\begin{aligned}
\boldsymbol{\kappa} &= \boldsymbol{b} \times \left(\frac{\nabla B \times \boldsymbol{B}}{B^2} - \frac{\nabla \times \boldsymbol{B}}{B} \right) \\
&= \frac{1}{B}\left(\nabla B - \boldsymbol{b}\cdot\nabla B\right) + \mu_0 \frac{\boldsymbol{J}\times\boldsymbol{B}}{B^2} \\
&= \frac{\nabla_\perp B}{B} + \mu_0 \frac{\boldsymbol{J}\times\boldsymbol{B}}{B^2} \\
&= \frac{\nabla_\perp B}{B} + \frac{\mu_0 \nabla p}{B^2} \simeq \frac{\nabla_\perp B}{B} + \mathcal{O}(\beta)
\end{aligned} \tag{3.17}$$

where $p = p(\psi)$ denotes the scalar pressure. The second term is negligible in low-β approximation.

The particle trajectories $\dot{\boldsymbol{Z}}^{\text{zow}}$ are treated as if they are crawling on a specific flux surface and given as follows:

$$\dot{\boldsymbol{X}} = v\xi\boldsymbol{b} + \boldsymbol{v}_E + \hat{\boldsymbol{v}}_m, \tag{3.18a}$$

$$\dot{v} = \frac{-e_a}{m_a v}\boldsymbol{v}_m \cdot \nabla\psi\frac{d\Phi}{d\psi}, \tag{3.18b}$$

$$\begin{aligned}
\dot{\xi} = &-\frac{1-\xi^2}{2B}\left(v\boldsymbol{b}\cdot\nabla B\right) \\
&- \xi(1-\xi^2)\frac{d\Phi}{d\psi}\frac{\boldsymbol{B}\times\nabla B}{2B^3}\cdot\nabla\psi.
\end{aligned} \tag{3.18c}$$

Here, the $\boldsymbol{E}\times\boldsymbol{B}$ drift is defined as

$$\boldsymbol{v}_E \equiv \frac{d\Phi}{d\psi}\frac{\boldsymbol{B}\times\nabla\psi}{B^2} \tag{3.19}$$

and the magnetic drift is defined as

$$\boldsymbol{v}_m\cdot\nabla\psi \equiv \frac{m_a v^2}{2e_a B^3}\left(1+\xi^2\right)\boldsymbol{B}\times\nabla B\cdot\nabla\psi. \tag{3.20}$$

The radial virtual drift velocity $\dot{\psi}$ in the local model is evaluated from $\nabla\psi\cdot$ product of Eq. (3.20), and the tangential magnetic drift $\hat{\boldsymbol{v}}_m$ is defined as in Eq.(2.1),

$$\hat{\boldsymbol{v}}_m \equiv \boldsymbol{v}_m - \dot{\psi}\boldsymbol{e}_\psi.$$

The Jacobian of ZOW in phase space becomes

$$\mathcal{J} = \frac{2\pi B_\parallel^* v^2}{B}\frac{G+\iota I}{B^2} \simeq 2\pi v^2\frac{G+\iota I}{B^2}.$$

It should be pointed out that the magnetic drift velocity $\boldsymbol{v}_m$ is assumed to be the same order as the $\boldsymbol{E}\times\boldsymbol{B}$ drift, $\mathcal{O}(\delta v_{th})$. Therefore, the radial magnetic drift $\boldsymbol{v}_m\cdot\nabla\psi$ is still kept in the time evolution of velocity $\dot{v}$, which is also $\mathcal{O}(\delta)$. Even though the $\dot{\psi}\partial f_1/\partial\psi$ term is neglected in the LHS of Eq.(3.13), the source/sink term $S_0\propto\dot{\psi}$ in the RHS is the same as Eq.(5.9) in the global model.

The guiding-center equations of motion Eq.(3.18) do not include the radial drift term $\dot{\psi}$ and they do not satisfy Hamiltonian property. As a result, $\dot{\boldsymbol{Z}}^{\rm zow}$ is compressible on 4-dimensional phase space where

$$\mathcal{G} = \nabla_z\cdot\dot{\boldsymbol{Z}}^{\rm zow} = \frac{1}{\mathcal{J}}\frac{\partial}{\partial Z_i}\cdot(\mathcal{J}\dot{Z}_i) \neq 0. \tag{3.21}$$

Here, ∇_z represents the divergence in the phase space. Following (3.18) and (3.21),

the variation of phase-space volume along the guiding-center trajectories is

$$\nabla_z \cdot \dot{\boldsymbol{Z}}^{\text{zow}} = \frac{mv^2(1+\xi^2)}{2eB(G+\iota I)}\left\{\frac{3}{B}\frac{\partial B}{\partial \psi}\left(I\frac{\partial B}{\partial \zeta} - G\frac{\partial B}{\partial \theta}\right) + \left(G\frac{\partial^2 B}{\partial \psi \partial \theta} - I\frac{\partial^2 B}{\partial \psi \partial \zeta}\right)\right\}. \tag{3.22}$$

This term affects the balance equation of particle number, parallel momentum, and energy, which will be discussed in Chapter 4.

3.4 Zero Magnetic Drift Model (ZMD)

The zero magnetic drift (ZMD) model is similar to ZOW. It follows Eq.(3.18) but it excludes all the magnetic drift term in $\dot{\boldsymbol{X}}$. The particle trajectories of ZMD is given as the following:

$$\dot{\boldsymbol{X}} = v\xi \boldsymbol{b} + \boldsymbol{v}_E, \tag{3.23a}$$

$$\dot{v} = \frac{-e_a}{m_a v}\boldsymbol{v}_m \cdot \nabla\psi \frac{d\Phi}{d\psi}, \tag{3.23b}$$

$$\dot{\xi} = -\frac{1-\xi^2}{2B}\left(v\boldsymbol{b}\cdot\nabla B\right) - \xi(1-\xi^2)\frac{d\Phi}{d\psi}\frac{\boldsymbol{B}\times\nabla B}{2B^3}\cdot\nabla\psi. \tag{3.23c}$$

Following the ZMD 4-dimensional guiding-center orbit, the incompressibility of the phase-space volume $\mathcal{G} = 0$ is still retained.

3.5 DKES-like Model

The DKES-like model takes a further approximation on ZMD, that is, the mono-energetic assumption $\dot{v} = 0$. Then, the DKES-like model is reduced to be a 3-dimensional problem, in which $\dot{\boldsymbol{Z}}^{\text{dkes}} = d/dt(\psi, \theta, \zeta)$ on the LHS of the drift-kinetic

equation. Following the trajectory Eq.(3.23) and the mono-energetic particle approximation $\dot{v} = 0$, the phase space volume is not conserved:

$$\nabla_z \cdot \dot{\boldsymbol{Z}}^{\mathrm{dkes}} = \frac{3(1+\xi^2)}{2B^3\mathcal{J}}\left(G\frac{\partial B}{\partial \theta} - I\frac{\partial B}{\partial \zeta}\right)\frac{d\Phi}{d\psi}. \tag{3.24}$$

In order to maintain $\mathcal{G} = 0$, the electric potential $\nabla\Phi$ is replaced by

$$\nabla\Phi \simeq \nabla\Phi\frac{B^2}{\langle B^2\rangle} \tag{3.25}$$

and the incompressible $\boldsymbol{E}\times\boldsymbol{B}$ drift is denoted as

$$\hat{\boldsymbol{v}}_E \equiv \frac{\boldsymbol{E}\times\boldsymbol{B}}{\langle B^2\rangle}. \tag{3.26}$$

In summary, the guiding-center trajectory in the DKES-like model is given as follows:

$$\dot{\boldsymbol{X}} = v\xi\boldsymbol{b} + \hat{\boldsymbol{v}}_E, \tag{3.27a}$$

$$\dot{v} = 0, \tag{3.27b}$$

$$\dot{\xi} = -\frac{(1-\xi^2)v}{2B}\boldsymbol{b}\cdot\nabla B, \tag{3.27c}$$

and the particle trajectory conserves the phase space volume, $\mathcal{G} = \nabla_z \cdot \dot{\boldsymbol{Z}}^{\mathrm{dkes}} = 0$. Note that in Eqs.(3.27), v_E is the only $\mathcal{O}(\delta)$ term and the other terms are $\mathcal{O}(\delta^0)$. In the original DKES code, the collision operator is simplified by the Lorentz pitch-angle scattering operator

$$\mathcal{L}f_a = \frac{\nu_{ab}}{2}\frac{\partial}{\partial\xi}(1-\xi^2)\frac{\partial}{\partial\xi}f_a, \tag{3.28}$$

where the particle does not change the magnitude the velocity either by guiding-center motion or by collision. However, in the series of simulations in this work, all models use the same linear collision operator to benchmark neoclassical transport.

The linear collision operator includes the energy scattering term and field-particle part to maintain the conservation property of Fokker-Plank operator[35]. Between the original DKES and the DKES-like in the simulation, the effects of different collision operators appear in a quasi-symmetric geometry because of the conservation of momentum. It is essential to evaluate neoclassical transport as discussed in Sec. 6.1.

The properties of drift-kinetic models are summarized in the table below.

	Global	Local		
Model	FORTEC-3D	ZOW	ZMD	DKES-Like
Orbit	Full Orbit	$\hat{\boldsymbol{v}}_m \neq 0$	$\boldsymbol{v}_m = 0$	$\boldsymbol{v}_m = 0$
Dimensions	5	4	4	3
$\dot{\mu}$	$= 0$	$\neq 0$	$= 0$	$\neq 0$
$\mathbf{E} \times \mathbf{B}$ drift compressible?	Yes	Yes	Yes	No
$\nabla \cdot \dot{\boldsymbol{z}}$	$= 0$	$\neq 0$	$= 0$	$= 0$
$\dot{v}$				$= 0$

Table 3.1: The summary of the properties of the global and local drift-kinetic models

Chapter 4

Moments of the Drift-Kinetic Equation in the Models

In this chapter, the balance equations of particle number, parallel momentum, and energy are investigated for global and local models. The compressibility of phase space $\mathcal{G}$ and the approximations on guiding-center trajectories in each model are taken into account. The requirement of adaptive source-sink term S_1 is explained, which is essential for obtaining a steady-state solution in some models.

In order to take moments of Eq.(3.4), consider an arbitrary function $\mathcal{A}(\boldsymbol{X}, v, \xi, t)$ which is independent of the gyro-phase. For density variable $\int d^3v f\mathcal{A}$ in $\boldsymbol{X}$-space, the balance equation is yielded by multiplying $\mathcal{A}$ with Eq.(3.4) and taking integral over the velocity-space. By partial integral, Eq.(3.4) is rewritten as

$$\begin{aligned}
&\frac{\partial}{\partial t}\left(\int d^3v\ f_a\mathcal{A}\right) + \nabla\cdot\left(\int d^3v\ f_a\ \mathcal{A}\dot{\boldsymbol{X}}\right) \\
&= \int d^3v\ \left(f_a\frac{d\mathcal{A}}{dt} + \left[\mathcal{C}_a + \mathcal{S}_{a,1}\right]\mathcal{A}\right) \\
&+ \int d^3v\ f_a\mathcal{G}\mathcal{A}, \qquad (4.1)
\end{aligned}$$

where the integral of velocity-space is given as

$$\int d^3v = 2\pi \int dv v^2 \int d\xi.$$

Furthemore, the following equation is employed to derive Eq.(4.1)

$$\frac{d\mathcal{A}}{dt} \equiv \left(\frac{\partial}{\partial t} + \dot{\boldsymbol{Z}} \cdot \frac{\partial}{\partial \boldsymbol{Z}} \right) \mathcal{A}.$$

4.1 The Particle and Energy Balance on the Local DKE Models

In order to derive the conservation law of particle number, substituting $\mathcal{A} = 1$ into Eq.(4.1) yields

$$\begin{aligned} &\frac{\partial}{\partial t} \left(\int d^3v \ f_a \right) + \nabla \cdot \left(\int d^3v \ f_a \dot{\boldsymbol{X}} \right) \\ &= \int d^3v \ \mathcal{S}_a + \int d^3v \ f_a \mathcal{G} \end{aligned} \tag{4.2}$$

where $\int d^3v \ \mathcal{C}_a = 0$ is used. The continuity equation is obtained as

$$\frac{\partial n_a}{\partial t} + \nabla \cdot (n_a \boldsymbol{V}_a) = \int d^3v \ \mathcal{S}_a + \int d^3v f_a \mathcal{G}. \tag{4.3}$$

The density n_a and the mean flow velocity $n_a \boldsymbol{V}_a$ are defined as

$$n_a \equiv \int d^3v \ f_a, \tag{4.4a}$$

$$n_a \boldsymbol{V}_a \equiv \int d^3v \ \dot{\boldsymbol{X}} f_a. \tag{4.4b}$$

The balance of kinetic energy is obtained by substituting $\mathcal{A} = \mathcal{K}$ into Eq.(4.1),

$$\begin{aligned}
&\frac{\partial}{\partial t}\left(\int d^3v \ f_a \mathcal{K} \right) + \nabla \cdot \left(\int d^3v \ f_a \mathcal{K} \dot{\boldsymbol{X}} \right) \\
&= \int d^3v \left(f_a \frac{d\mathcal{K}}{dt} + \left[\mathcal{C}_a + \mathcal{S}_a \right] \mathcal{K} \right) \\
&+ \int d^3v \ f_a \mathcal{G} \mathcal{K}.
\end{aligned} \tag{4.5}$$

Here the kinetic energy $\mathcal{K}$ is defined as

$$\mathcal{K} \equiv \frac{1}{2} m_a {v_\parallel}^2 + \mu B = \mathcal{E} - e_a \Phi \tag{4.6}$$

where μ is the magnetic momentum, $\mathcal{E}$ is the total energy, and Φ is the electrostatic potential. The time derivative of the kinetic energy is denoted as

$$\begin{aligned}
\frac{d\mathcal{K}}{dt} &= \frac{d\mathcal{E}}{dt} - e_a \frac{d\Phi}{dt} \\
&= \mu \frac{\partial B(\boldsymbol{X}, t)}{\partial t} + e_a \boldsymbol{E}^* \cdot \frac{d\boldsymbol{X}}{dt},
\end{aligned} \tag{4.7}$$

where $\boldsymbol{E}^*$ is defined in Eq.(3.10c). In the series of simulations, a stationary electromagnetic field approximation is employed, which is given in Eqs.(3.14) and (3.15). Therefore, Eq.(4.7) is approximated as

$$\frac{d\mathcal{K}}{dt} \simeq -e_a \frac{d\Phi}{dt} = -e_a \frac{d\boldsymbol{X}}{dt} \cdot \nabla \Phi. \tag{4.8}$$

According to Eqs.(4.3), (4.25), and (4.5), if the Liouville theorem is violated, $\mathcal{G}$ affects the particle, momentum, and energy balance. The approximated trajectories and balance equations in the local models are presented in the following subsections.

The flux-surface-average is denoted as

$$\langle \mathcal{A} \rangle \equiv \frac{\int d\theta d\zeta \ \mathcal{J} \mathcal{A}}{\mathcal{V}'}, \tag{4.9}$$

where $\mathcal{A}$ is an arbitrary function and $\mathcal{V}'$ is defined as

$$\mathcal{V}' \equiv \frac{d\mathcal{V}}{d\psi} = \int d\theta d\zeta \ \mathcal{J}. \tag{4.10}$$

The particle density from f_1 is denoted as

$$\mathcal{N}_1 \equiv \int d^3v \ f_1(\boldsymbol{Z}). \tag{4.11}$$

The subscript of particle species is omitted here and hereafter unless it is necessary. According to continuity equation Eq.(4.3), the time evolution of density is

$$\begin{aligned} &\frac{\partial \langle \mathcal{N}_1 \rangle}{\partial t} + \left\langle \nabla \cdot \left(\mathcal{N}_1 \boldsymbol{V} \right) \right\rangle \\ &= \left\langle \int d^3v \ \mathcal{S}_1 \right\rangle + \left\langle \int d^3v \ f_1 \ \mathcal{G} \right\rangle. \end{aligned} \tag{4.12}$$

After taking the flux-surface-average, the contribution of $\mathcal{S}_0$ is zero because the source/sink term is a Maxwellian Eq.(3.6) with flux-surface functions n and T. Note here that in the global model the particle flow $\mathcal{N}_1 \boldsymbol{V}$ contains the radial component and $\mathcal{G} = 0$. Then, Eq.(4.12) for the global model becomes

$$\frac{\partial \langle \mathcal{N}_1 \rangle}{\partial t} + \frac{d}{d\mathcal{V}} \left(\Gamma^{\psi} \mathcal{V}' \right) = \left\langle \int d^3v \mathcal{S}_1 \right\rangle, \tag{4.13}$$

where the particle flux is calculated by

$$\Gamma^{\psi} \equiv \left\langle \int d^3v \ f_1 \dot{\psi} \right\rangle, \tag{4.14}$$

and the following identity is employed

$$\langle \nabla \cdot \boldsymbol{A} \rangle = \frac{d}{d\mathcal{V}} \langle \boldsymbol{A} \cdot \nabla \mathcal{V} \rangle = \frac{1}{\mathcal{V}'} \frac{d}{d\psi} \langle \mathcal{V}' \boldsymbol{A} \cdot \nabla \psi \rangle. \tag{4.15}$$

The finite $d(\Gamma^{\psi}\mathcal{V}')/d\mathcal{V}$ term is a corollary of global simulation in which the actual

radial particle flux across a flux surface is solved. Therefore, it is essentially required to include the particle source to obtain a steady-state solution. On the other hand, in the three local models, the $\mathcal{N}_1\boldsymbol{V}$ term has only the tangential component to the flux surface. Therefore, the $\langle\nabla\cdot(\mathcal{N}_1\boldsymbol{V})\rangle$ term vanishes in ZOW, ZMD and DKES-like models. However, for ZOW, the artificial source/sink term $\mathcal{S}_1$ is required because of the compressibility $\mathcal{G}\neq 0$ [29],

$$\frac{\partial\langle\mathcal{N}_1\rangle}{\partial t}=\left\langle\int d^3v\ \mathcal{S}_1\right\rangle+\left\langle\int d^3v\ f_1\ \mathcal{G}\right\rangle. \tag{4.16}$$

According to Eq.(3.22), the last term in Eq.(4.16) is estimated as $\mathcal{O}(\delta^2)$. For ZMD and DKES-like, the particle density $\mathcal{N}_1$ is constant naturally without $\mathcal{S}_1$, as pointed out by Landreman,[23]

$$\frac{\partial\langle\mathcal{N}_1\rangle}{\partial t}=0. \tag{4.17}$$

The energy balance equation for each model is derived similarly, as follows. The energy flux is introduced as

$$\boldsymbol{Q}\equiv\int d^3v f_1\mathcal{K}\dot{\boldsymbol{X}}, \tag{4.18}$$

and the flux-surface-average of radial energy flux is defined as

$$Q^{\psi}\equiv\left\langle\int d^3v f_1\mathcal{K}\dot{\psi}\right\rangle. \tag{4.19}$$

The pressure perturbation on flux surface is given as

$$P_1\equiv\frac{2}{3}\int d^3v f_1\mathcal{K}. \tag{4.20}$$

According to balance of kinetic energy Eq.(4.5), the time evolution of P_1 is rewritten

as

$$\begin{aligned}&\frac{3}{2}\frac{\partial}{\partial t}\langle P_1\rangle + \langle \nabla\cdot\boldsymbol{Q}\rangle \\ &= \left\langle \int d^3v\ f_1\ \frac{d\mathcal{K}}{dt}\right\rangle + \left\langle \int d^3v\ \mathcal{S}_1\ \mathcal{K}\right\rangle \\ &+ \left\langle \int d^3v\ f_1\ \mathcal{G}\ \mathcal{K}\ \right\rangle. \end{aligned} \tag{4.21}$$

In Eq.(4.21), the contribution from $\mathcal{S}_0$ vanishes again. The energy exchange by collision is omitted because we neglect the ion-electron collision and the electron-ion collision is approximated by pitch-angle scattering in the simulations. In the RHS of Eq.(4.21), the time evolution of kinetic energy is approximated as

$$\begin{aligned}&\left\langle \int d^3v\ f_1\ \frac{d\mathcal{K}}{dt}\right\rangle \\ &\simeq eE_\psi \left\langle \int d^3v\ \dot{\psi}\ f_1\right\rangle = eE_\psi\ \Gamma^\psi, \end{aligned} \tag{4.22}$$

which represents the work done by the radial current. For the global model, the finite $\langle \nabla\cdot\boldsymbol{Q}\rangle = d(Q^\psi \mathcal{V}')/d\mathcal{V}$ remains as in Eq.(4.13). Therefore, an energy source $\mathcal{S}_1\mathcal{K}$ is essentially required to reach a steady-state. On the other hand, the radial energy flux Q^ψ vanishes in the local models. For the ZOW and ZMD models, $\mathcal{S}_1\mathcal{K}$ is required to satisfy the balance equation of energy because of $d\mathcal{K}/dt$ and $\mathcal{G}$

$$\begin{aligned}\frac{3}{2}\frac{\partial}{\partial t}\langle P_1\rangle &= \left\langle \int d^3v\ \mathcal{S}_1\ \mathcal{K}\right\rangle \\ &+ eE_\psi\ \Gamma^\psi + \left\langle \int d^3v\ f_1\ \mathcal{G}\ \mathcal{K}\ \right\rangle \end{aligned} \tag{4.23}$$

where $\mathcal{G}$ appears only in the ZOW model. Eq.(4.23) indicates that ZMD cannot maintain the conservation law on energy when $E_\psi \neq 0$, even if it holds the constant particle number in Eq.(4.17). Finally, DKES-like maintains the energy balance without $\mathcal{S}_1\mathcal{K}$ because of $d\mathcal{K}/dt = 0$ and $\mathcal{G} = 0$.

Recently, Sugama has derived another type of ZOW model[41] in which guiding-

center variables are chosen as $(\boldsymbol{X}, v_\parallel, \mathcal{K})$ and the tangential magnetic drift is defined as

$$\hat{\boldsymbol{v}}_m = \boldsymbol{v}_m - \frac{(\boldsymbol{v}_m \cdot \nabla\psi)}{|\nabla\psi|^2}\nabla\psi. \tag{4.24}$$

In this model, the magnetic moment μ is allowed to vary in time so that the kinetic energy $\mathcal{K}$ is conserved. It is shown that the new local model satisfies both particle and energy balance relations without source/sink term. Although such a conservation property is desirable as a drift-kinetic model, we employ Matsuoka's ZOW model here for two reasons. First, the definition of tangential magnetic drift as in Eq. (4.24) requires the geometric factor $|\nabla\psi|^2$ on each marker's position, which will increase the computation cost. Second, it is necessary to find a modified Jacobian with which the phase-space volume conservation is recovered in this local model. To obtain such a modified Jacobian, another differential equation as Eq. (84) in Ref. [41] is required to be solved. Instead, in this work, we adopt the source/sink term in ZOW and ZMD models after the verification as discussed in Sec. 5.3. The verification shows that the source/sink term does not affect the long-term time average value of neoclassical fluxes after the simulation reaches a quasi-steady state.

4.2 The Parallel Momentum Balance and Parallel Flow

he parallel momentum balance equation is derived from Eq.(4.1) with $\mathcal{A} = m_a v_\parallel$, [41]

$$\begin{aligned}
&\frac{\partial}{\partial t}(n_a m_a V_{a,\parallel}) + \boldsymbol{b}\cdot(\nabla\cdot\boldsymbol{P}_a) \\
&= n_a e_a E_\parallel + F_{\parallel,a} + \int d^3v\ \mathcal{S}_a m_a v_\parallel \\
&+ \int d^3v\ f_a \mathcal{G} m_a v_\parallel,
\end{aligned} \tag{4.25}$$

where $E_\parallel = \boldsymbol{b}\cdot\boldsymbol{E}$ and $\boldsymbol{P}_a$ is the pressure tensor. The parallel friction of collision $F_{a,\parallel}$ is given as

$$F_{a,\parallel} \equiv \boldsymbol{b}\cdot\sum_{b\neq a}\boldsymbol{F}_{ab} = \sum_{b\neq a}\int d^3v\ \mathcal{C}_{ab}(f_a, f_b)m_a v_\parallel. \tag{4.26}$$

In order to derive Eq.(4.25), the expression of the time derivative of the parallel velocity $\dot{v}_\parallel$ is required. For the global model, it is given as

$$\dot{v}_\parallel = -\frac{1}{m}\boldsymbol{b}\cdot(\mu\nabla B - e\boldsymbol{E}^*) + v_\parallel\dot{\boldsymbol{X}}\cdot\boldsymbol{\kappa} \tag{4.27}$$

following the particle orbit Eqs.(3.9) and (3.10f). We substitute Eq.(4.27) into the parallel momentum equation Eq.(4.1). The pressure tensor $\boldsymbol{P}$ includes the diagonal component, the Chew-Goldbeger-Low (CGL) tensor $\boldsymbol{P}_{\rm CGL}$, and the $\boldsymbol{\Pi}_2$ term, the viscosity tensor $\boldsymbol{\Pi}_2$. See Appendix A for the derivation. According to the δf method, the viscosity tensors become

$$\begin{aligned}
&\boldsymbol{b}\cdot\nabla\cdot\boldsymbol{P}_{\rm CGL}\\
&= \boldsymbol{b}\cdot\nabla\cdot\left[\int d^3v\ \Big(\big(\ mv_\parallel^2\ \boldsymbol{bb} + \mu B\ (\boldsymbol{I}-\boldsymbol{bb})\big)\ f_1\right], &\text{(4.28a)}\\
&\boldsymbol{b}\cdot\nabla\cdot\boldsymbol{\Pi}_2\\
&= \boldsymbol{b}\cdot\nabla\cdot\left[\int d^3v\ mv_\parallel\ \left(\dot{\boldsymbol{X}}_\perp\boldsymbol{b} + \boldsymbol{b}\dot{\boldsymbol{X}}_\perp\right)f_1\right], &\text{(4.28b)}
\end{aligned}$$

where f_1 is an even function but $v_\parallel\dot{\boldsymbol{X}}_\perp$ is an odd function. Therefore, f_1 does not contribute to $\nabla\cdot\boldsymbol{\Pi}_2$. According to Eq.(4.28a), $\nabla\cdot\boldsymbol{P}_{\rm CGL}$ does not explicitly depend on the approximations in $\boldsymbol{v}_m$ and $\boldsymbol{v}_E$. Multiplying Eq.(4.25) with B, the flux-surface-average of the parallel momentum balance equation becomes

$$\begin{aligned}
&\left\langle\frac{\partial}{\partial t}(nmV_\parallel B)\right\rangle + \langle\boldsymbol{B}\cdot\nabla\cdot(\boldsymbol{P}_{\rm CGL}+\boldsymbol{\Pi}_2)\rangle\\
&= \langle neE_\parallel B\rangle + \langle F_\parallel B\rangle + \left\langle B\int d^3v\ \mathcal{S}_1\ mv_\parallel\right\rangle.
\end{aligned} \tag{4.29}$$

For the ZOW model, the parallel momentum balance equation is calculated with

$\dot{\boldsymbol{X}}_\perp = \boldsymbol{v}_E + \hat{\boldsymbol{v}}_m$ and the time derivative of parallel velocity

$$\begin{aligned}\dot{v}_\parallel &= -\frac{\mu}{m}\boldsymbol{b}\cdot\nabla B + v_\parallel \boldsymbol{v}_E \cdot \frac{\nabla_\perp B}{B} \\ &= -\frac{\mu}{m}\boldsymbol{b}\cdot\nabla B + v_\parallel \dot{\boldsymbol{X}}_\perp \cdot \boldsymbol{\kappa} + v_\parallel \left(\frac{\dot{\psi}}{B}\frac{\partial B}{\partial \psi}\right),\end{aligned} \tag{4.30}$$

following the particle orbit Eq.(3.18). Then, the parallel momentum balance equation becomes

$$\begin{aligned}&\left\langle \frac{\partial}{\partial t}(nmV_\parallel B)\right\rangle + \langle \boldsymbol{B}\cdot\nabla\cdot(\boldsymbol{P}_{\mathrm{CGL}} + \boldsymbol{\Pi}_{2,\mathrm{ZOW}})\rangle \\ &= \langle F_\parallel B\rangle + \left\langle B\int d^3v\ \mathcal{S}_1\ mv_\parallel\right\rangle \\ &+ \left\langle B\int d^3v\ f_1\ \mathcal{G}\ mv_\parallel\right\rangle \\ &- \left\langle \int d^3v\ mv_\parallel B\left(\frac{\dot{\psi}}{B}\frac{\partial B}{\partial\psi}\right) f_1\right\rangle.\end{aligned} \tag{4.31}$$

For the ZOW model, the $\boldsymbol{P}_{\mathrm{CGL}}$ term is the same form as Eq.(4.28a) and the $\boldsymbol{\Pi}_2$ term, Eq.(4.28b), is rewritten as

$$\begin{aligned}&\langle \boldsymbol{B}\cdot\nabla\cdot\boldsymbol{\Pi}_{2,\mathrm{ZOW}}\rangle \\ &= \left\langle \boldsymbol{B}\cdot\nabla\cdot\left[mnV_\parallel(\boldsymbol{b}\boldsymbol{v}_E + \boldsymbol{v}_E\boldsymbol{b})\right]\right\rangle \\ &+ \left\langle \boldsymbol{B}\cdot\nabla\cdot\left[\int d^3v\ mv_\parallel\ \left(\hat{\boldsymbol{v}}_m\boldsymbol{b} + \boldsymbol{b}\hat{\boldsymbol{v}}_m\right) f_1\right]\right\rangle,\end{aligned} \tag{4.32}$$

where $\hat{\boldsymbol{v}}_m$ is defined by Eq.(2.1). Eq.(4.32) shows that $\boldsymbol{\Pi}_{2,\mathrm{ZOW}}$ includes not only the $\boldsymbol{E}\times\boldsymbol{B}$ drift but also the partial magnetic drift. In the ZOW model, there is an extra term in Eq.(4.31),

$$\left\langle \int d^3v\ mv_\parallel B\left(\frac{\dot{\psi}}{B}\frac{\partial B}{\partial\psi}\right) f_1\right\rangle \tag{4.33}$$

which comes from the last term of Eq.(4.30) and is estimated as $\mathcal{O}(\delta^2)$. Actually, the $\partial B/\partial\psi$ is $\mathcal{O}(\delta)$ terms in MHD-equilibrium of helical devices, and Eq.(4.33) becomes

$\mathcal{O}(\delta^3)$. Furthermore, there is an additional term on the RHS in Eq.(4.31),

$$\left\langle B \int d^3v \; f_1 \; \mathcal{G} \; m v_\parallel \right\rangle \tag{4.34}$$

which is estimated as $\mathcal{O}(\delta^2)$. The effect of Eq.(4.34) on the parallel flow will be discussed in Sec.6.2 below. Following the order of magnitude, the contribution of Eq.(4.32) and (4.34) are comparable in the parallel momentum equation Eq.(4.31). The parallel electric field $E_\parallel$ and its contribution to the parallel momentum balance are neglected in the local models for simplicity.

For the ZMD model, the parallel momentum balance equation is calculated with $\dot{\boldsymbol{X}}_\perp = \boldsymbol{v}_E$ and the time derivative of parallel velocity

$$\begin{aligned} \dot{v}_\parallel &= -\frac{\mu}{m}\boldsymbol{b}\cdot\nabla B + v_\parallel \boldsymbol{v}_E \cdot \frac{\nabla_\perp B}{B} \\ &= -\frac{\mu}{m}\boldsymbol{b}\cdot\nabla B + v_\parallel \dot{\boldsymbol{X}}_\perp \cdot \boldsymbol{\kappa}, \end{aligned} \tag{4.35}$$

following the particle orbit Eq.(3.23). If the scalar pressure is assumed as a function of $p = p(\psi)$, $\nabla_\perp B/B \cdot \boldsymbol{v}_E$ is rewritten as $\dot{\boldsymbol{X}}_\perp \cdot \boldsymbol{\kappa}$, according to Eq.(3.17). Then, the parallel momentum balance equation becomes

$$\begin{aligned} &\left\langle \frac{\partial}{\partial t}(nmV_\parallel B) \right\rangle + \langle \boldsymbol{B}\cdot\nabla\cdot(\boldsymbol{P}_{\mathrm{CGL}} + \boldsymbol{\Pi}_{2,\mathrm{ZMD}})\rangle \\ &= \langle F_\parallel B\rangle + \left\langle B \int d^3v \; \mathcal{S}_1 \; m v_\parallel \right\rangle. \end{aligned} \tag{4.36}$$

Equation (4.28b) for ZMD is rewritten as

$$\langle \boldsymbol{B}\cdot\nabla\cdot\boldsymbol{\Pi}_{2,\mathrm{ZMD}}\rangle = \left\langle \boldsymbol{B}\cdot\nabla\cdot\left[mnV_\parallel(\boldsymbol{b}\boldsymbol{v}_E + \boldsymbol{v}_E\boldsymbol{b})\right]\right\rangle \tag{4.37}$$

where $\boldsymbol{v}_m$ does not exist in $\boldsymbol{\Pi}_2$. Compared to the ZOW model, the ZMD model maintains not only $\mathcal{G} = 0$ but also there is no extra term in the parallel momentum balance equation.

For the DKES model, the parallel momentum balance equation is calculated with $\dot{\boldsymbol{X}}_\perp = \hat{\boldsymbol{v}}_E$ from Eq.(3.26) and the time derivative of parallel velocity

$$\dot{v}_\parallel = -\frac{\mu}{m}\boldsymbol{b}\cdot\nabla B, \tag{4.38}$$

following the particle orbit Eq.(3.27). Then, the parallel momentum balance equation becomes

$$\begin{aligned}&\left\langle \frac{\partial}{\partial t}(nmV_\parallel B)\right\rangle + \langle \boldsymbol{B}\cdot\nabla\cdot(\boldsymbol{P}_{\rm CGL}+\boldsymbol{\Pi}_{2,\rm DKES})\rangle \\ &= \left\langle F_\parallel B\right\rangle + \left\langle B\int d^3v\ \mathcal{S}_1\ mv_\parallel\right\rangle - \left\langle BnmV_\parallel \hat{\boldsymbol{v}}_E\cdot\boldsymbol{\kappa}\right\rangle.\end{aligned} \tag{4.39}$$

With the incompressible $\boldsymbol{E}\times\boldsymbol{B}$ flow, Eq.(4.28b) is rewritten as

$$\begin{aligned}&\langle \boldsymbol{B}\cdot\nabla\cdot\boldsymbol{\Pi}_{2,\rm DKES}\rangle \\ &= \left\langle \boldsymbol{B}\cdot\nabla\cdot\left[\frac{mnV_\parallel}{\langle B^2\rangle}(\boldsymbol{bE}\times\boldsymbol{B}+\boldsymbol{E}\times\boldsymbol{Bb})\right]\right\rangle.\end{aligned} \tag{4.40}$$

DKES maintains $\mathcal{G}=0$ but the extra term $\left\langle BnmV_\parallel\hat{\boldsymbol{v}}_E\cdot\boldsymbol{\kappa}\right\rangle$ appears in its parallel momentum balance equation.

The viscosity tensors are different among the ZOW, ZMD, and DKES-like models because of the approximation of incompressible $\boldsymbol{E}\times\boldsymbol{B}$ drift. The effect of incompressibility is discussed in Sec.6.1 below.

For the parallel momentum balance in all of the global and local models, the constraint imposed on the source/sink term $\mathcal{S}_1$ is that its contribution to parallel momentum should vanish;

$$\int d^3v\ \mathcal{S}_1 mv_\parallel = 0. \tag{4.41}$$

In fact, unlike the particle or energy balance relation, the drift-kinetic simulation reaches a steady state of parallel flow without any additional source/sink term. Note

that the parallel momentum source vanishes not by flux-surface averaging, but is set to be zero anywhere on a flux surface. The effect of parallel friction $F_{\parallel}$ and the finite-$\mathcal{G}$ terms on the parallel momentum are discussed in Chapter. 6.

Chapter 5

Two-Weight δf Scheme

5.1 Weight Functions in the δf Scheme

The two-weight δf scheme[17][35] is employed to solve the global and local drift-kinetic models derived in Section 3.2 - 3.5. In this section, the compressibility of phase space $\mathcal{G}$ and the approximations of each model are taken into account in the weight function. Then, the balance equations of particle number, parallel momentum and energy are investigated for each models. The requirement of adaptive source-sink term S_1 is explained which is essential for obtaining a steady-state solution in some models.

The distribution function f_a is decomposed into a Maxwellian $f_{a,M}$ and perturbation $f_{a,1}$

$$f_a(\boldsymbol{X}, v, \xi, t) = f_{a,M}(\psi, v) + f_{a,1}(\boldsymbol{X}, v, \xi, t). \tag{5.1}$$

A Maxwellian $f_{a,M}$ is defined as

$$f_{a,M} = n_a(\psi) \left(\frac{m_a}{2\pi T_a(\psi)} \right)^{3/2} exp \left(- \frac{m_a v^2}{2T_a(\psi)} + \frac{eZ_a m_a \Phi(\psi)}{T_a(\psi)} \right).$$

The drift-kinetic equation is performed as the following by Eq.(3.7)

$$\left(\frac{\partial}{\partial t}+\dot{\boldsymbol{X}}\cdot\nabla+\dot{v}\frac{\partial}{\partial v}+\dot{\xi}\frac{\partial}{\partial \xi}\right)f_a=\mathcal{C}(f_a,f_b)+\mathcal{S}_{a,1} \tag{5.2}$$

where $\mathcal{C}(f_a,f_b)$ and $\mathcal{S}_{a,1}$ are Coulomb collision operator and source/sink, respectively. The linearized Coulomb collision operator is employed

$$\begin{aligned}\mathcal{C}(f_a,f_b)=&\mathcal{C}(f_{a,M},f_{b,M})+\mathcal{C}(f_{a,M},f_{b,1})\\&+\mathcal{C}(f_{a,1},f_{b,M})+\mathcal{C}(f_{a,1},f_{b,1}),\end{aligned} \tag{5.3}$$

where the nonlinear term $\mathcal{C}(f_{a,1},f_{b,1})$ is to be omitted in the following derivation. According to Eq.(5.1) and (5.2), the drift-kinetic equation becomes

$$\left(\frac{\partial}{\partial t}+\dot{\boldsymbol{X}}\cdot\nabla+\dot{v}\frac{\partial}{\partial v}+\dot{\xi}\frac{\partial}{\partial \xi}\right)(f_{a,M}+f_{a,1})=\mathcal{C}(f_a,f_b)+\mathcal{S}_{a,1}. \tag{5.4}$$

According to the order estimation in Chapter 3, one has

$$\dot{\xi},\dot{\theta},\dot{\zeta}\sim\mathcal{O}(\delta^0)$$

while

$$\dot{\psi},\dot{v}\sim\mathcal{O}(\delta^1).$$

Then, the lowest-order of Eq.(5.4) becomes

$$\left(\frac{\partial}{\partial t}+\dot{\theta}\frac{\partial}{\partial \theta}+\dot{\zeta}\frac{\partial}{\partial \zeta}+\dot{\xi}\frac{\partial}{\partial \xi}\right)f_{a,M}=\mathcal{C}\left(f_{a,M},f_{b,M}\right). \tag{5.5}$$

According to Eq.(5.2), the derivative of perturbation part δf becomes

$$\left(\frac{\partial}{\partial t}+\dot{\boldsymbol{X}}\cdot\nabla+\dot{v}\frac{\partial}{\partial v}+\dot{\xi}\frac{\partial}{\partial \xi}\right)f_{a,1}=\mathcal{C}_T+\mathcal{C}_F+\mathcal{S}_{a,0}+\mathcal{S}_{a,1} \tag{5.6}$$

where the test particle collision operator $\mathcal{C}_T$ and the field particle collision operator

$\mathcal{C}_F$ [35][24] are defined as

$$\mathcal{C}_T \equiv \mathcal{C}(f_{a,1}, f_{b,M}), \tag{5.7}$$

$$\mathcal{C}_F \equiv \mathcal{C}(f_{a,M}, f_{b,1}), \tag{5.8}$$

and the source term is denoted as

$$\mathcal{S}_{a,0} \equiv -\left(\dot{v}\frac{\partial}{\partial \psi} + \dot{\psi}\frac{\partial}{\partial \psi}\right) f_{a,M}. \tag{5.9}$$

Following Eq.(5.6), an operator includes the total derivative along the particle trajectory and the test-particle collision is defined as

$$\begin{aligned} \frac{Df_1}{Dt} &\equiv \frac{\partial f_1}{\partial t} + \dot{\boldsymbol{Z}} \cdot \frac{\partial f_1}{\partial \boldsymbol{Z}} - \mathcal{C}_T(f_1) \\ &= \mathcal{S}_0 + \mathcal{S}_1 + \mathcal{C}_F \end{aligned} \tag{5.10}$$

The detail about the implementation of $\mathcal{C}_T$ and $\mathcal{C}_F$ is explained in Sec. 5.2.

Let us briefly explain the two-weight δf scheme in the case of $\mathcal{G} \neq 0$. The weight functions $\mathfrak{w}$ and $\mathfrak{p}$ are given as follows:

$$f_1(\boldsymbol{Z}) = g(\boldsymbol{Z})\mathfrak{w}(\boldsymbol{Z}) \tag{5.11a}$$

$$f_M(\boldsymbol{Z}) = g(\boldsymbol{Z})\mathfrak{p}(\boldsymbol{Z}) \tag{5.11b}$$

where $g(\boldsymbol{Z})$ is the marker distribution function.

According to Eqs.(3.3) and (3.4), the drift-kinetic equation of marker distribution $g(\boldsymbol{Z})$ is obtained

$$\frac{Dg}{Dt} = -g\ \mathcal{G}. \tag{5.12}$$

Eq.(5.10) is extended with Eq.(5.11a)

$$\frac{Df_1}{Dt} = \mathfrak{w}\frac{Dg}{Dt} + g\frac{D\mathfrak{w}}{Dt}. \tag{5.13}$$

Following (5.10), (5.12), and (5.13), the time evolution of the weight function $\mathfrak{w}$ is obtained

$$\begin{aligned}\dot{\mathfrak{w}} &= \frac{1}{g}\frac{Df_1}{Dt} - \frac{\mathfrak{w}}{g}\frac{Dg}{Dt} \\ &= \frac{\mathfrak{p}}{f_M}\Big(\mathcal{S}_0 + \mathcal{S}_1 + \mathcal{C}_F(f_M)\Big) + \mathfrak{w}\mathcal{G}\end{aligned} \tag{5.14}$$

Similarly, the time evolution of the weight function $\mathfrak{p}$ is obtained as follows:

$$\dot{\mathfrak{p}} = \frac{\mathfrak{p}}{f_M}\left(\dot{\boldsymbol{Z}}\cdot\frac{\partial}{\partial \boldsymbol{Z}}\right)f_M + \mathfrak{p}\mathcal{G}. \tag{5.15}$$

The time evolution of the weights $\mathfrak{w}$ Eq.(5.14) and $\mathfrak{p}$ (5.15) include $\mathcal{G}$ which is non-zero in the ZOW model only. The last term in Eqs.(5.14) and (5.15) is required so that the two-weight δf scheme is applicable to the case in which the phase-space volume is not conserved[17]. Note that $\dot{\boldsymbol{Z}}$ in RHS of Eq.(5.15) depends on the drift-kinetic models. For the global model, it is denoted as

$$\dot{\boldsymbol{Z}}\cdot\frac{\partial f_M}{\partial \boldsymbol{Z}} = -\mathcal{S}_0; \tag{5.16}$$

for ZOW and ZMD, it is denoted as

$$\dot{\boldsymbol{Z}}\cdot\frac{\partial f_M}{\partial \boldsymbol{Z}} = \dot{v}\frac{\partial}{\partial v}f_M; \tag{5.17}$$

for the DKES-like, due to $\dot{v} = 0$, $\dot{\psi} = 0$, and $\mathcal{G} = 0$, the weight function $\mathfrak{p}$ becomes constant as

$$\dot{\mathfrak{p}} = 0. \tag{5.18}$$

5.2 Collision Operator

The general Fokker-Planck collision operator is given as

$$\mathcal{C}_{ab}(f_a, f_b) = \frac{\partial}{\partial \boldsymbol{v}} \cdot \left[\boldsymbol{A}^{ab} f_a + \frac{\partial}{\partial \boldsymbol{v}} \cdot \left(\boldsymbol{D}^{ab} f_a \right) \right], \tag{5.19}$$

where

$$\boldsymbol{A}^{ab} \equiv -\frac{\langle \Delta \boldsymbol{v} \rangle^{ab}}{\Delta t} = \left(1 + \frac{m_a}{m_b} \right) K_{ab} \frac{\partial \varphi_b}{\partial \boldsymbol{v}} \tag{5.20}$$

and

$$\boldsymbol{D}^{ab} \equiv -\frac{\langle \Delta \boldsymbol{v} \boldsymbol{v} \rangle^{ab}}{2\Delta t} = -K_{ab} \frac{\partial^2 \psi_b}{\partial \boldsymbol{v}}. \tag{5.21}$$

The relative velocity is denoted as $\boldsymbol{u} \equiv \boldsymbol{v} - \boldsymbol{v}'$ and the Rosenbluth potential is given as

$$\varphi_b(\boldsymbol{v}) \equiv -\frac{1}{4\pi} \int \frac{1}{u} f_b(\boldsymbol{v}') d^3 v', \tag{5.22}$$

$$\psi_b(\boldsymbol{v}) \equiv -\frac{1}{8\pi} \int u f_b(\boldsymbol{v}') d^3 v'. \tag{5.23}$$

The collision operator Eq.(5.19) is written with the Rosenbluth potential to obtain

$$\mathcal{C}_{ab}(f_a, f_b) = K_{ab} \frac{\partial}{\partial \boldsymbol{v}} \cdot \left[\frac{m_a}{m_b} \frac{\partial \varphi_b}{\partial \boldsymbol{v}} f_a - \frac{\partial^2 \psi_b}{\partial \boldsymbol{v} \partial \boldsymbol{v}} \cdot \frac{\partial f_a}{\partial \boldsymbol{v}} \right], \tag{5.24}$$

where

$$K_{ab} = ln\Lambda \left(\frac{e_a e_b}{\epsilon_0 m_a} \right)^2 \tag{5.25}$$

5.2.1 Like-Species Collision

Following Eqs.(5.3), (5.7) and (5.8), Eq.(5.24) is divided into the test particle collision operator $\mathcal{C}_T(f_{a,1}, f_{a,M})$ and the field particle collision operator $\mathcal{C}_F(f_{a,M}, f_{a,1})$,

$$\mathcal{C}_T(f_{a,1}, f_{b,M}) = K_{ab}\frac{\partial}{\partial \boldsymbol{v}} \cdot \left[\frac{m_a}{m_b}\frac{\partial \varphi(f_{b,M})}{\partial \boldsymbol{v}} f_{a,1} - \frac{\partial^2 \psi(f_{b,M})}{\partial \boldsymbol{v}\partial \boldsymbol{v}} \cdot \frac{\partial f_{a,1}}{\partial \boldsymbol{v}}\right], \tag{5.26a}$$

$$\mathcal{C}_F(f_{a,M}, f_{b,1}) = K_{ab}\frac{\partial}{\partial \boldsymbol{v}} \cdot \left[\frac{m_a}{m_b}\frac{\partial \varphi(f_{b,1})}{\partial \boldsymbol{v}} f_{a,M} - \frac{\partial^2 \psi(f_{b,1})}{\partial \boldsymbol{v}\partial \boldsymbol{v}} \cdot \frac{\partial f_{a,M}}{\partial \boldsymbol{v}}\right]. \tag{5.26b}$$

In this subsection, we consider the case $a = b$ for the like-species collision operator. In Eq.(5.26a), for the test particle collision operator $\mathcal{C}_T$, the explicit analytic expressions of Rosenbluth potentials φ_a and ψ_a are available because there are integrals of known function $f_{a,M}$. In Eq.(5.26b), for the field particle collision operator $\mathcal{C}_F$, the derivative of Rosenbluth potentials φ_a and ψ_a requires differentiation and integral of $f_{a,1}$. This processes will introduce the numerical error in $\mathcal{C}_F$. Therefore, the field particle collision operator $\mathcal{C}_F$ is evaluated by the conservation law instead of Eq.(5.26b).

In the drift-kinetic theory, the distribution function f_1 is regarded as gyro-phase independent, $f_1 = f_1(\boldsymbol{X}, v_\parallel, v_\perp)$. By taking the gyro-phase average, the test particle collision operator Eq.(5.26a) can be rewritten as [25]

$$\begin{aligned}\mathcal{C}_T(f_{a,1}) = &\frac{\partial}{\partial v_\parallel}\left(\nu_{s,\parallel} f_{a,1}\right) + \frac{\partial}{\partial v_\perp^2}\left(\nu_{s,\perp} f_{a,1}\right) + \frac{\partial}{\partial v_\parallel \partial \nu_{\parallel,\perp}^2}\left(v_\perp f_{a,1}\right) \\ &+ \frac{1}{2}\frac{\partial^2}{\partial v_\parallel^2}\left(\nu_\parallel f_{a,1}\right) + \frac{1}{2}\frac{\partial^2}{(\partial v_\perp^2)^2}\left(\nu_\perp f_{a,1}\right)\end{aligned} \tag{5.27}$$

where the coefficients are defined as

$$\begin{aligned}\nu_{s,\parallel} &\equiv v_\parallel \mathfrak{F}, \\ \nu_{s,\perp} &\equiv v_\perp^2(2\mathfrak{F} - \mathfrak{H}) - (2v_\parallel^2 + v_\perp^2)\mathfrak{G}, \\ \nu_\parallel &\equiv v_\parallel^2 \mathfrak{H} + v_\perp^2 \mathfrak{G}, \\ \nu_\perp &\equiv 4v_\perp^2(v_\perp^2 \mathfrak{H} + v_\parallel^2 \mathfrak{G}), \\ \nu_{\parallel,\perp} &\equiv 2v_\perp^2 v_\parallel(\mathfrak{H} - \mathfrak{G}).\end{aligned} \tag{5.28}$$

The $\mathfrak{F}$, $\mathfrak{G}$, amd $\mathfrak{H}$ function are defined as

$$\mathfrak{F}(x) \equiv (1 + \frac{m_a}{m_b})\phi(x)\nu_0, \tag{5.29}$$

$$\mathfrak{G}(x) \equiv \nu_0 \left[\left(1 - \frac{1}{2x}\right) \phi(x) + \frac{d\phi(x)}{dx} \right], \tag{5.30}$$

$$\mathfrak{H}(x) \equiv \nu_0 \frac{1}{x} \phi(x) \tag{5.31}$$

where $x \equiv v^2/v_{th}^2$,

$$\phi(x) \equiv \frac{2}{\sqrt{\pi}} \int dt e^{-x'} \sqrt{x'}, \tag{5.32}$$

and

$$\nu_0 \equiv \frac{n_b e_a^2 e_b^2 ln\Lambda_{ab}}{4\pi\epsilon_0^2 m_a^2 v^3}. \tag{5.33}$$

Then, the test particle collision operator is carried out as

$$v_\parallel = v_{\parallel,0} - \nu_{s,\parallel}\Delta t + \sqrt{12\nu_\parallel \Delta t}(R_1 - 0.5), \tag{5.34}$$

$$v_\perp = v_{\perp,0}^2 - \nu_{s,\perp}\Delta t + \sqrt{12\Delta t \left(v_\perp - \frac{v_{\parallel,\perp}^2}{\nu_\parallel}\right)}(R_2 - 0.5) + \sqrt{12\nu_\parallel \Delta t}(R_1 - 0.5)\frac{\nu_{\parallel,\perp}}{\nu_\parallel} \tag{5.35}$$

where $R_1, R_2 \in [0, 1]$ are two independent uniform random numbers.

The field particle operator is defined so that it satisfy the fellowing relations [34], which are also satisfied by the original linearized operator, Eq.(5.26). First, it must satisfy the conservation properties

$$\int d^3v \ \mathfrak{M} \ [\mathcal{C}_T(f_a) + \mathcal{C}_F(f_{M,a})] = 0 \tag{5.36}$$

where the operator $\mathfrak{M}$ is defined as

$$\mathfrak{M} \equiv \left\{1, v_\parallel, v^2\right\}. \tag{5.37}$$

Second, the property is the adjointness of the linearized operator [22]. For the case of like-species collisions,

$$\int d^3v \frac{f_1}{f_M} \mathcal{C}_T(g_1) = \int d^3v \frac{g_1}{f_M} \mathcal{C}_T(f_1) \tag{5.38a}$$

$$\int d^3v \frac{f_1}{f_M} \mathcal{C}_F(g_1) = \int d^3v \frac{g_1}{f_M} \mathcal{C}_F(f_1) \tag{5.38b}$$

Third, the linearized collision operator can describe the H-theorem

$$\int d^3v \frac{f_1}{f_M} \left[\mathcal{C}_T(f_1) + \mathcal{C}_F(f_1)\right] \leq 0, \tag{5.39}$$

where the equality is satisfied when f_1 has the following form,

$$f_1 = \left(c_0 + c_1 v_\parallel + c_2 v^2\right) f_M \quad \textit{for } \forall c_i \in \mathbf{R}. \tag{5.40}$$

The form f_1 in the above equation also satisfy the null space of the linearized operator,

$$\mathcal{C}_T(f_1) + \mathcal{C}_F(f_1) = 0. \tag{5.41}$$

The field particle collision operator $\mathcal{C}_F$ which satisfies the conditions Eqs.(5.36) to (5.41) is given as follows:

$$\mathcal{C}_F = -\frac{1}{n}\left[aF(x) + b\xi G(x) + cH(x)\right] f_M. \tag{5.42}$$

The F, G, amd H function are defined as

$$F(x) \equiv 1 - 3\sqrt{\frac{\pi}{2x}}\left(\phi(x) - \phi(x)'\right), \tag{5.43a}$$

$$G(x) \equiv 3\sqrt{\frac{\pi}{2x}}\phi(x), \tag{5.43b}$$

$$H(x) \equiv 3\sqrt{\frac{\pi}{2x}}\left(\phi(x) - \phi(x)'\right). \tag{5.43c}$$

where $x \equiv v^2/v_{th}^2$ and $\phi(x)$ is defined in Eq.(5.32).

The coefficients (a, b, c) are determined by perturbation of particle number, momentum, and energy in $\mathcal{C}_T$

$$\{a, b, c\} = \left\{\delta n, \frac{2\delta P}{v_{th}}, \frac{2}{3}\frac{\delta E}{v_{th}^3}\right\} \tag{5.44}$$

$$\{\delta n, \delta P, \delta E\} = \int d^3v \{1, v_\parallel, v^2\} \mathcal{C}_T(\delta f_a). \tag{5.45}$$

The problem is that the coefficients (a, b, c) given by Eq.(5.44) are the solutions if there is no numerical or statistic error in Monte-Carlo method. In practice, the field particle operator cannot satisfy the conservation property with finite number of simulation markers. The practical solution which keep the conservation property is obtained by substituting (5.42), (5.44), and Eq.(5.45) into Eq.(5.36),

$$\begin{pmatrix} a \\ b \\ c \end{pmatrix} = -\sum_k \begin{pmatrix} F_k \mathfrak{p}_k & G_k \mathfrak{p}_k & H_k \mathfrak{p}_k \\ F_k x_k^{1/2} \xi_k \mathfrak{p}_k & G_k x_k^{1/2} \xi_k^2 \mathfrak{p}_k & H_k x_k^{1/2} \xi_k \mathfrak{p}_k \\ F_k x_k \mathfrak{p}_k & G_k x_k \xi_k \mathfrak{p}_k & H_k x_k \mathfrak{p}_k \end{pmatrix}^{-1} \cdot \begin{pmatrix} \delta n \\ \delta P/v_{th} \\ \delta E/v_{th}^2 \end{pmatrix} \tag{5.46}$$

where the summation is taken over markers (index k) within a small volume cell, and the abbreviations $F_k = F(x_k)$ and so on are used. By Eq.(5.46), the linearized collision operator satisfies the conservation law.

5.2.2 Unlike-Species Collision

If $m_a \ll m_b$, the gerneral collision operator is simplified as follows.[14] Assume the particle species a and b have the same order of magnitude of temperature, $T_b \sim T_a$ so that

$$v_{th,b} \ll v_{th,a}. \tag{5.47}$$

As a result, for the a species, the distribution of species b can be approximated as a delta function,

$$f_b(\boldsymbol{v}) \simeq n_b \delta(\boldsymbol{v} - \boldsymbol{V}_b) \tag{5.48}$$

where $\boldsymbol{V}_b$ is the average velocity of species b. Then,

$$\psi_b \simeq -\frac{n_b}{8\pi}|\boldsymbol{v} - \boldsymbol{V}_b| \simeq -\frac{n_b}{4\pi} v \left(1 - \frac{\boldsymbol{v}\cdot\boldsymbol{V}_b}{v^2}\right). \tag{5.49}$$

Then, when $\mathcal{C}_{ab}$ is linearized $\mathcal{C}_{ab} = \mathcal{C}_T + \mathcal{C}_F$ as Eqs.(5.26a) and (5.26b), the approximation $m_a \ll m_b$ is used for $\mathcal{C}_F$. It yields

$$\mathcal{C}_F(f_{a,M}, f_{b,1}) \simeq -\frac{n_b K_{ab}}{4\pi}\frac{m_a}{T_a}\frac{\boldsymbol{V}_b\cdot\boldsymbol{v}}{v^3} f_{M,a}. \tag{5.50}$$

In Eq.(5.50), the fist term in Eq.(5.26b) is neglected.

For $\mathcal{C}_T$, first, the gyro-phase average of Eq.(5.26a) is emplyed. It yields

$$\mathcal{C}_T(f_{a,1}, f_{b,M}) \equiv \nu_D^{ab}\mathcal{L} + \frac{1}{v^2}\frac{\partial}{\partial v}\left[v^3\left(\frac{m_a}{m_a+m_b}\nu_{ab,s} f_{a,1} + \frac{1}{2}\nu_{ab,\parallel} v \frac{v\partial f_{a,1}}{\partial v}\right)\right], \tag{5.51}$$

where the Lorentz scattering operator in spherical coordinates (r, θ, ϕ) is denoted as

$$\mathcal{L} \equiv \frac{1}{2}\left[\frac{1}{\sin\theta}\frac{\partial}{\partial\theta}\left(\sin\theta\frac{\partial f_a}{\partial\theta}\right) + \frac{1}{\sin^2\theta}\frac{\partial^2 f_a}{\partial\phi^2}\right]. \tag{5.52}$$

The slowing-down frequency ν_s^{ab}, deflection frequency ν_D^{ab}, and parallel velocity diffsion frequency $\nu_\parallel^{ab}$denoted as

$$\nu_D^{ab}(v) \equiv \frac{n_b}{4\pi v_{T_a}^3} K_{ab}\frac{\mathrm{erf}(y) - \mathcal{G}_{ch}(y_b)}{y_a^3}, \tag{5.53a}$$

$$\nu_s^{ab}(v) \equiv \frac{n_b}{4\pi v_{T_a}^3} K_{ab}\frac{T_a}{T_b}\left(1 + \frac{m_b}{m_a}\right)\frac{\mathcal{G}_{ch}(y_a)}{y_a}, \tag{5.53b}$$

$$\nu_\parallel^{ab}(v) \equiv 2\frac{n_b}{4\pi v_{T_a}^3} K_{ab}\frac{\mathcal{G}_{ch}(y_b)}{y_a^3}. \tag{5.53c}$$

where $y_b = v/v_{T_b}$, $\mathrm{erf}(y)$ is the error function, and $\mathcal{G}_{ch}$ is Chandrasekhar function,

$$\mathcal{G}_{ch}(y) \equiv \frac{\mathrm{erf}(y) - y[\mathrm{erf}(y)]'}{2y^2}. \tag{5.54}$$

If the large-mass-ration limit $m_a \ll m_b$ is assumed, $y_a \sim \mathcal{O}(1)$ and $y_b \sim \mathcal{O}(\sqrt{m_b/m_a}) \gg 1$. In this case, one can estimate as

$$\nu_{ab,D} \sim \frac{\mathrm{erf}(y_b)}{y_a^3} \sim \frac{1}{y_a^3}, \tag{5.55}$$

$$\frac{m_e}{m_e + m_i}\nu_{ab,s} \sim \frac{m_a}{m_b}\frac{1}{y_b y_a^2}, \tag{5.56}$$

$$\nu_{ab,\parallel} \sim \frac{\mathcal{G}_{ch}(y_b)}{y_a^3} \sim \frac{1}{y_b^3 y_a^2}, \tag{5.57}$$

which allows ones to neglect the second and third terms in Eq.(5.51)

Finally, the unlike-species collision operator in the large-mass-ratio limit is obtain as

$$\mathcal{C}_{ab} \simeq \nu_{ab,D}\left(\mathcal{L}(f_a) + \frac{m_a}{T_a}\frac{\boldsymbol{V}_b \cdot \boldsymbol{v}}{v^3} f_{M,a}\right). \tag{5.58}$$

Following Eqs.(5.52) and (5.51), the test particle operator $\mathcal{C}_T$ is rewritten as [30]

$$\begin{aligned}\mathcal{C}_T &= \nu_{ab,D}\mathcal{L}(f_a) \\ &= \frac{\nu_{ab,D}}{2}\left[\frac{\partial}{\partial \xi}(1+\xi)\frac{\partial^2 \delta f}{\partial \xi}\right].\end{aligned} \tag{5.59}$$

where the pitch angle of particle is denoted as $\xi \equiv v_\parallel/v$.

In this work, the Lorentz scattering operator in the Monte-Carlo simulation is carried out as follows. According to Eq.(5.59), in the numerical simulation the pitch angle ξ is presented as

$$\xi_n = \xi_{n-1}(1 - \nu_{ei,D}\tau) \pm \sqrt{1 - \xi_{n-1}^2 \nu_{ei,D}\tau} \tag{5.60}$$

where τ an n are a time step and an index of time step, respectively. Note that the sign, $\pm$, is given randomly with equal probability, and Eq.(5.60) is applied

for the markers which satisfy $\xi_{n-1}^2 \nu_{ei,D} \tau < 1$. For the slow markers which have $\xi_{n-1}^2 \nu_{ei,D} \tau \geq 1$, a random number $\xi_n \in (-1, +1)$ is given in each time step to mimic a large-angle scattering. Therefore, the pitch angle is restricted to $-1 < \xi < 1$ for any particles.

The field particle operator $\mathcal{C}_F$ is evolved with the weight function $\mathfrak{w}$

$$\begin{aligned} \mathcal{C}_F((f_{M,a}) &= \left[\frac{d}{dt} f_{a,1}\right]_{\mathcal{C}_F} \\ &= g_b\left(f_{M,a}\right) \dot{\mathfrak{w}} \\ &= \frac{n_b K_{ab}}{4\pi} \frac{m_a}{T_a} \frac{\boldsymbol{V}_b \cdot \boldsymbol{v}}{v^3} f_{M,a} \end{aligned} \tag{5.61}$$

where $f_{M,a}$ can be obtained by the weight function $\mathfrak{p}$, $f_{M,a} = \mathfrak{p} g_b\left(f_{M,a}\right)$. Then, the time derivative of weight function $\dot{\mathfrak{w}}$ is obtained by Eq.(5.61)

$$\dot{\mathfrak{w}} = \frac{n_b K_{ab}}{4\pi} \frac{m_a}{T_a} \frac{\boldsymbol{V}_b \cdot \boldsymbol{v}}{v^3} \mathfrak{p}. \tag{5.62}$$

In the part I, only the Lorentz scattering operator $\mathcal{L}_{ei}$ is employed in $\mathcal{C}_{ei}$ in order to carried out the simulations. In the part II, the $\boldsymbol{V}_{i,\parallel}$ is included in the simulations in order to present the importance of the parallel friction between electron and ion.

5.3 Source/Sink Term

As explained in Sec. 4.1 and 4.2, an adaptive source and sink term is introduced in the global and local FORTEC-3D codes. Thus, the flux-surface averaged density and pressure perturbation from the f_1 part, which are defined by Eqs. (4.11) and (4.20), become negligible compared to the background density and pressure, i.e., $\langle \mathcal{N}_1 \rangle \ll n$ and $\langle P_1 \rangle \ll nT$. Such a source/sink term is constructed according to the following considerations.

First, the source/sink term acts to reduce the flux-surface average perturbations $\langle \mathcal{N}_1 \rangle$ and $\langle P_1 \rangle$. It is considered that the source/sink term should **not** smoothen the spatial variation of them on the flux surface, because the non-uniform distribution reflects the compressible flow on the flux surface. Therefore, the source-sink term is constructed to reduce $\langle \mathcal{N}_1 \rangle$ and $\langle P_1 \rangle$, while it maintains the fluctuation patterns on the flux surface, $\mathcal{N}_1 - \langle \mathcal{N}_1 \rangle$ and $P_1 - \langle P_1 \rangle$. Second, the source-sink term should be adaptive. The strength of the source-sink term is proportional to $\langle \mathcal{N}_1 \rangle$ and $\langle P_1 \rangle$ so that the users do not have to control the strength of the source-sink term. Third, the source/sink term does not contribute as a parallel momentum source as shown in Eq.(4.41), because the steady-state parallel momentum balance can be found without giving an artificial source/sink term.

In the drift-kinetic equation for f_1 (5.10), the source-sink term S_1, which satisfies the conditions explained above, is given in the form $S_1 = s(\psi, v, \xi, t) f_M$ with the following constraints:

$$\begin{aligned} \int d^3v \; s f_M &= -\nu_S \langle \mathcal{N}_1 \rangle, \\ \int d^3v \; m_a v_\parallel s f_M &= 0, \\ \int d^3v \; \frac{m_a v^2}{2} s f_M &= -\frac{3}{2} \nu_S \langle P_1 \rangle, \end{aligned} \tag{5.63}$$

where ν_S is a numerical factor to control the strength of the adaptive source-sink term. There is arbitrariness to make a source/sink term which satisfies Eq.(5.63). The examples of the adaptive source/sink terms can be found in the references[23][20]. In FORTEC-3D code, the source/sink term is implemented by diverting the field-particle collision operator $\mathcal{C}_F f_M$, which is introduced in Sec. 5.2.1. The field-particle operator is made so as to satisfy the conservation laws for the like-particle linearized collision Eq.(5.36). By comparing Eqs. (5.63) and (5.36), one can see that operator $\mathcal{C}_F$ can be directly used to implement the source/sink term. In FORTEC-3D, the source/sink term is operated in the (θ, ζ) cells on a flux-surface which is the same as

those prepared for the collision terms. In this simulation, $20 \times 10 (20 \times 20)$ cells on a (θ, ζ)-plane are employed. The strength of the source/sink term ν_S is varied case by case because the growth rate of $\langle \mathcal{N}_1 \rangle$ and $\langle P_1 \rangle$ depends on the drift-kinetic model, magnetic configuration, and parameters such as E_ψ. See Eqs.(4.12) and (4.23). In most cases, the moderate strength $\nu_S = 0.5 \sim 1.0 \times \nu_i$ is enough to suppress $\mathcal{N}_1$ and P_1 to $\mathcal{O}(10^{-2})$, where ν_i is the ion-ion collision frequency. As demonstrated in Fig. 5.1 for the ZOW and ZMD simulations in the LHD case, it is confirmed that the final steady-state solutions of the neoclassical fluxes are not affected by the strength of the source/sink term nor the timing from when the source/sink term is turned on. It is obvious that without the source/sink term the ZMD model does not conserve $\langle P_1 \rangle$. The $\langle \mathcal{N}_1 \rangle$ and $\langle P_1 \rangle$ both continue to change in the ZOW model, as expected from the particle and energy balance relations in Sec. 4.1. In the series of simulations without source/sink, the neoclassical fluxes Γ_i and $\langle V_\parallel B \rangle$ continue evolving and one cannot obtain a quasi-steady state solution. By adopting $\nu_S = 0.5$ or 1.0, the ZOW and ZMD models both converge to a quasi-steady state at which one can take a time average. It is observed that the pattern of the fluctuations on the flux surface, $\mathcal{N}_1 - \langle \mathcal{N}_1 \rangle$ and $P_1 - \langle P_1 \rangle$, are sustained before and after turning on the source/sink term. This scheme works well in the global, ZOW, and ZMD models. For the DKES-like model, the source/sink term is not necessary because it preserves the total particle number and energy ideally. However, the weak source/sink was given in the DKES-like model in this work to reduce the numerical error accumulation in $\mathcal{N}_1$ and P_1.

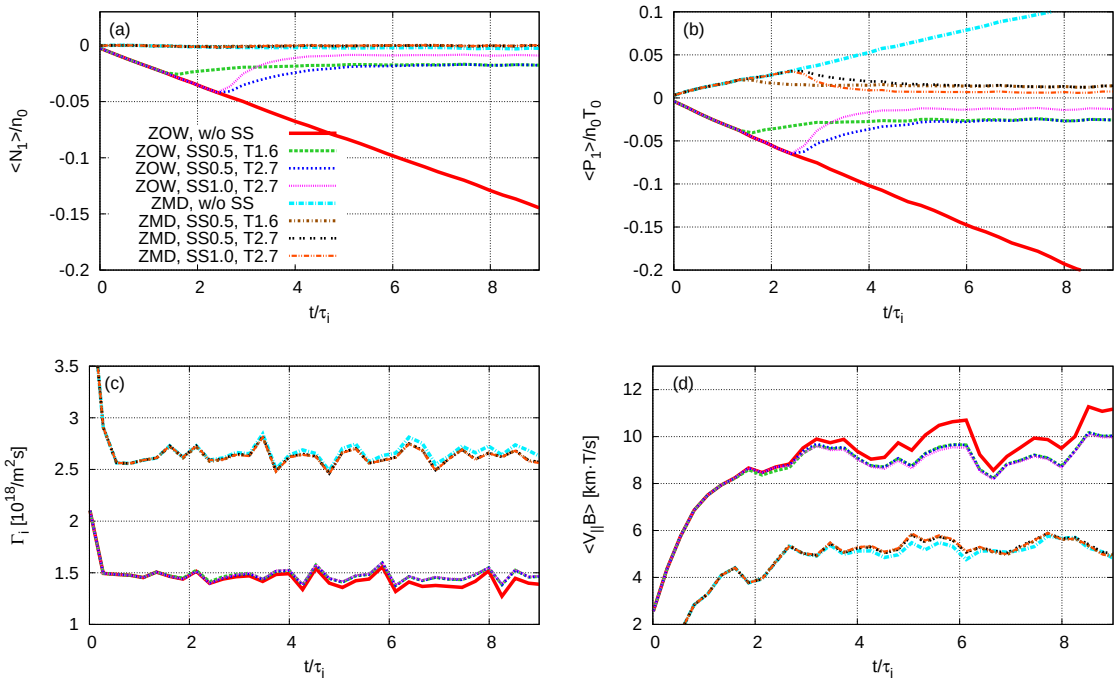

Figure 5.1: For the LHD ion, the time evolution of the LHD ion (a) the density perturbation $\langle \mathcal{N}_1 \rangle$, (b) the pressure perturbation $\langle P_1 \rangle$, (c) the neoclassical particle flux Γ_i and (d) the parallel flow $\langle V_\parallel B \rangle$ are shown in Sec. 6.1. Furthermore, Figs.(a) and (b) are normalized by background density and pressure, respectively. In Fig.(d), the parallel flows of the ZMD model are plotted offset by -4. The source/sink term is turned on at $t = 1.6\tau_i$ or $2.7\tau_i$. The numbers after "SS" in the legend indicate the strength of the source/sink term, ν_S.

Chapter 6

Benchmark of Local Drift-kinetic Model

A series of simulations are carried out to benchmark the local and the global drift-kinetic models. We compare the neoclassical radial particle flux Γ_a^ψ Eq.(4.14), radial energy flux Eq.(4.19), and the flux-surface average parallel mean flow multiplied by B,

$$\langle V_{a,\parallel} B \rangle \equiv \left\langle \int d^3v \; f_{a,1} v_{a,\parallel} B(\psi, \theta, \zeta) \right\rangle. \tag{6.1}$$

To see the radial fluxes and the heat fluxes in the units [1/m^{2}s] and [W/m^2], respectively, these are redefined as

$$\Gamma_a \equiv \frac{dr}{d\psi}\Gamma_a^\psi, \quad Q_a \equiv \frac{dr}{d\psi}Q_a^\psi,$$

where $r = a\sqrt{\psi/\psi_{edge}}$ and a is the effective minor radius of the plasma boundary, $\psi = \psi_{edge}$. a and ψ_{edge} are given from VMEC MHD equilibrium calculation code[16]. Note that in the local models even though f_1 does not contribute to radial fluxes in the particle and energy balance equations in Sec.4.1, Γ_a and Q_a are evaluated by the virtual radial displacement $\boldsymbol{v}_m \cdot \nabla r$-term in the local approximations.

The plasma parameters are given as TABLE 6.1. Two types of normalized ion collisionality ν_i^* are given in the table : $\nu_{i,PS}^* \equiv qR_{ax}\nu_{ii}/v_{thi} = 1$ represents the Plateau - PfirschSchlüter boundary and $\nu_{i,B}^* \equiv \nu_{i,PS}^*/(r/R_{ax})^{1.5} = 1$ is the Banana-Plateau boundary. For LHD, the inward-shift configuration is employed, in which the neoclassical radial transport is expected to be suppressed compared to that in a standard configuration. For W7-X, the magnetic geometry is adjustable by the coil current system. Here, the standard configuration [9] in the zero-β limit is employed. For HSX, the quasi-helically symmetric configuration is employed. The magnetic field configurations of both W7-X and HSX are chosen so as to reduce the radial guiding center excursion of trapped particles, while W7-X also aims at reducing the bootstrap current[9][1] The artificial density and temperature profiles are given in the LHD and W7-X investigations so that the plasmas are in $1/\nu$ regime around $|E_r| \sim 0$. The HSX kinetic profile is the diagnostic data from HSX experiment.[7] Compared to the other devices, the collisionality of the HSX plasma is high in terms of ν_{iB}^* because of very low T_i. In TABLE 6.1, the ambipolar E_r of the LHD and HSX simulations are shown, which have been evaluated by GSRAKE and DKES/PENTA, respectively.

In the following benchmarks, there are three types of DKES models, namely DKES, DKES-like, and DKES/PENTA. First, DKES is the original code with the pitch angle scattering collision operator. Thus, it does not guarantee the conservation of momentum. Second, DKES-like is the solver of Eq.(3.27) with the δf method and the linearized collision operator as ZOW and ZMD. The test-particle portions of collision operator include both the pitch-angle and energy scattering terms. The field-particle term maintains the conservation of particle numbers, parallel momentum, and energy in the simulation.[35] The third model, DKES/PENTA, is the numerical result from DKES and with momentum correction by Sugama-Nishimura method.[42][38] For LHD, local models are also benchmarked with GSRAKE code[3], which solves the mono-energy and the ripple-averaged drift-kinetic equations. GSRAKE is sim-

Table 6.1: Simulation parameters on each configuration.

	LHD	W7-X	HSX
r/a	0.7375	0.7500	0.3100
ι	0.740	0.886	1.051
R_{ax}/a	3.60/0.64	5.51/0.51	1.21/0.126
n_i $[10^{18}/m^3]$	3.10	0.406	3.83
T_i $[keV]$	0.891	0.350	0.061
T_e $[keV]$	0.891	0.350	0.544
B_{ax} $[T]$	2.99	2.77	1.00
$\nu^*_{i,B}$	0.0368	0.0910	17.3
$\nu^*_{i,PS}$	0.0017	0.0017	0.101

ilar to DKES but the magnetic field spectrum in GSRAKE is approximated.[3] It should be emphasized that the $\boldsymbol{E} \times \boldsymbol{B}$ drift term in GSRAKE is compressible, although this point has not been clearly mentioned in previous studies. [3][4] The original GSRAKE code is made so that it can include the tangential magnetic drift term. However, the term is omitted in the present benchmarks because the magnetic drift term is found to make the simulation result unstable[36].

6.1 Effect of E × B Compressibility

The radial electric field E_r is given as a parameter in this series of investigations. In Figs. 6.1 and 6.2, the ion radial particle and energy fluxes among the different approximations are presented on LHD, W7-X, and HSX, respectively. The figures of parallel flow simulation are shown in Fig. 6.3. The global simulations are carried out for LHD only because the global simulation requires much more computational resources than the local to reach a steady-state solution of $\langle V_{i,\parallel} B \rangle$. In Figs. 6.1 - 6.3, the good agreements appear among the local models in Γ_i, Q_i, and $\langle V_{i,\parallel} B \rangle$ if the radial electric field amplitude is moderate in terms of the poloidal Mach number, that is, $0 \ll |\mathcal{M}_p| \ll 1$.

Let us first focus on the difference which appears on the neoclassical fluxes at large-E_r values. When the amplitude of E_r rises, the discrepancies increase between

DKES-like and the other local models. As shown in Figs. 6.1(a), 6.2(a), and 6.3(a), the LHD radial and parallel fluxes of the ZOW, ZMD, and GSRAKE models agree with the global model well. Thus, the discrepancies comes from the incompressibility approximation of the $\boldsymbol{E} \times \boldsymbol{B}$ drift on DKES-like according to Eq.(3.26). According to Figs. 6.1-6.3, the $\boldsymbol{E} \times \boldsymbol{B}$ compressibility effect is expected to be significant when $|\mathcal{M}_p| > 0.4$.

The E_r-dependence of Γ_i, Q_i, and $\langle V_{i,\parallel} B \rangle$ found in the HSX case need more explanations. First, in Fig.6.1(d), all the cases, except for the original DKES, show a good agreement. The disagreement between the DKES model and the others is also found in the ion energy flux Fig. 6.2(c) and parallel flow Fig. 6.3(c). Recall that our DKES-like simulation uses the collision operator which ensures the conservation of parallel momentum in ion-ion collisions. The simulation result suggests that the momentum conservation property of the collision operator is essential for neoclassical transport calculation on quasi-symmetric devices like HSX. Secondly, as E_r increases, the neoclassical fluxes of all the models disagree with one another. As in the LHD and W7-X cases, the $\boldsymbol{E} \times \boldsymbol{B}$ compressibility is supposed to be the main cause of the disagreement. However, it should be pointed out that the ion parallel flow in HSX becomes supersonic at $\mathcal{M}_p > 1$ as shown in Fig.6.3. Here, the parallel Mach number is defined as

$$\mathcal{M}_\parallel \equiv \frac{\langle V_\parallel B \rangle}{v_{th} B_{ax}}. \tag{6.2}$$

In the work, the drift-kinetic models are constructed under the assumption $\mathcal{M}_\parallel \ll 1$ because we just takes the zeroth order distribution as the Maxwellian without the mean flow. See Eqs.(3.5) and (3.6). The parallel flow dependence on E_r in HSX is contrastive to that in W7-X, in which parallel mean flow remains very slow compared to thermal velocity, as in Fig. 6.3(b). Both HSX and W7-X configurations aim at reducing radial neoclassical flux. However, the magnetic configuration of W7-X is chosen to reduce the parallel neoclassical flow, too. This leads to the different dependence of parallel flow on E_r in these two devices. Note also that $T_e \gg T_i$ in

HSX [27] while $T_i = T_e$ in LHD and W7-X cases. In such a $T_e \gg T_i$ plasma, $\mathcal{M}_p$ of $\boldsymbol{E} \times \boldsymbol{B}$ flow by ambipolar-E_r can be $\mathcal{O}(1)$ because of the slow ion thermal velocity $v_{th,i}$. For example, under the ambipolar condition, $\mathcal{M}_p \simeq -0.015$ and $E_r \simeq -1.73$ kV/m on LHD by GSRAKE, while $\mathcal{M}_p \simeq 0.95$, and $E_r \simeq 3.47$ kV/m on HSX by DKES/PENTA. Such a large $\mathcal{M}_p$ with the quasi-symmetric configuration of HSX results in $\mathcal{M}_\parallel \sim \mathcal{O}(1)$. When $\mathcal{M}_\parallel > 1$, all the drift-kinetic models violate the assumption of the slow-flow-ordering. Therefore, although $\mathcal{M}_p \sim \mathcal{O}(1)$ $\boldsymbol{E} \times \boldsymbol{B}$ flow is allowed in ZOW and ZMD models, the validation of the drift-kinetic models at $\mathcal{M}_\parallel \sim \mathcal{O}(1)$ has to be reconsidered by taking account of the centrifugal force and potential variation along the magnetic field lines[40]. This problem is beyond the scope of the present study.

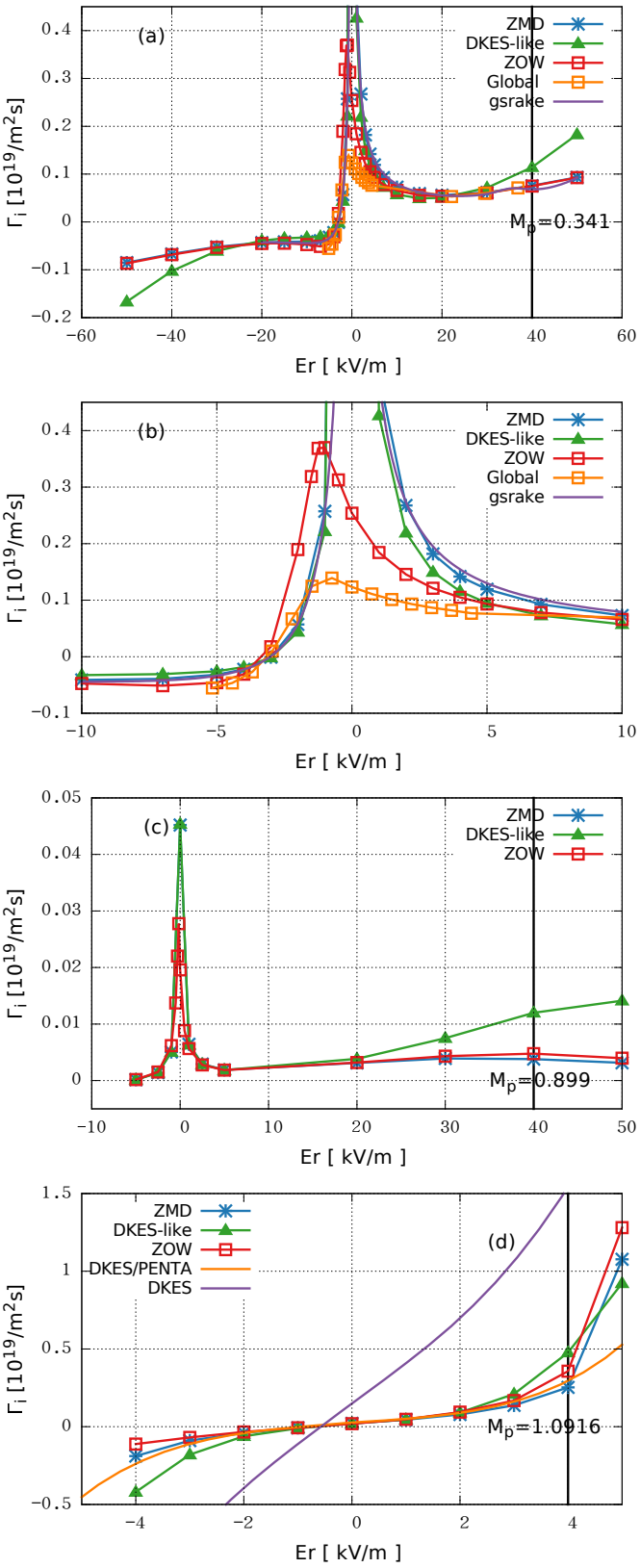

Figure 6.1: Ion particle fluxes Γ_i of (a) LHD, (c) W7-X, and (d) HSX , respectively. (b) is an enlarged view of (a) around $E_r \sim 0$. The multiple numerical results of DKES model with the different collision operators are shown in (d). The vertical line shows the value of poloidal Mach number $\mathcal{M}_p$ defined in Eq.(3.1).

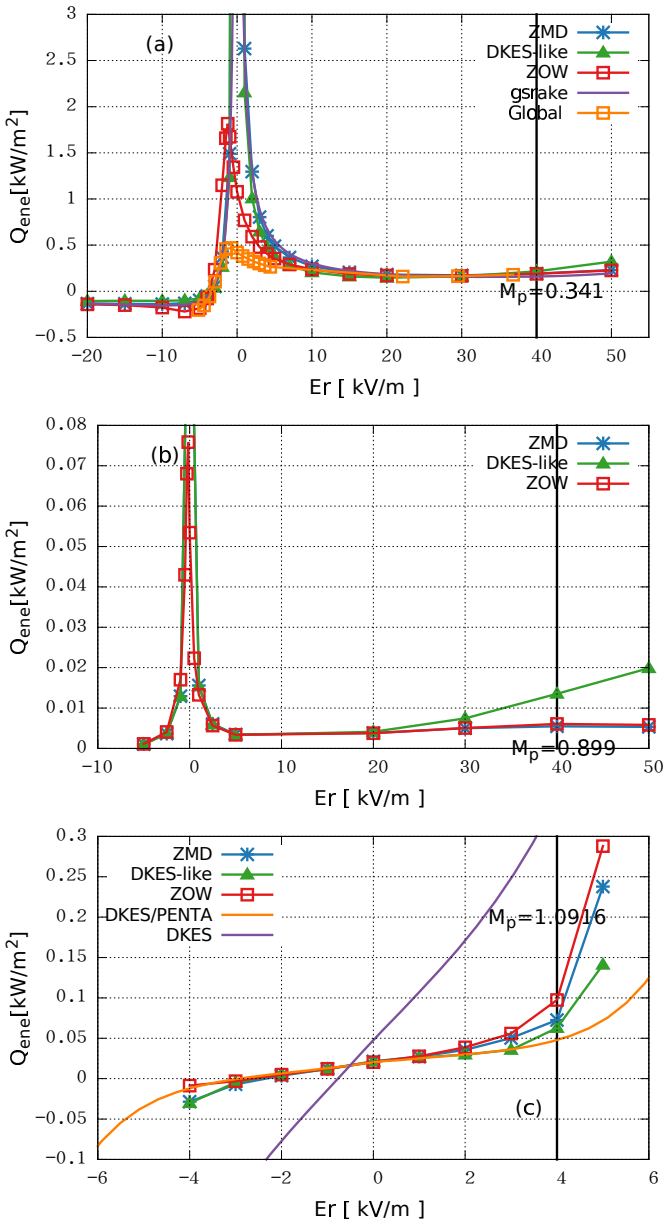

Figure 6.2: Ion energy flues Q_i of (a) LHD, (b) W7-X, and (c) HSX, respectively.

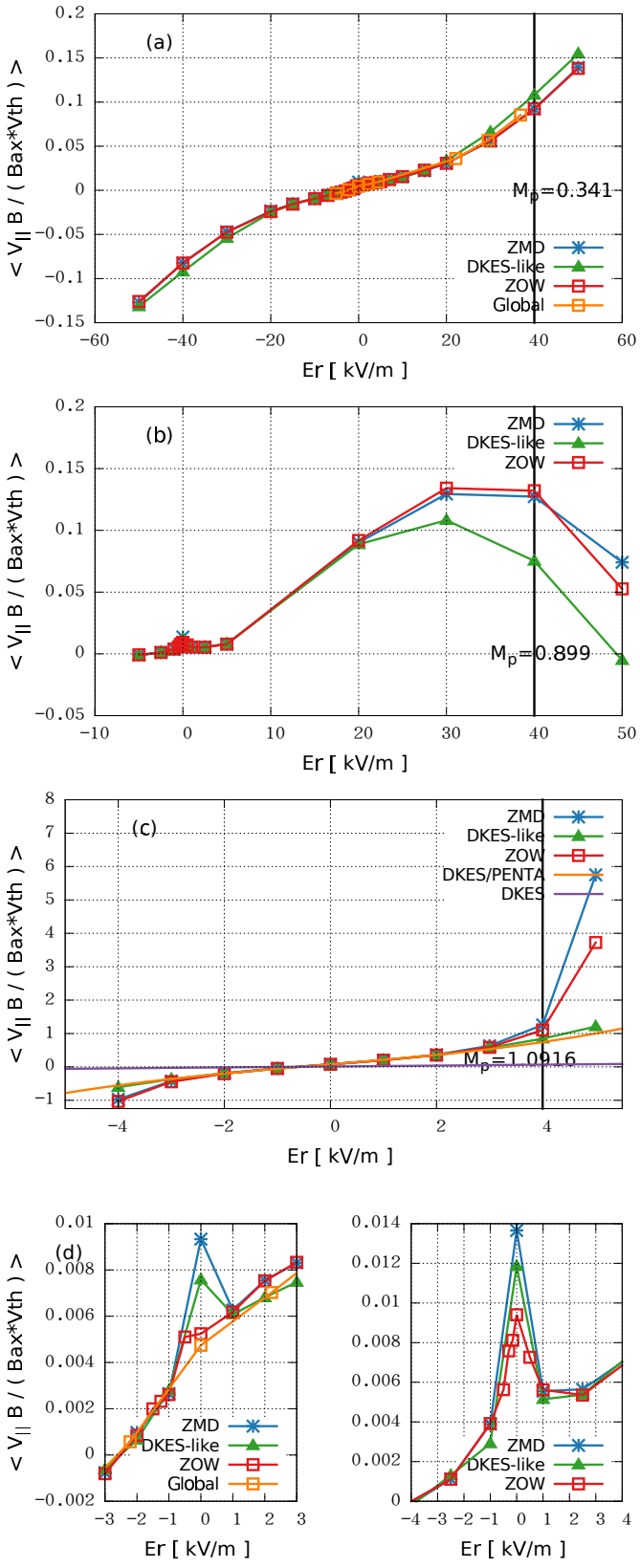

Figure 6.3: Ion parallel flow of (a) LHD, (b) W7-X, and (c) HSX, respectively. (d) presents the enlarged details around $E_r \sim 0$ for the LHD and W7-X cases. The vertical axis represents the parallel Mach number $M_{||}$ as defined in Eq. (6.2).

6.2 Effect of Magnetic Drift

In Figs. 6.1-6.2, there are the very large peaks of Γ_i and Q_i at $E_r = 0$ in the LHD and W7-X cases by the ZMD and the DKES-like models. On the contrary, the global and the ZOW models show the reduction of radial fluxes at $E_r \simeq 0$ and the peaks shift to negative-E_r side. This tendency has been found in the previous study[29], and this greatly modifies the neoclassical transport in $1/\nu$-regime, especially in the LHD case. For HSX, there is not such a peak at $E_r = 0$ in the result of ZMD and DKES-like models. What causes the reduction of Γ_i and Q_i in ZOW, and what makes the configuration dependence?

First of all, the problem is considered by analytical formulation. In a simple stellarator/heliotron magnetic configuration like LHD, the amplitude of the magnetic field is given approximately

$$|\boldsymbol{B}| \approx B_0[1 - \epsilon_h \cos(l\theta - m\zeta) - \epsilon \cos\theta], \tag{6.3}$$

where ϵ_h and ϵ are helical and toroidal magnetic field modulations, respectively. l is the helical field coil number and m is the number of toroidal periods. Once a particle is trapped by the helical ripples, its orbit drifts across the magnetic surface and contributes to the radial flux. The estimation of particle flux is roughly given as[32]

$$\Gamma \sim -\left\langle \int \frac{\nu_{\text{eff}}}{(\nu_{\text{eff}})^2 + (\omega_h + \omega_E)^2} V_\perp^2 \frac{\partial f_M}{\partial r} d^3v \right\rangle. \tag{6.4}$$

Here, ν_{eff} is the effective collision frequency of trapped particle and defined as $\nu_{\text{eff}} \equiv \nu/\epsilon_h$. ω_h and ω_E represent the poloidal precession frequency of the trapped particles by the magnetic drift and $\boldsymbol{E} \times \boldsymbol{B}$ drift, respectively. $V_\perp$ denotes the radial drift

velocity. For trapped particles, they are estimated as [2]

$$V_\perp \sim \frac{v_d}{\epsilon_t B_0}\frac{\partial B}{\partial \theta} \sim v_d \frac{\epsilon}{\epsilon_t}, \qquad \omega_h \sim \frac{v_d}{\epsilon_t B_0}\frac{\partial B}{\partial r}, \quad \omega_E \sim \frac{E_r}{r B_0}, \tag{6.5}$$

where $v_d \equiv \mathcal{K}/eB_0R_0$ and $\epsilon_t = r/R_0$. If $(\nu_{\rm eff})^2 \gg (\omega_h + \omega_E)^2$, then Eq.(6.4) indicates that the particle transport is inversely proportional to the collision frequency.

Approximating $\omega_h \to 0$ in Eq. (6.4) corresponds to ZMD and DKES models. Then, around $E_r = 0$, Γ_i shows $1/[\nu_{\rm eff}(1+x^2)]$-type dependence where $x = (\omega_E/\nu_{\rm eff})^2$. The ω_E is common for all the particles on a flux surface so that it makes a strong resonance at $\omega_E = 0$. Once the finite ω_h is considered, the peak of Γ_i appearing at the poloidal resonance condition $\omega_h + \omega_E = 0$ becomes blurred because of ω_h dependence on $\boldsymbol{v}, \theta$, and ζ. This explains the difference between the ZOW and the ZMD models in the LHD case.

The analytic model of the $1/\nu$-type diffusion infers that the strong resonance of trapped-particles at $E_r = 0$ in ZMD and DKES-like models is damped by Coulomb collisions. To demonstrate this, the 10 times larger density simulations are carried out for the LHD case as shown in Fig. 6.4. It is found that the strong peak in Γ_i and $\langle V_{i,\parallel} B\rangle$ at $E_r = 0$ in ZMD and DKES-like calculations are diminished, and the difference from the ZOW result is small. It is concluded that the tangential magnetic drift is more important for neoclassical transport calculation in the lower collisionality case and when $|\omega_E| < |\omega_h|$.

Secondly, in the W7-X case, the magnetic field spectrum is much more complicated than the simple model Eq. (6.3). It is generally expressed in a Fourier series as follows:

$$B(\psi, \theta, \zeta) = B_0 \sum_{m,n} b_{m,n}(\psi) \cos(m\theta - 5n\zeta). \tag{6.6}$$

Compared with LHD, W7-X has good modular coil feasibility to adjust $b_{m,n}$ [13]

where the helical $b_{1,1}$ and toroidal $b_{1,0}$ magnetic field modulations are equal to ϵ_h and ϵ respectively in Eq.(6.3). One of the neoclassical optimizations is performed by the reduction of average toroidal curvature $b_{1,0}/\epsilon_t \sim 0.5$[9] compared to that in LHD, $\epsilon/\epsilon_t \simeq 1$. According to Eq. (6.8), this partially explains the smallness of $1/\nu$-regime transport in W7-X. However, the magnetic spectrum of W7-X contains other Fourier components which are comparable to $b_{1,0}$ and $b_{1,1}$. Thus, the simple analytic model, such as Eqs. (6.3) and (6.8), is insufficient to explain its optimized neoclassical transport level.

The quasi-isodynamic concept of the neoclassical optimized stellarator configuration is as follows: the trapped particles in the toroidal magnetic mirrors $b_{0,1}$ precess in the poloidal direction while their radial displacements are small and return to the same flux surface after they circulate poloidally. The trapped particle trajectory in quasi-isodynamic W7-X configuration has been analyzed using the second adiabatic invariant[10]

$$\begin{aligned} \mathfrak{J}_{\parallel} &= \int dl\ v_{\parallel} = \int d\zeta\ \frac{\sqrt{(2\mathcal{K} - 2\mu B)/m}}{\boldsymbol{b}\cdot\nabla\zeta} \\ &\propto \int d\zeta \frac{\sqrt{B_{ref} - B}}{B}, \end{aligned} \tag{6.7}$$

where B_{ref} represents the magnetic field strength at the reflecting point of a trapped particle. Deeply-trapped particles move along the $\mathfrak{J}_{\parallel}$ =const. surfaces. Then, if the constant- $\mathfrak{J}_{\parallel}$-contours on a poloidal cross-section are near a flux-surface function and if the contours are closed, the radial transport of the trapped particles are suppressed. However, the standard configuration, which we investigate, is not fully optimized as is the quasi-isodynamic configuration. The $\mathfrak{J}_{\parallel}$ = constant surfaces in the standard configuration have small deviation from the flux surfaces[10]. Therefore, in the limit $\omega_E + \omega_h = 0$, the deeply-trapped particles drift radially along the $\mathfrak{J}_{\parallel}$ contours. Consequently, the radial flux in W7-X solved with ZMD and DKES-like models shows the strong peak at $E_r = 0$. As expected from the form of Eq. (6.4),

either by increasing the collision frequency or by taking account of finite ω_h as in the ZOW model results in decreasing the radial transport at $E_r = 0$. In Fig. 6.5 we have examined the radial and parallel flux in 10 times larger density W7-X plasma than those in Figs. 6.1(c) and 6.3(b). As found in the LHD case, the difference among the ZOW, ZMD, and DKES-like models at $E_r = 0$ diminished in the higher collisionality W7-X case. It is worthwhile to note that it has already been pointed out that the improvement of collisionless particle confinement in W7-X configuration is realized not only in quasi-isodynamic geometry but also by enhancing the poloidal magnetic drift in finite-β W7-X plasma because $\partial b_{0,0}/\partial r \propto \omega_h$ increases as the plasma-β.[49]

In the simulations, steady-state solution of parallel flow is obtained when the parallel momentum balance relation Eq.(4.29) is satisfied. As explored in Sec. 4.2, in the parallel momentum balance relation, the differences among the drift-kinetic models includes four parts: (1) the explicit difference of the tangential drift velocities in $\langle \boldsymbol{B} \cdot \nabla \cdot \boldsymbol{\Pi}_2 \rangle$, (2) the implicit difference of $\langle \boldsymbol{B} \cdot \nabla \cdot \boldsymbol{P}_{\mathrm{CGL}} \rangle$ through f_1, (3) the extra term Eq.(4.33) which breaks the symmetry of Π_2 in ZOW, and (4) the term (4.34) related to $\mathcal{G} = \nabla_z \cdot \dot{\boldsymbol{Z}}^{\mathrm{ZOW}} \neq 0$. $\langle \boldsymbol{B} \cdot \nabla \cdot \boldsymbol{\Pi}_2 \rangle$ in DKES-like and ZMD models do not contain $\hat{\boldsymbol{v}}_m$. These models disagree with each other gradually as E_r increases. This indicates that the discrepancy between Eqs.(4.37) and (4.40) on the compressibility of $\boldsymbol{E} \times \boldsymbol{B}$ affects the evaluation of parallel flow. Meanwhile, the ZMD and ZOW tendencies are similar in the wide range of E_r in Figs.6.3. As a result, the two extra parallel-viscosity terms appearing in the ZOW model do not influence the parallel flow. In Fig.6.3(d), there are small peaks at $E_r = 0$. When $E_r = 0$, the poloidal resonance leads to the extra large radial fluxes in Fig.6.1(a) and 6.1(c). Equations (4.14) and (6.4) suggest that f_1 becomes very large at the resonance. However, the resonance occurs on trapped particles, which cannot contribute to parallel flow. The influence of resonance is passed to the passing particles via collisions to change the momentum balance through $\langle \boldsymbol{B} \cdot \nabla \cdot \boldsymbol{P}_{\mathrm{CGL}} \rangle$. The parallel flows peak at $E_r = 0$ is

much less than the radial flux peaks because it is driven by this indirect mechanism.

Model	Γ $[1/m^2 s]$
ZOW	1.72×10^{15}
ZMD	2.15×10^{16}
DKES-like	2.10×10^{16}

Table 6.2: The particle flux of HSX at $E_r = 0$ with 0.01 times density than that in Table 6.1.

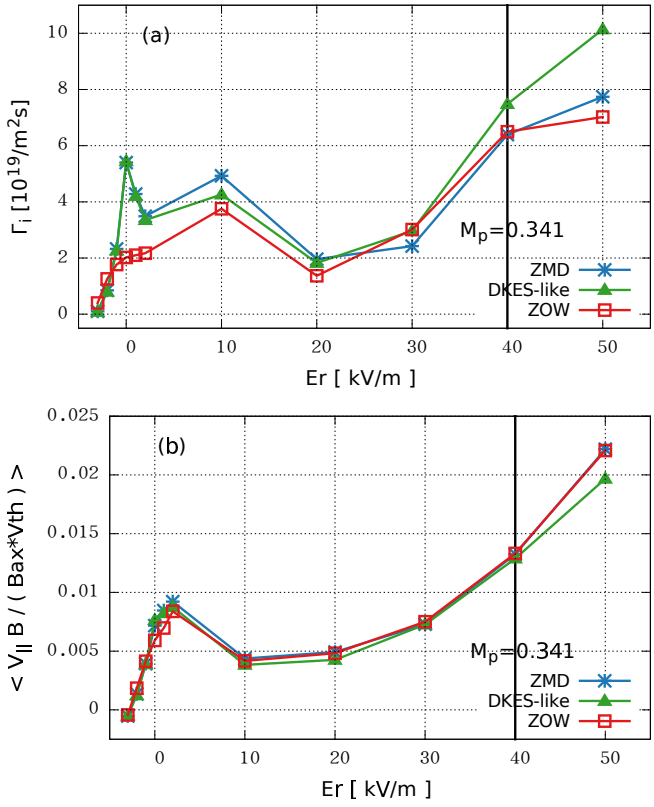

Figure 6.4: (a) The radial particle flux and (b) ion parallel flow of high collision frequency test of LHD. The normalized collision frequency is 10 times higher than ν^* on LHD in Table 6.1.

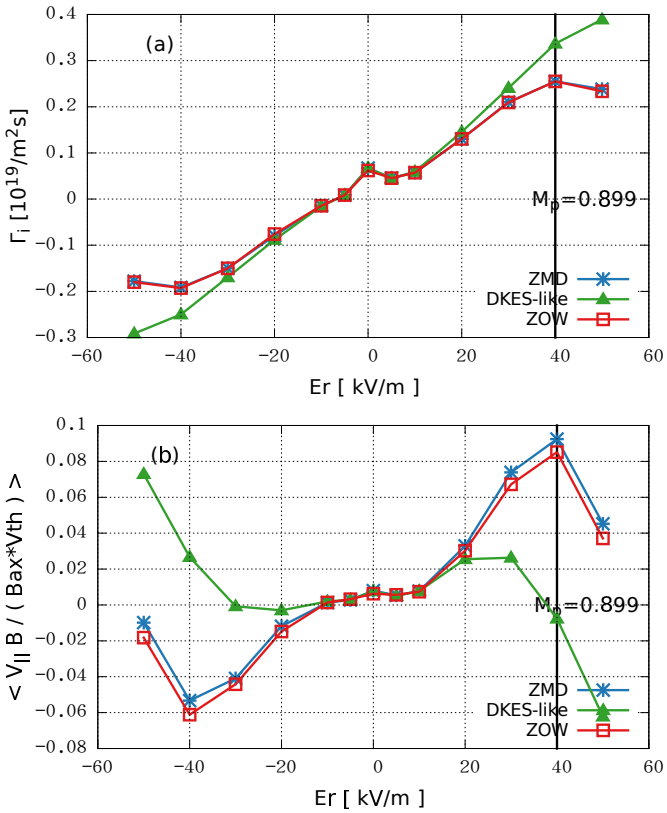

Figure 6.5: (a) The radial particle flux and (b) ion parallel flow of higher collision frequency test on W7-X. The normalized collision frequency is 10 times higher than ν^* of W7-X in Table 6.1.

6.3 Effect of Magnetic Collision Frequency

The diffusion coefficient in $1/\nu$-regime is approximated as[2]

$$D_h \approx {\epsilon_h}^{1/2}(\Delta_h)^2\nu_{\rm eff} \sim {\epsilon_h}^{3/2}\left(\frac{T}{eB_0R_0}\frac{\epsilon}{\epsilon_t}\right)^2\frac{1}{\nu}, \tag{6.8}$$

where $\Delta h = V_\perp/\nu_{\rm eff}$ is the estimation of the radial step size of helically trapped particles.

Quasisymmetric HSX can be regarded as the $\epsilon \to 0$ limit of Eq. (6.3).[1] The bounce-average radial drift $\langle V_\perp \rangle$ vanishes in the quasisymmetric limit $\epsilon/\epsilon_t = 0$ so that HSX shows the low radial particle transport at $E_r \simeq 0$ as in Fig.6.1(d) in all local models. The radial flux is of comparable level to that in equivalent tokamaks. However, it should be noted that the collisionality of the present HSX case is in plateau-regime. Then, the discussion on the radial transport level in HSX using Eq. (6.4) is inadequate. Following the previous benchmark study on local neoclassical simulations[4], there are tiny magnetic ripples in the actual HSX magnetic field made by the discrete modular coils, which causes $1/\nu$-type diffusion coefficient at very low-collisionality, $\nu^*_{PS} < 10^{-3}$, in the DKES calculation. Therefore, we benchmarked the local drift-kinetic models in HSX with 100 times smaller plasma density ($\nu^*_{PS} \simeq 1.0 \times 10^{-3}$) at $E_r = 0$. The results are shown in Table 6.2. The radial flux in very low-collisionality regime in HSX shows discrepancy among ZOW, ZMD, and DKES-like models, as found in the LHD and W7-X cases. Though the $1/\nu$-regime appears from lower ν^* value in HSX than LHD, the effect of the tangential magnetic drift on neoclassical transport appears in the same way.

Concerning the parallel flows, Fig.6.3 shows that all models agree with each other well at $0 \ll \mathcal{M}_p \ll 1$. Compared to the radial flux, the magnetic drift does not influence the parallel flow strongly at $E_r \sim 0$, even in the low-collisionality LHD and W7-X cases. On the other hand, the discrepancies of parallel flows at large-$|\mathcal{M}_p|$

appear as clearly as that of the radial flux.

In summary, as long as the collisionality is low enough to present the $1/\nu$-type diffusion at the condition $|\omega_E| < |\omega_h|$, the ZMD and DKES-like models, which ignore the tangential magnetic drift term, tend to overestimate the neoclassical flux at $E_r \to 0$ in all three helical configurations in this work. The ZOW model reproduces the similar trend as the global simulation in which the finite ω_h term results in reducing the $1/\nu$-type diffusion. The strong poloidal resonance $\omega_E = 0$ without ω_h term in these local models results in the strong modification in the perturbed distribution function f_1, and it indirectly affects the evaluation of parallel flow $\langle V_\parallel B \rangle$, too.

6.4 Electron Neoclassical Transport

In order to benchmark the bootstrap current calculation at ambipolar condition among the local models, the electron neoclassical transport simulations were carried out for the LHD case. The results are shown in Figs. 6.6. In the entire range of E_r, it is found that the differences of Γ_e, Q_e, and $\langle V_{e,\parallel} B \rangle$ between the two groups, i.e., (global, ZOW) and (ZMD, DKES-like), are smaller than those in the ion calculations. As the electron thermal velocity is much faster than the ions, the poloidal Mach number for electrons is always regarded as $\mathcal{M}_{p,e} \sim \mathcal{O}(\delta)$. Therefore, the $\boldsymbol{E} \times \boldsymbol{B}$-compressibility is not important for the electron calculation. Moreover, compared with Fig.6.1(a), Fig.6.6(a) does not present any obviously unphysical peak of the radial particle transport at $E_r \simeq 0$. There is the same feature in the energy flux. (See Fig.6.1(a) and 6.6(b).) Even though the normalized collision frequencies $\nu_{*,B}$ (or $\nu_{*,PS}$) are the same in the ion and electron simulations, it seems that the collision effect is stronger in electrons than ions to blur the tangential magnetic drift effect around $E_r = 0$. Note that the precession drift frequency by the magnetic drift is also the same order between ions and electrons. See Eq.(6.5). The difference of

the tendency at $E_r \simeq 0$ between ions and electrons is considered as follows. The collision frequency of particle species a is proportional to [5]

$$\nu_a \propto \frac{(e_a)^4 n_a}{m_a^2 v_a^3}. \tag{6.9}$$

For the LHD simulations, the temperature is set as $T_e = T_i$. Thus, the ratio of collision frequency between the electron and ion is

$$\frac{\nu_e}{\nu_i} \propto \left(\frac{m_i}{m_e}\right)^{\frac{1}{2}} \gg 1 \tag{6.10}$$

because of $Z_i = Z_e = 1$ in this work. On the other hand, the normalized collision frequency $\nu_* (= \nu_{*,PS})$ is defined as $\nu_{*,a} \equiv qR_{ax}\nu_a / v_{th,a}$. Therefore, the ratio between the normalized electron and ion collision frequency is

$$\frac{\nu_{*,i}}{\nu_{*,e}} \propto \left(\frac{m_e}{m_i}\right)^{\frac{1}{2}} \frac{v_{th,e}}{v_{th,i}}. \tag{6.11}$$

Eqs. (6.10) and (6.11) suggest that $\nu_e \gg \nu_i$ though $\nu_{*,e} = \nu_{*,i}$. In Eq.(6.4), it is not the normalized collision frequency but the real collision frequency that appears in the form $\nu_{a,\mathrm{eff}} = \nu_a / \epsilon_h$. ω_h and ω_E are the same order between ions and electrons so that the ratio between these terms in the denominator of Eq. (6.4),

$$(\omega_h + \omega_E)^2 / \nu_{\mathrm{eff}}^2$$

is smaller for electrons than that for ions. Therefore, the finite-ω_h effect in the ZOW model is not as important for electrons than as for ions.

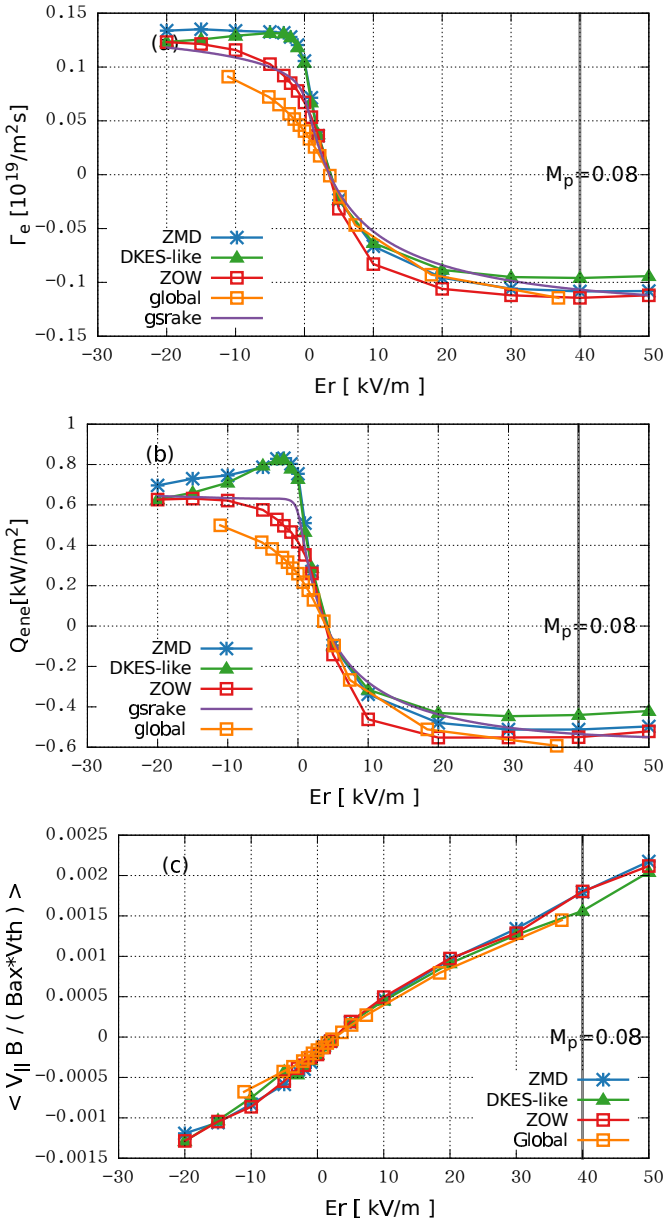

Figure 6.6: (a) The electron radial particle flux, (b) the energy flux, and (c) the parallel flow in the LHD case shown in Table 6.1.

6.5 Bootstrap Current

The LHD bootstrap current is investigated among the drift-kinetic models. In Fig.6.7, the bootstrap current is estimated by ion and electron parallel flows as

$$J_{BC} = e(Z_i \langle v_{i,\parallel} B \rangle n_i - \langle v_{e,\parallel} B \rangle n_e)/B_{ax}. \tag{6.12}$$

It is found that the discrepancy of bootstrap current among the models increases when E_r rises. This indicates that the gap mainly comes from the effect of $\boldsymbol{E} \times \boldsymbol{B}$ compressibility on the ion parallel flow as it is found in Fig.6.3(a). The local drift-kinetic models are divided into two groups, DKES-like and the others. In the following discussion, the two extra terms in the ZOW model, Eqs.(4.33) and (4.34), are ignored because it is found that the difference caused from these two terms is negligible among the ZMD and the ZOW models. Neglecting the $neE_\parallel B$ term in Eq.(4.29), the parallel momentum balance in a steady-state is written as

$$\langle \boldsymbol{B} \cdot \nabla \cdot (\boldsymbol{P}_{\mathrm{CGL}} + \boldsymbol{\Pi}_2) \rangle_a = \langle B F_{a,\parallel} \rangle. \tag{6.13}$$

The friction $F_\parallel$ is estimated as follows: For ion, the friction between ions and electrons is ignored because of large mass ratio. And, the parallel momentum balance depends only on $\boldsymbol{P}_{\mathrm{CGL}}$ and $\boldsymbol{\Pi}_2$:

$$\langle \boldsymbol{B} \cdot \nabla \cdot (\boldsymbol{P}_{\mathrm{CGL}} + \boldsymbol{\Pi}_2) \rangle_i = 0. \tag{6.14}$$

For electrons, not only the viscosity but also the electron-ion parallel friction $F_{ei,\parallel}$ are considered. And the parallel friction is approximated by

$$F_{ei,\parallel} \simeq \nu_{ei,\parallel} m_e n_e (V_{i,\parallel} - V_{e,\parallel}), \tag{6.15}$$

where $\nu_{ei,\parallel}$ is the parallel momentum-transfer frequency. The friction acting on ions is ignored, $F_{ie,\parallel} = -F_{ei,\parallel}$ so that the total parallel momentum is not conserved in the simulation. Moreover, as explained in section 5.1, the electron-ion collision in the simulation is simplified by the pitch-angle scattering operator Eq.(3.28) where ion mean flow is ignored. Therefore, in the present simulation models, the electron parallel momentum balance is approximated as

$$\langle \boldsymbol{B} \cdot \nabla \cdot (\boldsymbol{P}_{\mathrm{CGL}} + \boldsymbol{\Pi}_2) \rangle_e = -\langle \nu_{\parallel,ei} m_e n_e V_{e,\parallel} B \rangle. \tag{6.16}$$

In Eqs.(6.15) and (6.16), the viscosity $\boldsymbol{\Pi}_2$ is directly influenced by the treatment of the guiding center motion tangential to the flux surface. See Eqs.(4.32), (4.37), and (4.40). J_{BS} in the DKES-like model deviates from that in the ZOW and the ZMD model. This shows that the incompressible-$\boldsymbol{E} \times \boldsymbol{B}$ assumption in $\boldsymbol{\Pi}_2$ mainly causes the difference in parallel momentum balance. Meanwhile, the contribution of the tangential magnetic drift $\hat{\boldsymbol{v}}_m$ is minor in the parallel momentum balance equation because the difference is negligible between the ZMD and the ZOW models in Fig.6.7. It should be noted that the approximation in the $F_{\parallel,ei}$ in our simulation is valid when $|V_{\parallel,e}| \gg |V_{\parallel,i}|$. Actually, the electron and ion parallel flows can become comparable. For a more quantitative evaluation of bootstrap current, the effect should be considered when ion mean flow dominates the bootstrap current, for example, when J_{BS} is at $E_r > 30kV/m$ in Fig.6.7. This work is to investigate neoclassical transport among the local drift-kinetic models so that the rigorous treatment of the parallel friction is left in Part II.

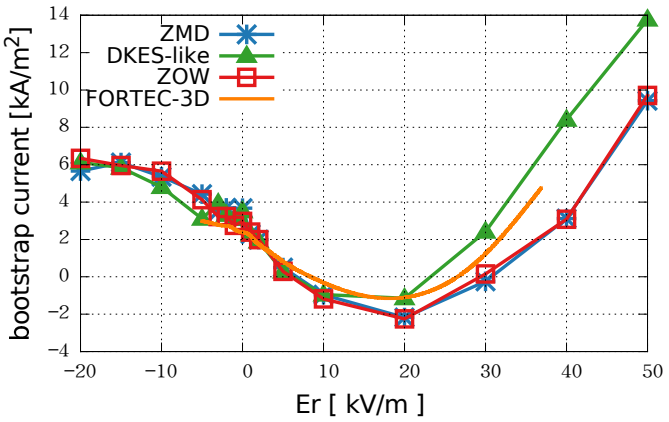

Figure 6.7: The bootstrap current in the LHD case by combining Fig.6.3(a) with Fig.6.6(c).

	E_r $[kV/m]$	Γ $[10^{19}/m^2 s]$	J_{BS} $[kA/m^2]$	$Q_i[kW/m^2]$	$Q_e[kW/m^2]$
Global	-2.34	0.057	2.88	0.272	0.343
ZOW	-2.59	0.089	3.23	0.614	0.515
ZMD	-1.55	0.123	3.22	0.880	0.819
DKES	-1.66	0.125	3.55	0.595	0.807
GSRAKE	-1.73	0.089	N/A	0.519	0.628

Table 6.3: The ambipolar conditions of LHD in each model.

Chapter 7

Conclusions of Part I

A series of neoclassical transport benchmarks has been presented among the drift-kinetic models in helical plasmas. The two-weight δf scheme is employed to carry out the calculations of particle flux, energy flux, and parallel flow. The δf formulation in this work allows the violation of Liouville's theorem in a local drift-kinetic approximation as in the ZOW model. The treatments of the convective derivative term $(\boldsymbol{v}_E + \boldsymbol{v}_m) \cdot \nabla f_{a,1}$ are different among the local drift-kinetic models. For example, the ZOW model maintains the tangential magnetic drift $\hat{\boldsymbol{v}}_m$ which results in the compressible phase-space flow, $\mathcal{G} \neq 0$. On the contrary, in the ZMD and the DKES models, the magnetic drift is completely neglected, but instead the phase-space volume is conserved. The finite $\mathcal{G}$ term in ZOW brings $\mathcal{O}(\delta^2)$-correction in the particle, parallel momentum, and energy balance equations. The simulation results have demonstrated that the ZOW and the ZMD models agree with each other well in the wide range of E_r value. This fact is a clear indication that the $\mathcal{O}(\delta^2)$-correction term is negligibly small in neoclassical transport calculation. The only exception is around $\boldsymbol{v}_E \simeq 0$, where the ZMD and DKES-like models show the very large peaks of neoclassical flux. Owing to the tangential magnetic drift $\hat{\boldsymbol{v}}_m$, the ZOW simulation evaluates the radial fluxes and parallel flows around $E_r \simeq 0$ which are much more smoothly dependent on E_r and similar to those obtained from the

global calculations.

Effects of the tangential magnetic drift $\hat{v}_m$ becomes stronger under the following conditions. First, according to the simulations, the tangential magnetic drift $\hat{v}_m$ is more obvious in LHD than W7-X and HSX. In W7-X and HSX, the magnetic configuration is chosen so as to reduce the radial drift of trapped particles and remains the neoclassical transport in $1/\nu$-regime. This reduces the peak value of Γ_i at the poloidal resonance, $\omega_E + \omega_h = 0$ in Eq. (6.4), and results in the small gap between the ZMD and the ZOW models in these machines compared to LHD. Second, the effect is obvious in the low collisional plasma. At $E_r \simeq 0$, the tangential magnetic drift is required to avoid the poloidal resonance. Otherwise, the artificially strong $1/\nu$-type neoclassical transport will occur. Third, the ZOW, ZMD, and DKES-like models agree with one another in a series of electron simulations. The discrepancies occur more clearly on the ions. This suggests that the conventional local drift-kinetic models are sufficient for electron simulation.

The difference in the treatment of the $\boldsymbol{E} \times \boldsymbol{B}$ drift term has also been found to cause a large error in neoclassical transport calculation. The assumption of incompressible $E \times B$ drift in the DKES-like model results in the miscalculation of the neoclassical transport for the larger poloidal Mach number of $\mathcal{M}_p > 0.4$. Due to the mass dependency of $\mathcal{M}_p \propto v_E/v_{th,a} \sim \sqrt{m_a}$, the heavier ion $\mathcal{M}_p$ such as He and W increases. Therefore, the parameter window in which the incompressible-$\boldsymbol{E} \times \boldsymbol{B}$ approximation is valid will be narrower for heavier species.

Regarding the practical application, the neoclassical flux and bootstrap current are evaluated at the ambipolar condition. The ion-root usually exists when $T_i \simeq T_e$; the electron-root appears when $T_i \ll T_e$[48]. The peak of Γ_i at $E_r = 0$ is an artifact of the ZMD and the DKES-like models. It suggests that the T_e/T_i is the threshold of transition between the ion-root and the electron-root. Therefore, the magnitude of T_e/T_i will be less/lower in the global and the ZOW models than in the ZMD and the DKES models. The neoclassical transport varies drastically if

the ambipolar-E_r switches from an ion-root to an electron-root. Therefore, the tangential magnetic drift term plays a decisive role in the local models for the investigation of the ambipolar-root transition. Figure 6.7 indicates that the $\hat{v}_m$ term slightly affects the bootstrap current evaluation. Furthermore, the sign of the bootstrap current may change when the ambipolar-E_r transits from a negative to a positive root. This will be also related to the study on the bootstrap current effect on MHD equilibrium.

The dependence of neoclassical transport on radial electric field is studied. The obvious difference appears at $E_r \simeq 0$ or $\mathcal{M}_p \sim 1$ among the drift-kinetic models. For the practical application on helical devices, it is important for evaluating the neoclassical fluxes at the ambipolar condition. The LHD ambipolar condition is investigated by searching the E_r value where $Z_i\Gamma_i = \Gamma_e$. As shown in Table 6.3, the ambipolar-E_r values from different models are located between -2.6 and -1.5 $[kV/m]$. The amplitude of electric field, radial flux, and bootstrap current at the ambipolar condition are obtained by the interpolation as shown in Table 6.3. The ambipolar-E_r magnitude of the ZMD model is close to the DKES-like and GSRAKE magnitudes, while the ZOW model predicts closer E_r to the global simulation. Around the ambipolar condition, the bootstrap current amplitudes are just minor differences among the drift-kinetic models. Owing to $T_i \sim T_e$, the ambipolar condition is on the ion-root. In this case, the finite E_r on the ion-root is sufficient to suppress the poloidal resonance but insufficient to make an obvious gap by the $\boldsymbol{E} \times \boldsymbol{B}$ compressibility. The present case does not show any obvious advantage of the ZOW model compared to the other local models. If the tangential magnetic drift $\hat{v}_m$ increases or if the plasma collisionality is lower, the ZOW model has a possibility that it becomes more reliable than the other models in predicting the ambipolar-E_r, bootstrap current, and radial fluxes. The result of the ZOW model is close to the global simulation values so that the code requires less computation resources than the global. For example, in the LHD case, the ZOW model takes about 20% computational resources compared to

a global calculation with the same number of radial flux surfaces. In local simulation, one can choose a proper time step size according to the local parameters. On the other hand, in a global code, the time step size is a common parameter for all the markers. The step size must be small enough to resolve the fast guiding-center motion in the core, but it is much too fine for the markers in the low-temperature peripheral region. Another advantage of local simulation is fewer time steps to finish a calculation than a global one. For a local model, the calculation can be stopped after the time evolution converges on a single flux surface. For a global model, the calculation has to be continued untill the whole the plasma reaches a steady state.

On the basis of the study in Part I, the particle flux, energy flux, and bootstrap current of FFHR-d1 is studied in Part II. The FFHR-d1 magnetic configuration is similar to LHD so that the present study on an LHD configuration provides useful insight on the magnetic drift effect on the neoclassical transport in FFHR-d1. The effect of the bootstrap current on the MHD equilibrium will play a more important role in FFHR-d1 than that in present LHD operations because the central β will be about 5%[11].

It is found that the $\hat{v}_m$ term does not only decrease the height of the peak of Γ_i but also changes the value of E_r at which $\Gamma_i(r, E_r)$ peaks. The shift in E_r in LHD can be estimated by the bounce-averaged poloidal precession drift[3] of thermal ions as in Eq.(6.5). The bounce-averaged magnetic drift for deeply-trapped particles is approximated as

$$\begin{aligned} \omega_h &\sim \frac{v_d}{\epsilon_t B_0} \frac{\partial B_{2,10}(\rho)}{\partial r} \langle \cos(m\theta - n\zeta) \rangle_b \\ &\sim -\frac{4v_d}{a} \end{aligned} \tag{7.1}$$

where $\rho \equiv r/a$ and $\langle \cdots \rangle_b$ denotes the bounce-average over a particle trajectory trapped in a helical magnetic ripple. The radial dependence of the helical component is approximated as $B_{2,10}(\rho) \simeq 2(a/R_0)B_0\rho^2$ according to the tendency found in the

MHD equilibrium for LHD plasma. In Eq.(7.1), $(\theta, \zeta) = (0, \pi/10)$ is chosen because this is the bottom position of both toroidal and helical ripples. Substituting the parameters B_0, a, ϵ_t, and v_d for the LHD case, the shift of the Γ_i-peak is estimated as

$$E_r \simeq -\frac{4T_i\rho}{e_i R_0} \tag{7.2}$$

at which poloidal resonance $\omega_E + \omega_h = 0$ occurs. Eq.(7.2) agrees with the tendency of the peak shift in Γ_i from the ZOW and the global models, which are Figs.8-10 in Matsuoka et al.[29] Since high-temperature discharge $T_i > 10$ keV is planned in FFHR-d1, it is anticipated that the peak of Γ_i in the ZOW model will appear more negative-E_r which can be close to the ion-root E_r value. In such a case, the difference between the ZOW and ZMD models becomes significant in evaluating the neoclassical transport level in the ambipolar condition.

Part II

Applications of the ZOW Model to Bootstrap Current Calculations

Chapter 8

Introduction

The study of the bootstrap current is necessary to reproduce accurately the MHD equilibrium for high-beta plasmas. For the axisymmetric magnetic geometry, reliable analytic formulas of bootstrap current is available[37]. For the non-axisymmetric system, one needs to rely on numerical methods to evaluate the bootstrap current, which is complicatedly dependent on the magnetic geometry, the collision frequency, and the radial electric field. The past studies[31] presented the benchmark between the Monte-Carlo global model VENUS+δf and the local semi analytical solution SPBSC[47] in LHD. The bootstrap current between the VENUS+δf and the SPBSC codes shows a systematic difference. Although the difference may be caused in part by the finite-orbit-width effect, a missing discussion in that work is about the treatment of collision term. The VENUS+δf code did not treat the friction force between electrons and ions, while SPBSC solved the balance between parallel viscosity and friction force as shown in later in Eq. (6.13) by analytic formula. In order to carry out a more direct investigation on the impact of the parallel friction on the bootstrap current calculations, this work performs the benchmark among the ZOW model[29], DKES[46], and PENTA[38], which are all based on local neoclassical models.

In Part I, the benchmark of parallel flow is presented by the global, ZOW, ZMD and DKES models. It found that the ZOW model agrees with the global model. However, the collisions among the ions and electrons is expected to play an important role, while the ZOW collision operator in Part I still does not certainty satisfy Eq.(5.58). As discussed in Eqs.(6.15) and (6.16), for electron, the parallel momentum balance is related to the electron-ion friction $F_{ei,\|}$. For the investigation of the parallel friction effect on the bootstrap current calculation, in Part II the benchmark are performed among the ZOW[29], DKES[46], and PENTA[38] codes which are all local neoclassical models.

The rest of Part II is organized as follows. In chapter 9, the improved collision operator in the ZOW Model are introduced. In chapter 10, it presents the application for the FFHR-d1 DEMO reactor which includes the benchmark on the ion and electron parallel flow, ambipolar condition and the collision frequency dependence. Then, the conclusion of Part II is presented in chapter 11. In Appendix B, with tokamak geometry, the benchmark are presented to investigate the intrinsic ambipolarity in the ZOW model, the PENTA code, the DKES model.

Chapter 9

Collision Operator and Friction in the ZOW Model

The ZOW model[19] solves the radially-local drift-kinetic equation by the δf Monte-Carlo method, and the parallel friction $\mathcal{F}_{\parallel}$ is treated as follows. For the like-species collisions, the linearized collision operators are employed and this satisfies the parallel momentum balance, i.e., $\mathcal{F}_{\parallel,ee} = \mathcal{F}_{\parallel,ii} = 0$. For ion, the ion-electron friction $\mathcal{F}_{\parallel,ie}$ is neglected because of the large mass ratio, $m_e/m_i \ll 1$. For electron, in the previous work, the electron-ion collision was only approximated as the pitch-angle scattering operator with the stationary background Maxwellian ion distribution, i.e., $\mathcal{C}_{ei} \simeq \mathcal{L}_{ei}$. In the present work, not only the pitch-angle scattering but also the parallel ion mean flow $U_{\parallel,i}$ are newly employed[18],

$$\mathcal{C}_{ei} \cong \mathcal{L}_{ei} + \nu_D^{ei} \frac{m_e}{T_e} U_{\parallel,i} \nu_{\parallel} f_{e\mathcal{M}}. \tag{9.1}$$

according to Eq.(5.58). With the new $\mathcal{C}_{ei}$ operator, the electrons are exposed to the friction $\mathcal{F}_{\parallel,ei}$ which is roughly proportional to $(U_{\parallel,e} - U_{\parallel,i})$. In Eq.(9.1), the parallel

ion mean flow $U_{\parallel,i}$ is given as

$$U_{\parallel,i} = \frac{\langle U_{\parallel,i} B \rangle}{\langle B^2 \rangle} B + \left(\frac{1}{en} \frac{\partial p_i(\psi)}{\partial \psi} + \frac{\partial \Phi(\psi)}{\partial \psi} \right) \widetilde{U}_{\parallel}. \tag{9.2}$$

where $\langle \cdots \rangle$ represents a flux-surface average, and the pressure $p_i(\psi)$ and the electrostatic potential $\Phi(\psi)$ are assumed as the flux-surface functions. The second term in Eq. (9.2) represents the return flow of the diamagnetic and $E \times B$ flow, with the assumption that these flows are divergence-free on the flux-surface[38]. The $\widetilde{U}_{\parallel}$ term vanishes after taking the flux-surface average, i.e., $\left\langle B\widetilde{U}_{\parallel} \right\rangle = 0$. In Eq.(9.2), the term $\langle U_{\parallel,i} B \rangle$ is given from the ion simulations.

DKES solves the local and mono-energy drift-kinetic equation. Both ions and electrons implement the pitch-angle scattering in the their collision operators

$$\mathcal{C}_a \cong \sum_b \mathcal{L}_{a,b}. \tag{9.3}$$

Therefore, the momentum balance is not accurately satisfied in either the like- or the unlike-species collision. Besides the original DKES in the work, the DKES-like model is employed which is the DKES model with the same collision operators as the ZOW model. For the PENTA model[38], Sugama-Nishimura method[42] is adapted in order to re-interpret the diffusion coefficients from DKES so that the momentum conservation is satisfied, i.e., $\mathcal{F}_{\parallel,ii} = \mathcal{F}_{\parallel,ee} = 0$ and $\mathcal{F}_{\parallel,ei} = -\mathcal{F}_{\parallel,ie}$.

Ideally, the PENTA model reproduces the intrinsic-ambipolarity in an axisymmetric system. Verifications of the momentum correction method of PENTA and the new electron-ion collision operator in the ZOW model in aximmetric tokamak is presented in Appendix B.

Chapter 10

Application for the FFHR-d1 DEMO Reactor

10.1 Ion Parallel Flow

In Fig.10.1, the ZOW, DKES, and PENTA codes present the parallel flows under the candiate of FFHR-d1 self-ignition operation.[11] The scale of FFHR-d1 is about 4 times larger than LHD. The plasma parameters on the magnetic axis are $n_e = 2 \times 10^{20}/m^3$, $T = 15$ keV, $B_0 = 5.8$T, and $\beta_0 \simeq 6\%$. It is assumed that the ion and electron temperature are the same, and the pure deuterium plasma is assumed in order to simplify the neoclassical transport simulation. Note here that the bootstrap current effect on the MHD equilibrium is not taken into account in the simulations results shown in this chapter. The neoclassical transport simulations are carried out in the FFHR-d1 MHD equilibrium without toroidal current.

According to Eq.(6.14) and the models, the ion parallel flow depends on the viscosity balance,

$$\langle \boldsymbol{B} \cdot \nabla \cdot (\boldsymbol{P}_{\rm CGL} + \boldsymbol{\Pi}_2) \rangle_i \simeq 0. \tag{10.1}$$

In Fig.10.1(a), the parallel flow of the ZOW model agree with the PENTA well even

though the $\mathcal{F}_{\parallel,ie}$ is absent in the ZOW model. This suggests that the friction $\mathcal{F}_{\parallel,ie}$ is negligible as expected in the ZOW model in the Sec.9. Owing to the discrepancy between the DKES and the PENTA models in Fig.10.1(a), the momentum conservation is necessary even in the helical plasmas.

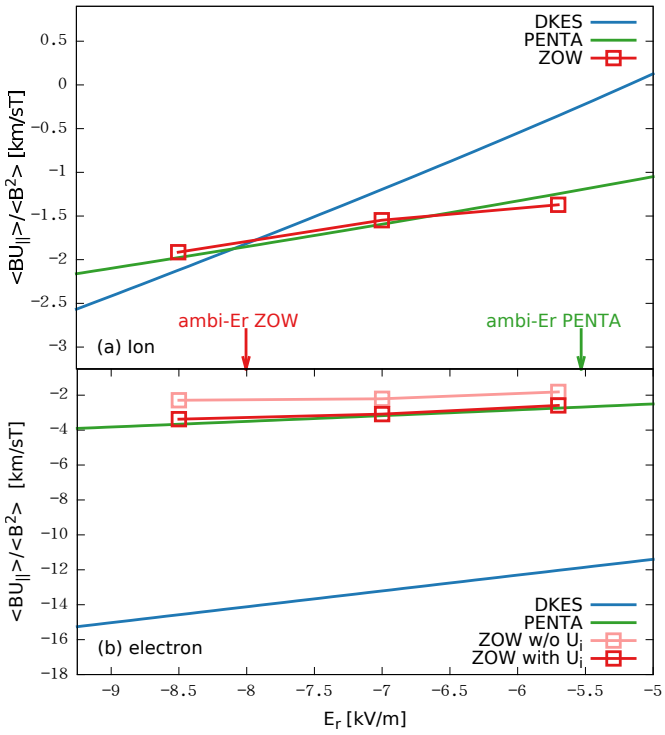

Figure 10.1: The dependence of the flux-surface average parallel mean flow $\langle BU_{\|}\rangle/\langle B^2\rangle$ on radial electric field : (a) deuterium ion and (b) electron. The "ambi-E_r" labels represent the vaules of ambipolar-E_r evaluated from the ZOW and PENTA simulations.

10.2 Electron Parallel Flow

For the electrons, in Fig.10.1(b), the two ZOW simulation results are employed to investigate the importance of the parallel ion mean flow $U_{\parallel,i}$. The electron parallel momentum equation is determined by

$$\langle \boldsymbol{B} \cdot \nabla \cdot (\boldsymbol{P}_{\mathrm{CGL}} + \boldsymbol{\Pi}_2) \rangle_e \simeq \langle \mathcal{F}_{\parallel,ei} B \rangle \tag{10.2}$$

according to Eqs.(6.15) and (6.16). The friction $\mathcal{F}_{\parallel,ei}$ with the finite $U_{\parallel,i}$ cause the difference between the two ZOW simulation results. The PENTA result agrees with the ZOW model with finite $U_{\parallel,i}$ better than the ZOW model without finite $U_{\parallel,i}$. The parallel momentum conservation is satisfied by finite $U_{\parallel,i}$ and the momentum correction of the like-species collision, respectively. The proper parallel mean flow $U_{\parallel,i}$ is necessary for the ZOW model to improve the collision operator on the electron parallel flow calculation. Fig.10.1(b) shows the difference between the DKES and the PENTA model as in the ion simulations.

10.3 Ambipolar Condition

In the estimation of neoclassical transport in helical plasmas, what is practically important is to find the ambipolar radial electric field $E_{amb}(r)$ which is determined by the condition $\sum e_a \Gamma_a(r, E_r) = 0$, and the radial profiles of Γ_a, Q_a, and the bootstrap current in the ambipolar condition. Here, the ambipolar neoclassical transport in the FFHR-d1 canse is compared among the local models.

In Fig.10.2, the ambipolar-E_r radial profile of ZOW, DKES, and PENTA simulation results are shown. In this section, the result of GSRAKE code, which is used to investigate the operation scenario of FFHR-d1 presently[11], is presented for reference, too. They shows the similar negative-E_r profile, which are the ion-roots. In

Fig10.3, the ion and electron parallel flows at the ambipolar conditions are presented, respectively. According to the parallel flow profiles, in Fig.10.4, the radial profile of the bootstrap current in the FFHR-d1 case is estimated by the ZOW, PENTA, and DKES models. The bootstrap current from the ZOW model with finite $U_{\parallel,i}$ agrees with PENTA. In the previous studies[29, 19] it is found that neglecting the tangential magnetic drift in DKES and PENTA causes the overestimation of the ion radial particles flux when E_r is small. This results in the difference in the ambipolar-E_r values as shown in Fig.10.1. However, in the present case, since $\langle BJ_\parallel \rangle = \langle Bne(U_{\parallel,i} - U_{\parallel,e}) \rangle$ from the ZOW model and PENTA have very weak dependence on E_r, the bootstrap current from these two codes agrees each other. The DKES result shows approximately 10 times larger magnitude of the bootstrap current than those from PENTA and the ZOW models.

In Fig.10.5, the radial profile of radial flux is present. In Fig.10.6 and 10.7, the heat fluxes of ion and electron both show the simular tendcy as the radial flux in Fig.10.5. In Fig.10.5, the momentum-correction does not affect the radial flux obviously compared to the bootstrap current. However, it shows that the radial flux of the PENTA model is still twice as large as the ZOW. As it is discussed in Sec. 7, the effect of the tangential magnetic drift on the determination of the ambipolar condition is expected to be more significant in FFHR-d1 than LHD. It is exected that the ZOW model will reproduce the dependence of Γ_i on E_r close to the global caclulation than DKES. Since PENTA relies on the DKES calculation result, it has the same problem as DKES code when $v_E \sim v_m$ or $\mathcal{M}_p \sim \mathcal{O}(1)$. However, to check which local model is closer to the global simulation result at the ambipolar condition, it requires the huge amount of computation resource to conduct the global code, especially to evaluate the ion mean flow $U_{\parallel,i}$. This issue will be studied in future work.

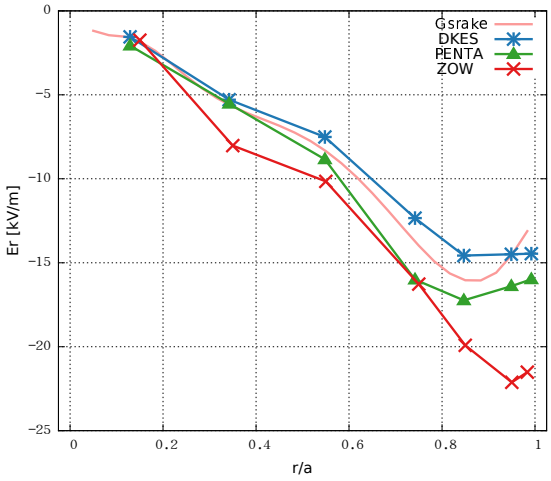

Figure 10.2: The electric field profile in FFHR-d1

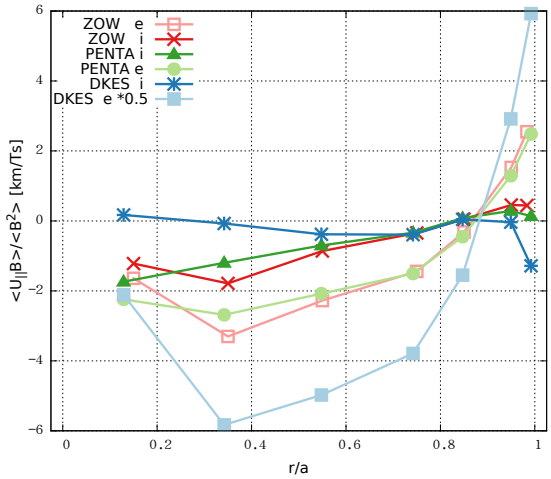

Figure 10.3: The parallel flow profile in FFHR-d1. The DKES result is multiplied by 0.5.

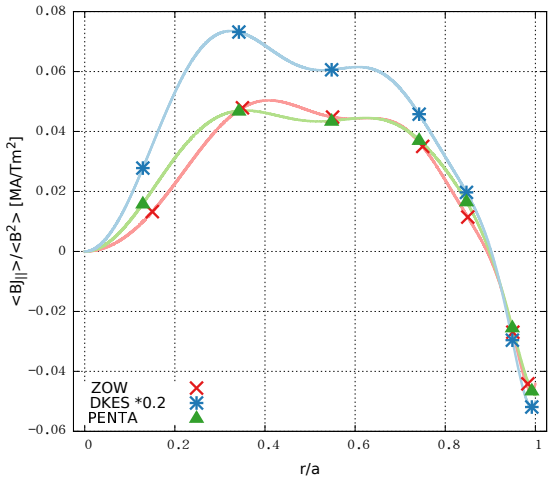

Figure 10.4: The radial profile of the bootstrap current. The DKES result is multiplied by 0.2.

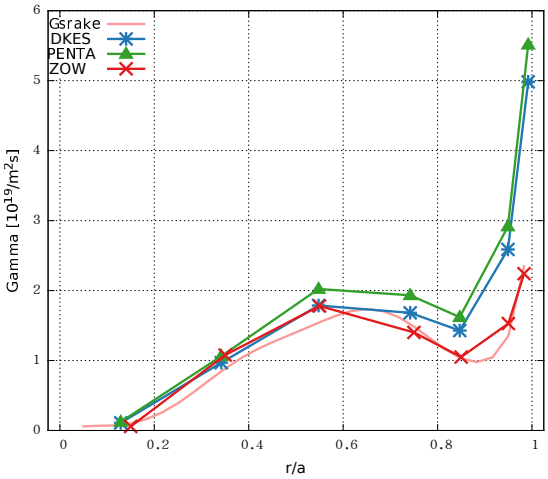

Figure 10.5: The radial flux profile in FFHR-d1

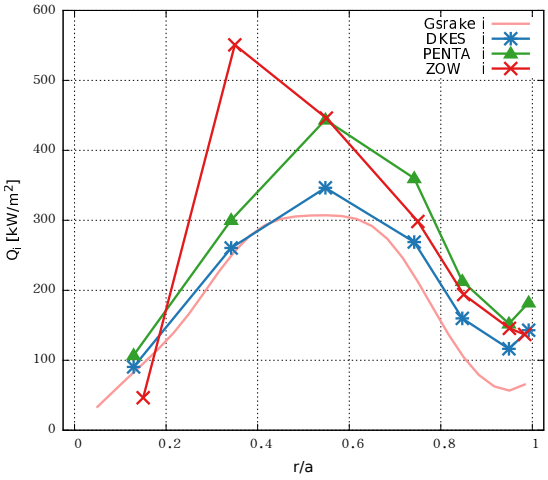

Figure 10.6: The ion energy flux profile in FFHR-d1

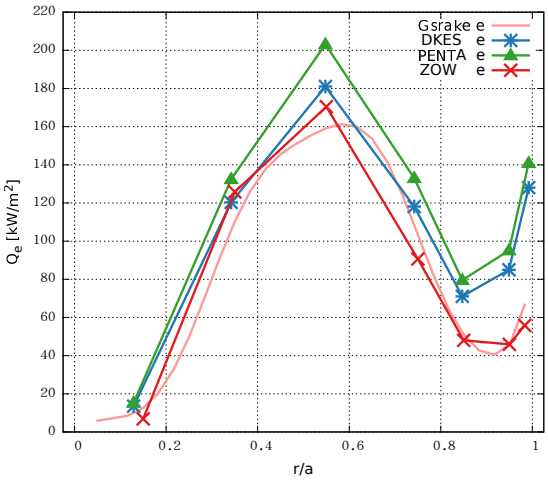

Figure 10.7: The electron energy flux profile in FFHR-d1

10.4 Collision Frequency Dependence

In this section, the collision dependence of bootstrap current in FFHR-d1 Demo are presented with the density which is four times denser than the particle density shown in Sec. 10.1.To keep the plasma β value, the temperature is reduced by a factor of 4. Therefore,the MHD equilibrium for test is the same as in Sec. 10.1. Note that this choice of plasma parameter is not realistic for the helical reactor. We use this case merely to study the effect of collisions on bootstrap current. Because the collision frequency $\nu \propto n/T^{3/2}$, it increases 32 times from the original self-ingnition condition.

In Fig.10.8, the ion and electron parallel flows are presented by the ZOW, DKES, and PENTA models. In Fig.10.9, the bootstrap current are obtained from the results in Fig.10.8. As the discussion in Sec.10.3, the ZOW and PENTA models agrees with each other again. The maximum amplitude of $\langle BJ_{\parallel}\rangle/B^2$ on DKES is roughly ten times as large as those from the ZOW and PENTA models. The positive peak magnitude of bootstrap current density in PENTA and ZOW are both five times lower than those in the original case in Fig.10.4. Consider the total toroidal current I_t in FFHR-d1 Demo. They are evaluated by integrating the current density from the magnetic axis to the plasma boundary. According to Table 10.1, the amplitude of total toroidal currents I_t of ZOW and PENTA are decreased roughly by a factor of ten. The negative I_t in the collisional case is due to the large negative $\langle BJ_{\parallel}\rangle$ at $r/a > 0.8$.

In the present benchmark, we do not try the self-consistent simulation between the MHD equilibrium and bootstrap current. However, we find that the operation under the high collision frequency is preferable to suppress the bootstrap current in FFHR-d1 Demo.

	$I_t[MA]$	
model / density	n	n_c
PENTA	1.924	−0.188
DKES	13.85	0.251
ZOW	1.845	−0.203

Table 10.1: The total toroidal current I_t in FFHR-d1. The plasma density n and the temperature T of the original self-ignition case in Table 6.1 is taken as the reference. In the high collision frequency test, the plasma density n_c and the temperature T_c are given as $n_c = n * 4$, $T_c = T/4$ and $n_c * T_c = const.$

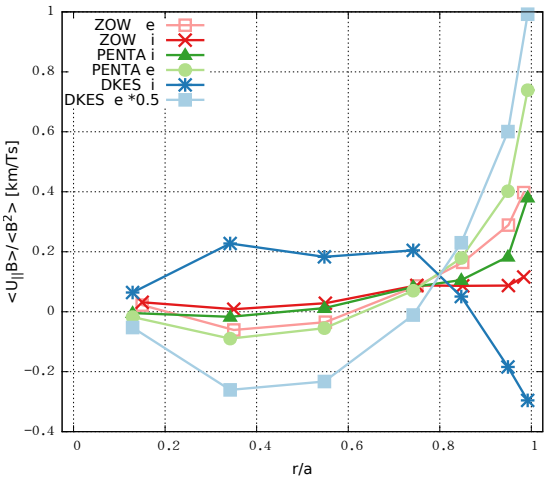

Figure 10.8: The ion and electron parallel flows in FFHR-d1 with the density n_c. The DKES result is multiplied by 0.5

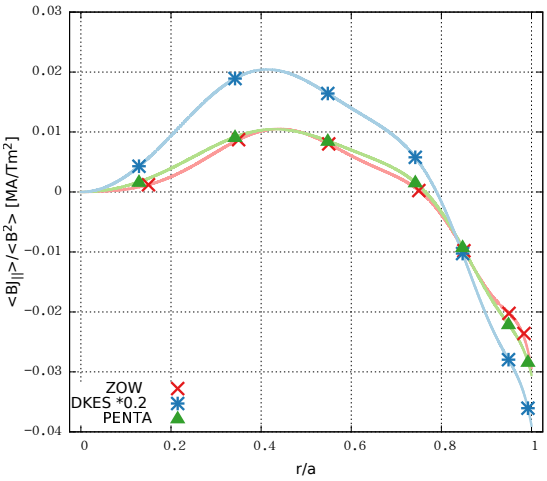

Figure 10.9: The bootstrap current in FFHR-d1 with the density n_c. The DKES result is multiplied by 0.2

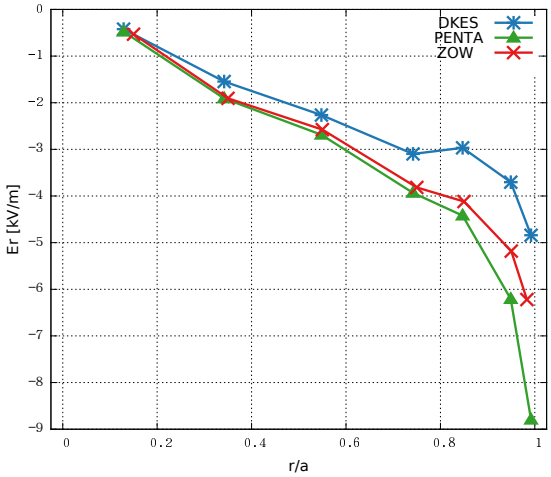

Figure 10.10: The electric field profile in FFHR-d1 with the density n_c.

Chapter 11

Conclusions of Part II

It is demonstrated that the pitch-angle scattering operator is sufficient for evaluating the radial transport but it is insufficient for the bootstrap current calculation in the helical plasmas. The collision operator is implemented as Eq.(9.1) in the ZOW model. Besides the pitch-angle scattering, the proper friction is necessary to improve the collision operator of the simulation, especially for the parallel electron mean flow. The present study shows that both the momentum conservation in the like-species collision and the friction on the electrons are important physics to estimate the bootstrap current precisely. Furthermore, the ZOW model with the finite $U_{\parallel,i}$ and the PENTA models present the intrinsic ambipolarity in the symmetric system as shown in Appendix B. For the PENTA model, this is verification of the Sugama-Nishimura method in the symmetric system. For the ZOW model, this demonstrates the reliability of the new collision operator.

In the benchmark of the bootstrap current calculation in the FFHR-d1 case, a good agreement between the ZOW model and PENTA are found. However, as demonstrated in Appendix B, the PENTA simulation is affected by the incompressible-$E \times B$ approximation used in DKES code when E_r as the poloidal Mach number $\mathcal{M}_p$ increases. Therefore, the applicability of the ZOW model for wider range of

$\mathcal{M}_p$ value than DKES and PENTA codes can be regarded as the advantage of the model, especially when we consider the ion impurity effect on the bootstrap current and the radial fluxes in the future helical reactor, since $\mathcal{M}_p$ becomes larger for heavy ions.

Following the demonstration in Sec.10.4, the magnitude of bootstrap current can be decreased by increasing the collision frequency. The simulation shows that the high collision frequency is preferable for suppressing the bootstrap current in FFHR-d1 Demo. According to the knowledge found in this study, a more collisional and low-β operation scenario than the self-ignition example used here is recently proposed in the study of the operation seraglio of FFHR-d1, in which $\beta_0 \sim 2.5\%$ and the fusion gain is expected to be $Q \sim 10$ [12]. It is shown in the work that the bootstrap current amplitude solved self-consistently with the MHD equilibrium in the $Q \sim 10$ case is reduced to the same level as in the high-collisionality case shown in Sec.10.4, Fig.10.9. The present verification of the ZOW model and PENTA code contributes to increasing the reliability of the numerical simulations applied to such prediction studies of the operation of future reactors.

Chapter 12

Summary

12.1 Verification of the Neoclassical Transport Models in Helical Plasmas

The drift-kinetic models in helical plasmas are benchmarked via the series of the neoclassical transport simulations. Here, the drift-kinetic models are the ZOW, ZMD, DKES-like, and global models. The helical device geometries of LHD, W7-X, and HSX are employed in the benchmarks. The two-weight delta-f scheme is employed to carry out the calculations of particle flux, energy flux, and parallel flow. The global model solves the drift-kinetic equation in 5-dimensional phase space (3D in position $\times$ 2D in the velocity space) which solves the exact guiding-center trajectories in the phase space. The local models adopt approximation in the guiding-center trajectories so as to reduce the dimension of the problem from 5 to 4 or 3. The Zero-Orbit-Width (ZOW) model drops the radial component of magnetic drift motion while it maintains the tangential component to the flux surface. In the ZMD and the DKES-like models, the magnetic drift is completely neglected, but instead the phase-space volume is conserved. Furthermore, the kinetic energy is taken as constant parameter in the DKES-like model. The ZOW model breaks the Liou-

ville's theorem because of the compressible phase-space flow. On the contrary, in the ZMD and the DKES models, the phase-space volume is conserved. We adopted a new delta-f method which enables the two-weight scheme adaptable to the case in which the phase-space volume is not conserved. In the ZOW model, the variation in the phase-space volume is estimated to bring the $\mathcal{O}(\delta^2)$ extra contributions in the particle, parallel momentum, and energy balance equations, where δ is a small ordering parameter in the drift-kinetic theory. The simulation results have demonstrated that the ZOW and the ZMD models agree with each other well in the wide range of E_r magnitude. This proves that the $\mathcal{O}(\delta^2)$ contributions are indeed negligible in neoclassical transport calculation. Around $E_r \sim 0$, the ZMD and DKES-like models show the extra large neoclassical flux peaks. Owing to the tangential magnetic drift in the ZOW model, the radial fluxes and parallel flows around $E_r \sim 0$ are smoothly dependent on E_r and similar to the global results.

The effects of the tangential magnetic drift become stronger under the following conditions. First, the effect is related to the magnetic geometry and it is more obvious in LHD than in W7-X and HSX. In W7-X and HSX, the magnetic configuration is optimized in order to reduce the radial drift of trapped particles. This reduces the magnitude of the particle fluxes at the poloidal resonance around $E_r \sim 0$. Then, the difference strength of the poloidal resonance results in the small gap between the ZMD and the ZOW models in these machines compared to LHD. Second, the effect is obvious in the lower collision frequency case. Around $E_r \sim 0$, the tangential magnetic drift helps to avoid the poloidal resonance. Otherwise, the artificially strong $1/\nu$-type neoclassical transport will occur. Third, the ZOW model agrees with the ZMD, and DKES-like models in the electron simulations. The discrepancies of the simulation occur on the ions only. This suggests that the conventional local drift-kinetic models are sufficient for electron simulation.

It is found that the difference treatment of the $\boldsymbol{E} \times \boldsymbol{B}$ drift term is related to the error in the neoclassical transport calculation. In the DKES-like model, the

incompressible $\boldsymbol{E}\times\boldsymbol{B}$ drift assumption causes the mis-estimation of the neoclassical transport as the poloidal Mach number is larger than 0.4, $\mathcal{M}_p > 0.4$. Due to the mass dependency of $\mathcal{M}_{p,a} > v_E/v_{th,a}$, the $\mathcal{M}_p$ increases for the heavy ion. Therefore, the parameter window in which the incompressible-$\boldsymbol{E}\times\boldsymbol{B}$ approximation is valid will be narrower for the heavier species $\boldsymbol{E}\times\boldsymbol{B}$.

Regarding the practical application, the neoclassical flux and bootstrap current are evaluated at the ambipolar condition. The ion-root usually exists as $T_i \simeq T_e$; the electron-root that appears as $E_r \sim 0$ in low-collisionality plasma is an artifact in the ZMD and the DKES-like models. The magnitude of the ratio T_e/T_i represents $T_i \ll T_e$. The strong ion particle flux peaks at the threshold of the transition between the ion-root and the electron-root. The benchmark result suggests that the T_e/T_i threshold will be lower in the global and the ZOW models than in the ZMD and the DKES models. The neoclassical transport varies drastically if the ambipolar-E_r switches from an ion-root to an electron-root. Therefore, the introduction of the tangential magnetic drift in a local code plays an important role in investigating the ambipolar-root transition. According to the simulations, the magnetic drift slightly affects the parallel flow and the bootstrap current evaluation. However, the sign of the bootstrap current may change when the ambipolar-E_r transits from a negative to a positive root. Then, the accurate expectation for the ambipolar-E_r is also important for bootstrap current evaluation in helical plasmas.

In the simulations, steady-state solution of parallel flow is obtained by the parallel momentum balance equation. For the ZOW model, the extra terms, from comprehensibility in the phase space and the viscosity, do not influence the parallel flow. Compared to the radial flux, the magnetic drift does not influence the parallel flow strongly at $E_r \sim 0$, even in the low-collisionality LHD and W7-X cases. On the other hand, the discrepancies of parallel flows at large-$\mathcal{M}_p$ appear as clearly as that of the radial flux. The resonance occurs on trapped particles, which cannot contribute to parallel flow. The influence of resonance is passed to the passing particles via

collisions to change the momentum balance. The parallel flows peak at $E_r = 0$ is much less than the radial flux peaks because it is driven by this indirect mechanism.

In the work, it is found that the tangential magnetic drift not only decreases the magnitude of the particle fluxes peak but also changes the peak position. Since the discharge temperature could be up to $T_i > 10$ keV in the FFHR-d1 helical reactor, it is anticipated that the radial ion flux peak in the ZOW model will tend to appear much more negative E_r side than that in LHD. This is related to the ion-root E_r magnitude. Therefore, the difference between the ZOW and ZMD models becomes significant to evaluate the neoclassical transport in the ambipolar condition.

This work demonstrates the advantage of ZOW as follows. (1) The ZOW model is able to mitigate the unphysical behavior in the radial neoclassical flux around $E_r \sim 0$, and (2) it also improves the reliability of the bootstrap current evaluation in helical plasmas compared to the conventional local models, i.e., ZMD and DKES. ZOW also reduces the computation cost compared to the global model.

12.2 Applications of the ZOW Model to Bootstrap Current Calculations

The importance of the parallel momentum conservation on the bootstrap current evaluation in nonaxisymmetric systems is demonstrated by the benchmarks among the local drift-kinetic equation solvers, i.e., the Zero-Orbit-width (ZOW), DKES, and PENTA codes. The verification and application are carried out in an FFHR-d1 helical DEMO reactor case. The ZOW model is extended to include the ion parallel mean flow effect on the electron-ion parallel friction. In the DKES model, collision term is approximated by the pitch-angle-scattering operator, which does not ensure the momentum balance. The PENTA model employs the Sugama-Nishimura method to correct the momentum balance of the DKES results. The ZOW and

PENTA models agree with each other well on the calculations of the bootstrap current. The DKES results without the parallel momentum conservation deviate significantly from those from the ZOW and PENTA models. It is well-known that the pitch-angle scattering operator is enough to evaluate the radial neoclassical fluxes in helical plasmas. In the present study, however, it is clearly demonstrated that the pitch-angle scattering operator is insufficient for the bootstrap current calculation. The present study shows that both the momentum conservation in the like-species collision and the friction on the electrons are the important physics for estimating the bootstrap current correctly. The electron-ion collision operator in the ZOW model drift-kinetic equation is improved in order to treat the correct friction force on the electrons with the ions which have finite parallel mean flow. This work is also the first report of verification of the ZOW and PENTA for bootstrap current calculations. It is demonstrated that the PENTA result agrees with the result of ZOW with the improved electron-ion collision operator. These two codes will serve to improve the accuracy of the bootstrap current calculation in general helical plasmas. In the application for FFHR-d1, it is found that the magnitude of the bootstrap current becomes the order of MA, which may affect the MHD equilibrium. However, the application for FFHR-d1 demonstrates that the bootstrap current is drastically reduced by choosing a more collisional operation scenario.

Appendix A

Derivation of Viscosity Tensor

The parallel moment equation is derived from Eq.(4.1) with $\mathcal{A} = mv_\parallel$,

$$\begin{aligned}
&\frac{\partial}{\partial t}\left(\int d^3v f m v_\parallel\right) + \nabla\cdot\left(\int d^3v f m v_\parallel \dot{\boldsymbol{X}}\right) \\
&= \left(\int d^3v f m \dot{v}_\parallel\right) + \left(\int d^3v f m v_\parallel [\mathcal{S}+\mathcal{C}]\right) \\
&+ \int d^3v f m v_\parallel \mathcal{G}.
\end{aligned} \tag{A.1}$$

With $\dot{v}_\parallel$ in the global model, Eq.(4.27), we have the following relation

$$\begin{aligned}
&\nabla\cdot\left(\int d^3v f m v_\parallel \dot{\boldsymbol{X}}\right) - \left(\int d^3v f m \dot{v}_\parallel\right) \\
&= \nabla\cdot\left(\int d^3v f m v_\parallel^2 \boldsymbol{b}\right) + \int d^3v f \boldsymbol{b}\cdot(\mu\nabla B - e_a \boldsymbol{E}) \\
&+ \nabla\cdot\left(\int d^3v f m v_\parallel \dot{\boldsymbol{X}}_\perp\right) - \int d^3v f m v_\parallel \dot{\boldsymbol{X}}_\perp\cdot\boldsymbol{\kappa} \\
&= \boldsymbol{b}\cdot\left\{\nabla\cdot\left(\int d^3v f\left[m v_\parallel^2 \boldsymbol{b}\boldsymbol{b} + \mu B\left(\boldsymbol{I}-\boldsymbol{b}\boldsymbol{b}\right)\right]\right)\right\} \\
&+ \boldsymbol{b}\cdot\left\{\nabla\cdot\left[\int d^3v f m v_\parallel\left(\boldsymbol{b}\dot{\boldsymbol{X}}_\perp + \dot{\boldsymbol{X}}_\perp \boldsymbol{b}\right)\right]\right\} \\
&- e_a E_\parallel \int d^3v f.
\end{aligned} \tag{A.2}$$

Then, with $\mathcal{G} = 0$ in the global model, Eq.(4.25) is obtained by rewriting Eq.(A.1),

$$\begin{aligned}&\frac{\partial}{\partial t}(nmV_\parallel) + \boldsymbol{b}\cdot(\nabla\cdot\boldsymbol{P})\\&= ne_aE_\parallel + F_\parallel + \int d^3v\ \mathcal{S}mv_\parallel,\end{aligned} \tag{A.3}$$

where

$$\boldsymbol{P} \equiv \boldsymbol{P}_{CGL} + \boldsymbol{\Pi}_2, \tag{A.4a}$$

$$\boldsymbol{P}_{CGL} \equiv \int d^3v\ [(mv_\parallel^2\boldsymbol{bb} + \mu B(\boldsymbol{I} - \boldsymbol{bb})]f, \tag{A.4b}$$

$$\boldsymbol{\Pi}_2 \equiv \int d^3v\ mv_\parallel\left(\dot{\boldsymbol{X}}_\perp\boldsymbol{b} + \boldsymbol{b}\dot{\boldsymbol{X}}_\perp\right)f. \tag{A.4c}$$

It should be noted that the $\dot{\boldsymbol{X}}_\perp\cdot\boldsymbol{\kappa}$ term in Eq.(A.2) is involved in the symmetry of the $\boldsymbol{\Pi}_2$ tensor. On the other hand, Eq.(A.2) is independent of the explicit form of $\dot{\boldsymbol{X}}_\perp$.

For the ZOW model, the parallel momentum balance equation is calculated with $\dot{\boldsymbol{X}}_{ZOW} = v_\parallel\boldsymbol{b} + \boldsymbol{v}_E + \hat{\boldsymbol{v}}_m$ and

$$\begin{aligned}\dot{v}_\parallel = &-\frac{1}{m}\boldsymbol{b}\cdot(\mu\nabla B) + v_\parallel\boldsymbol{v}_E\cdot\frac{\nabla_\perp B}{B} = -\frac{1}{m}\boldsymbol{b}\cdot(\mu\nabla B) + v_\parallel\dot{\boldsymbol{X}}_{ZOW}\cdot\boldsymbol{\kappa}\\&- v_\parallel\left(\dot{\boldsymbol{X}}_{ZOW}\cdot\boldsymbol{\kappa} - \boldsymbol{v}_E\cdot\frac{\nabla_\perp B}{B}\right).\end{aligned} \tag{A.5}$$

Then, the last term in Eq.(A.5) is rewritten as

$$\begin{aligned}&\dot{\boldsymbol{X}}_{ZOW}\cdot\boldsymbol{\kappa} - \boldsymbol{v}_E\cdot\frac{\nabla_\perp B}{B}\\&= (\hat{\boldsymbol{v}}_m + \boldsymbol{v}_E)\cdot\boldsymbol{\kappa} - \boldsymbol{v}_E\cdot\frac{\nabla_\perp B}{B}\\&= (\hat{\boldsymbol{v}}_m + \boldsymbol{v}_E)\cdot\left(\frac{\nabla_\perp B}{B} + \frac{\mu_0\boldsymbol{J}\times\boldsymbol{B}}{B^2}\right) - \boldsymbol{v}_E\cdot\frac{\nabla_\perp B}{B}\\&= [\boldsymbol{v}_m\cdot(\boldsymbol{I} - \nabla\psi\boldsymbol{e}_\psi)]\cdot\left(\frac{\nabla_\perp B}{B} + \frac{\mu_0\nabla p}{B^2}\right) + \boldsymbol{v}_E\cdot\frac{\mu_0\nabla p}{B^2}\\&= -\frac{1}{B}\frac{\partial B}{\partial\psi}\dot{\psi}.\end{aligned} \tag{A.6}$$

Therefore, Eq.(4.30) is obtained. Here, according to the low-β approximation $\boldsymbol{\kappa} \simeq \nabla_\perp B/B$, the magnetic drift is approximated as

$$\boldsymbol{v}_m \simeq \boldsymbol{B} \times \nabla B \frac{mv^2}{2e_a B^3} \left(1 + \xi^2\right). \tag{A.7}$$

Using this $\dot{v}_\parallel$ for the ZOW model, Eq.(A.2) is rewritten as

$$\begin{aligned}
&\frac{\partial}{\partial t}\left(\int d^3v f m v_\parallel\right) \\
&+ \boldsymbol{b}\cdot\nabla\cdot\left[\boldsymbol{P}_{CGL} + \boldsymbol{\Pi}_{2.\mathrm{ZOW}}\right] \\
&= F_\parallel + \left(\int d^3v f m v_\parallel \mathcal{S}\right) + \left(\int d^3v f m v_\parallel \mathcal{G}\right) \\
&+ \left(\int d^3v f m v_\parallel \frac{1}{B}\frac{\partial B}{\partial \psi}\dot{\psi}\right),
\end{aligned} \tag{A.8}$$

where

$$\begin{aligned}
&\boldsymbol{b}\cdot\nabla\cdot\boldsymbol{\Pi}_{2,\mathrm{ZOW}} \\
&= \boldsymbol{b}\cdot\left\{\nabla\cdot\left[\int d^3v\ f\ m\ v_\parallel\ \left(\boldsymbol{b}\dot{\boldsymbol{X}}_{\perp,ZOW} + \dot{\boldsymbol{X}}_{\perp,ZOW}\boldsymbol{b}\right)\right]\right\}.
\end{aligned} \tag{A.9}$$

For the ZMD model, the parallel momentum balance equation is calculated with $\dot{\boldsymbol{X}}_{\mathrm{ZMD}} = v_\parallel \boldsymbol{b} + \boldsymbol{v}_E$ and

$$\dot{v}_\parallel = -\frac{1}{m}\boldsymbol{b}\cdot(\mu\nabla B) + v_\parallel \boldsymbol{v}_E \cdot \frac{\nabla_\perp B}{B}. \tag{A.10}$$

Because of the difference of $\dot{\boldsymbol{X}}_\perp$ between ZOW and ZMD, one finds that

$$\begin{aligned}
&\boldsymbol{v}_E\cdot\frac{\nabla_\perp B}{B} - \dot{\boldsymbol{X}}_{\mathrm{ZMD}}\cdot\boldsymbol{\kappa} \\
&= \boldsymbol{v}_E\cdot\frac{\nabla_\perp B}{B} - \boldsymbol{v}_E\cdot\left(\frac{\nabla_\perp B}{B} + \frac{\mu_0 \boldsymbol{J}\times\boldsymbol{B}}{B^2}\right) \\
&= 0.
\end{aligned} \tag{A.11}$$

Then, the parallel momentum balance equation fo the ZMD model becomes

$$\begin{aligned}&\frac{\partial}{\partial t}(nmV_\parallel B) + \boldsymbol{B}\cdot\nabla\cdot(\boldsymbol{P}_{\mathrm{CGL}} + \boldsymbol{\Pi}_{2,\mathrm{ZMD}})\\ &= F_\parallel B + B\int d^3v\ \mathcal{S}_1\ mv_\parallel,\end{aligned} \tag{A.12}$$

where

$$\begin{aligned}&\boldsymbol{b}\cdot\nabla\cdot\boldsymbol{\Pi}_{2,\mathrm{ZMD}}\\ &= \boldsymbol{b}\cdot\nabla\cdot\left[\int d^3v f m v_\parallel\left(\boldsymbol{b}\dot{\boldsymbol{X}}_{\perp,\mathrm{ZMD}} + \dot{\boldsymbol{X}}_{\perp,\mathrm{ZMD}}\boldsymbol{b}\right)\right]\\ &= \boldsymbol{b}\cdot\nabla\cdot\left[nmV_\parallel\left(\boldsymbol{b}\boldsymbol{v}_E + \boldsymbol{v}_E\boldsymbol{b}\right)\right].\end{aligned} \tag{A.13}$$

Note that Eq.(A.13) is equivalent to Eq.(33) in Ref[23].

For the DKES model, the parallel momentum balance equation is calculated with $\dot{\boldsymbol{X}}_{DKES} = v_\parallel\boldsymbol{b} + \hat{\boldsymbol{v}}_E$ and

$$\dot{v}_\parallel = -\frac{1}{m}\boldsymbol{b}\cdot(\mu\nabla B), \tag{A.14}$$

which lacks in the $\dot{\boldsymbol{X}}\cdot\boldsymbol{\kappa}$ term. Therefore, the balance equation of parallel momentum becomes

$$\begin{aligned}&\frac{\partial}{\partial t}\left(\int d^3v f m v_\parallel\right) + \boldsymbol{b}\cdot\nabla\cdot[\boldsymbol{P}_{CGL} + \boldsymbol{\Pi}_{2.\mathrm{DKES}}]\\ &= F_\parallel + \left(\int d^3v f m v_\parallel\mathcal{S}\right) - nmV_\parallel\hat{\boldsymbol{v}}_E\cdot\boldsymbol{\kappa},\end{aligned} \tag{A.15}$$

where $\boldsymbol{\Pi}_{2,\mathrm{DKES}}$ is

$$\boldsymbol{b}\cdot\nabla\cdot\boldsymbol{\Pi}_{2,\mathrm{DKES}} = \boldsymbol{b}\cdot\left\{\nabla\cdot\left[nmV_\parallel\left(\boldsymbol{b}\hat{\boldsymbol{v}}_E + \hat{\boldsymbol{v}}_E\boldsymbol{b}\right)\right]\right\}. \tag{A.16}$$

Note that $\boldsymbol{b}\cdot\nabla\cdot\boldsymbol{\Pi}_{2.\mathrm{DKES}} + nmV_\parallel\hat{\boldsymbol{v}}_E\cdot\boldsymbol{\kappa}$ is equivalent to Eq.(34) in Ref[23], and in the derivations shown in Appendix A, we use assumptions $p = p(\psi)$, $\boldsymbol{J}\times\boldsymbol{B} = \nabla p$,

and $\boldsymbol{E} = -\nabla\Phi(\psi)$.

In conclusion, if we define the $\mathbf{\Pi}_2$ as a symmetric tensor in local models, an extra term appears in the right-hand-side of the parallel momentum balance equation for the ZOW and DKES models.

Appendix B

Benchmark of the Intrinsic Ambipolarity in Tokamak Geometry

In axisymetric tokamak, the neoclassical flux is defined as

$$\langle \Gamma_a \cdot \nabla\psi \rangle \equiv -I \left\langle \frac{F_{a,\parallel} + n_a e_A E_\parallel}{e_a B} \right\rangle, \tag{B.1}$$

where $I(\psi) = RB_\psi$. Then,

$$\sum_a e_a \langle \Gamma_a \cdot \nabla\psi \rangle = 0 \tag{B.2}$$

because of

$$\sum_a \boldsymbol{F}_a = 0 \quad \text{and} \quad \sum_a e_a n_a = 0.$$

Eq.(B.2) shows the intrinsic ambipolarity. The other important property of neoclassical transport in tokamak is that the radial fluxes and bootstrap current are independent of the radial electric field, as far as the momentum conservation property of collision operator and the slow-flow ordering $v_E \ll v_{th}$ are satisfied. For

example, the ion heat flux in the large-aspect-ratio limit in the banana regime is given as

$$\langle \boldsymbol{q}_i \cdot \nabla\psi \rangle = -0.92 f_t \frac{n_i T_i I^2}{m_i \Omega_i^2} \frac{dT_i}{d\psi} \tag{B.3}$$

where $x \equiv v/(v_{th,i})$ and the effective fraction of trapped particle is denoted as f_t. Since the momentum conservation is the essential physics in these properties, benchmarking the drift-kinetic models in a tokamak geometry is a good demonstration to prove that the collision operator works correctly.

In the benchmark, a circular cross section tokamak is considered. The plasma parameters used in the simulations are shown in Table B.1. We benchmark the original DKES code, PENTA code, and the ZOW model. The PENTA code utilizes with Sugama-Nishimura method in Sec. 9. The ZOW models is extended to two types: with and without the finite ion parallel flow $U_{\parallel,i}$ in the electron-ion collision operator Eq.(9.1). In the section, the intrinsic ambipolarity in tokamak is demonstrated in order to examine the momentum conservation property in each models.

In Fig.B.1, the ion radial fluxes are shown and there are three trendies. First, the result of ZOW shows the independence of the magnitude of E_r. As discussed in Eq.(B.1), Γ_i depends on the ion-electron friction $F_{ie,\parallel}$. Since $F_{ie,\parallel}$ is neglected in the ZOW model, the magnitude of ion raidal flux is almost zero. Second, the result of DKES is strongly proportional of the magnitude of E_r. This shows the pitch angle scattering is deficient to evaluate the ion radial flux in tokamak. Third, the results of DKES-like and PENTA are constant for small E_r but they depend on E_r at $E_r > 4$ kV/m. The tendency can be consider as the effect of incompressible-$\boldsymbol{E} \times \boldsymbol{B}$ as discussed in Part I. The Γ_i magnitude of DKES-like model is nearly zero for samll-E_r, because it employees the same collision operator as ZOW which conserves the parallel momentum in the ion-ion collisions. In contrast to DKES-like and ZOW, the momentum correction method of PENTA takes $F_{ie,\parallel}$ into account. This leads to the finite Γ_i in PENTA at $|E_r| < 4$ kV/m.

In Fig.B.2, the electron radial fluxes are shown and there are two groups:(1) ZOW with $U_{\parallel,i}$, PENTA, DKES-like with $U_{\parallel,i}$ and (2) DKES, and DKES-like. The result of the first group is independent of the magnitude of E_r but the second shows opposite results. This implies that the requirement of the electron-ion friction with finite $U_{i,\parallel}$ in the calculation of electron neoclassical transport. In contrast with Γ_i in Fig.B.1, in Fig.B.2 the effect of incompressible $\boldsymbol{E}\times\boldsymbol{B}$ is weak. It comes from the difference in the poloidal Mach number of ion and electron. In the work, we assume the same temperature of ion and electron, $T_i = T_e$. Then, the velocity of ion and electron becomes $v_{th,i} \ll v_{th,e}$ because of mass ratio. Therefore, $\mathcal{M}_{p,i} \gg \mathcal{M}_{p,e}$.

According to Figs.B.1 and B.2, the intrinsic ambipolarity $\Gamma_i = \Gamma_e$ is satisfied only in the PENTA calculation at at $|E_r| < 4$ kV/m. This demonstrates that the momentum conservation not only in like-species collisions, $F_{\parallel,ii} = F_{\parallel,ee} = 0$, but also the exact momentum transfer between ions and electrons, $F_{\parallel,ie} = -F_{\parallel,ei}$, are necessary to reproduce the intrinsic ambipolarity.

In Figs.B.3 and B.4, the tendencies of ion and electron energy fluxes are similar to those of the radial fluxes, respectively. In the ion energy fluxes, finite and constant difference is found between the results of PENTA and ZOW. Since $\Gamma_i \simeq 0$ in ZOW, this small discrepancy will be attributed to the convective part in the energy flux, $Q_i = q_i + \frac{5}{2}\Gamma_i T_i$, where q is the conductive heat flux.

In Fig.B.5, the the ion parallel flow $\langle BU_\parallel\rangle_i$ and electron parallel flow $\langle BU_\parallel\rangle_e$ from all the models are plotted. It can be seen that the parallel flows have linear dependence on E_r. Then, Fig.B.6 is obtained by

$$\frac{\langle BU_\parallel\rangle_i - \langle BU_\parallel\rangle_e}{B^2} \propto \langle BJ_\parallel\rangle. \tag{B.4}$$

The bootstrap current simulations are divided into parts:(1) ZOW with $U_{\parallel,i}$, PENTA, DKES-like with $U_{\parallel,i}$ and (2) DKES, and DKES-like. The result of the first group does not depends on the magnitude of E_r as the analytic theory predicts. The boot-

strap current are constant if the momentum conservation is satisfied by Sugama-Nishimura method or if $F_{\parallel,ei}$ with finite $U_{\parallel,i}$ is considered. The result of DKES depends on the magnitude of E_r slightly and the DKES-like model without $U_{\parallel,i}$ cannot evaluate the bootstrap current correctly. DKES-like with and without the finite $U_{\parallel,i}$ consider the same like-species collision operator, $\mathcal{C}_{ii}$ and $\mathcal{C}_{ee}$. The only difference is that the $U_{\parallel,i}$-term in $\mathcal{C}_{ei}$. This indicates the importance of $U_{\parallel,i}$ in the parallel momentum balance equation of electrons if we would like to evaluate the correct bootstrap current, since the parallel friction $F_{\parallel,ei}$ is roughly proportional to $\langle BU_\parallel \rangle_i - \langle BU_\parallel \rangle_e$, that is, bootstrap current. On the other hand, the present benchmark result ensures that the neglect of $\mathcal{C}_{ie}$ in the parallel momentum balance equation of ions is valid for bootstrap current calculation.

Table B.1: Parameter for Benchmark of Local Drift-kinetic Model

$x \equiv r/a$	R_0[m]	a[m]	$B_0[T]$	ι	$n[\frac{1}{m^3}]$	$T[kev]$	$\frac{d}{dx}\ln n$	$\frac{d}{dx}\ln T$	$v_{th}[m/s]$
0.2950	2.35	0.47	1.90	0.97	9.22×10^{18}	1.84	-0.58	-0.58	5.94×10^{5}

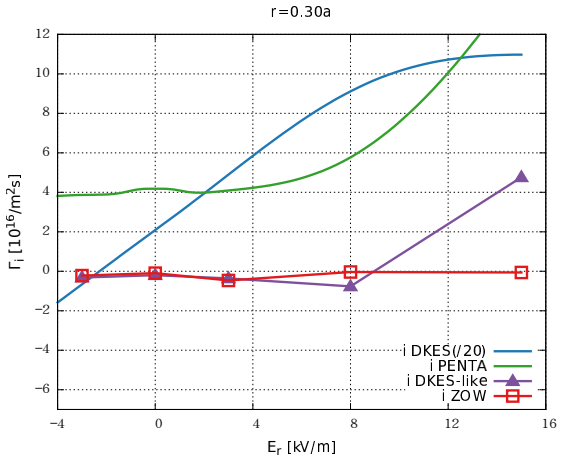

Figure B.1: The radial ion flux in the tokamak

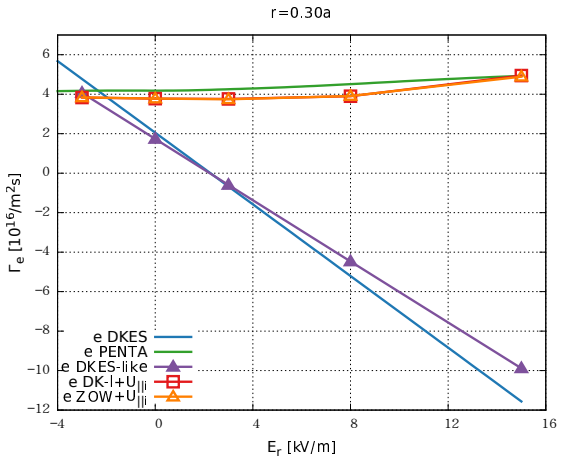

Figure B.2: The radial electron flux in the tokamak

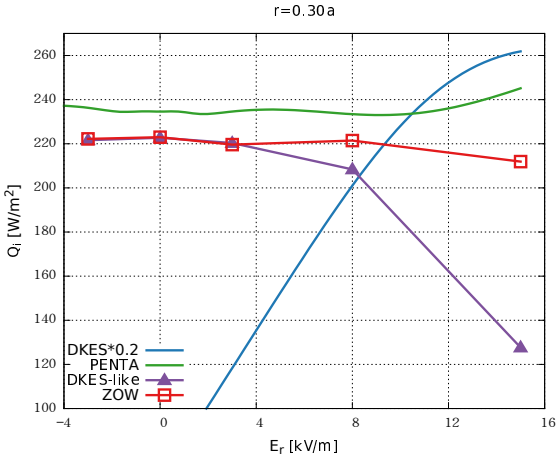

Figure B.3: The ion heat flux in the tokamak

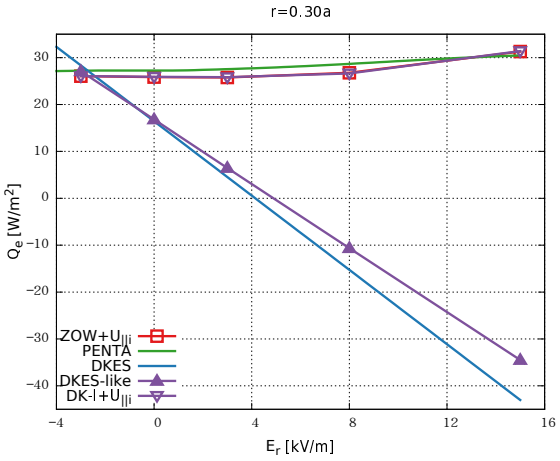

Figure B.4: The electron heat flux in the tokamak

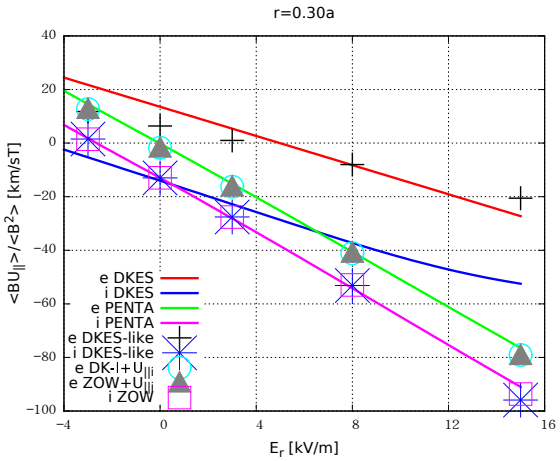

Figure B.5: The ion and electron parallel flows in the tokamak

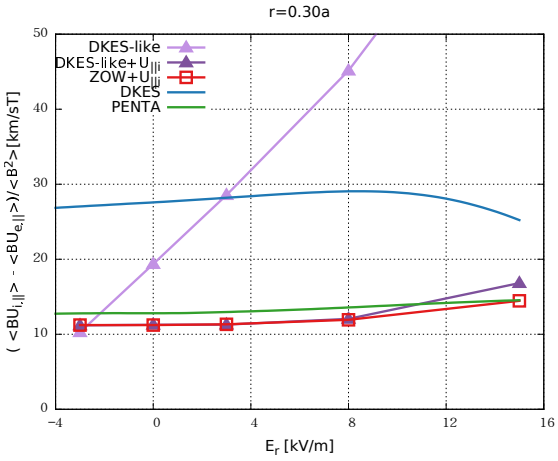

Figure B.6: The bootstrapt current in the tokamak

Bibliography

[1] F.S.B. Anderson, A.F. Almagri, D.T. Anderson, P.G. Matthews, J.N. Talmadge, and J.L Shohet. Helically symmetric experiment, (hsx) goals, design and status. Fusion Technology, 27:273–277, 1995.

[2] C D Beidler and W D D'haeseleer. A general solution of the ripple-averaged kinetic equation (gsrake). Plasma Physics and Controlled Fusion, 37(4):463, 1995.

[3] C D Beidler and H Maaßberg. An improved formulation of the ripple-averaged kinetic theory of neoclassical transport in stellarators. Plasma Physics and Controlled Fusion, 43(8):1131, 2001.

[4] C.D. Beidler, K. Allmaier, M.Yu. Isaev, S.V. Kasilov, W. Kernbichler, G.O. Leitold, H. Maaßberg, D.R. Mikkelsen, S. Murakami, M. Schmidt, D.A. Spong, V. Tribaldos, and A. Wakasa. Benchmarking of the mono-energetic transport coefficientsresults from the international collaboration on neoclassical transport in stellarators (icnts). Nuclear Fusion, 51(7):076001, 2011.

[5] S. I. Braginskii. Transport processes in a plasma. Reviews of Plasma Physics, 1:205, 1965.

[6] A Briesemeister, K Zhai, D T Anderson, F S B Anderson, and J N Talmadge. Comparison of the flows and radial electric field in the hsx stellarator to neo-

classical calculations. Plasma Physics and Controlled Fusion, 55(1):014002, 2013.

[7] A Briesemeister, K Zhai, D T Anderson, F S B Anderson, and J N Talmadge. Comparison of the flows and radial electric field in the hsx stellarator to neoclassical calculations. Plasma Physics and Controlled Fusion, 55(1):014002, 2013.

[8] J M García-Regaña, R Kleiber, C D Beidler, Y Turkin, H Maaßberg, and P Helander. On neoclassical impurity transport in stellarator geometry. Plasma Physics and Controlled Fusion, 55(7):074008, 2013.

[9] J. Geiger, C D Beidler, Y Feng, H Maaßberg, N B Marushchenko, and Y Turkin. Physics in the magnetic configuration space of w7-x. Plasma Physics and Controlled Fusion, 57(1):014004, 2015.

[10] S. Gori, W. Lotz, and J Nührenberg. Quasi-iosdynamic stellarators. In Theory of Fusion Plasmas (Proc. Joint Varenna-Lausanne Workshop, 1996), pages 335–342. Bologna: Editrice Compositori, 1997.

[11] T. Goto, J. Miyazawa, R. Sakamoto, R. Seki, C. Suzuki, M. Yokoyama, S. Satake, A. Sagara, and The FFHR Design Group. Integrated physics analysis of plasma start-up scenario of helical reactor ffhr-d1. Nuclear Fusion, 55(6):063040, 2015.

[12] T. Goto, J. Miyazawa, R. Sakamoto, Y. Suzuki, C. Suzuki, R. Seki, S. Satake, B. Huang, M. Nunami, M. Yokoyama, A. Sagara, and the FFHR Design Group. Development of a real-time simulation tool towards self-consistent scenario of plasma start-up and sustainment on helical fusion reactor ffhr-d1. submitted to Nuclear Fusion.

[13] G. Grieger, W. Lotz, P. Merkel, J. Nührenberg, J. Sapper, E. Strumberger, H. Wobig, R. Burhenn, V. Erckmann, U. Gasparino, L. Giannone, H. J. Hart-

fuss, R. Jaenicke, G. Kühner, H. Ringler, A. Weller, F. Wagner, the W7-X Team, and the W7-AS Team. Physics optimization of stellarators. Physics of Fluids B, 4(7):2081–2091, 1992.

[14] P. Helander and D.J. Sigmar. Collisional Transport in Magnetized Plasmas. Cambridge Monographs on Plasma Physics. Cambridge University Press, 2002.

[15] S. P. Hirshman, K. C. Shaing, W. I. van Rij, C. O. Beasley, and E. C. Crume. Plasma transport coefficients for nonsymmetric toroidal confinement systems. Physics of Fluids, 29(9):2951–2959, 1986.

[16] S.P Hirshman and O Betancourt. Preconditioned descent algorithm for rapid calculations of magnetohydrodynamic equilibria. Journal of Computational Physics, 96(1):99 – 109, 1991.

[17] Genze Hu and John A. Krommes. Generalized weighting scheme for delta-f particle-simulation method. Physics of Plasmas, 1(4):863–874, 1994.

[18] B. Huang, S. Satake, R. Kanno, H. Sugama, and T. Goto. Benchmark of the bootstrap current simulation in helical plasmas. accpeted for publication in Plasma and Fusion Research, 2017.

[19] B. Huang, S. Satake, R. Kanno, H. Sugama, and S. Matsuoka. Benchmark of the local drift-kinetic models for neoclassical transport simulation in helical plasmas. accpeted for publication in Physcis of Plasmas, 2017.

[20] S. Jolliet and Y. Idomura. Plasma size scaling of avalanche-like heat transport in tokamaks. Nuclear Fusion, 52(2):023026, 2012.

[21] Winfried KERNBICHLER, Sergei V. KASILOV, Georg O. LEITOLD, Viktor V. NEMOV, and Klaus ALLMAIER. Recent progress in neo-2 — a code for neoclassical transport computations based on field line tracing. Plasma and Fusion Research, 3:S1061–S1061, 2008.

[22] R.A. Kolesnikov, W.X. Wang, and F.L. Hinton. Unlike-particle collision operator for gyrokinetic particle simulations. Journal of Computational Physics, 229(15):5564 – 5572, 2010.

[23] M. Landreman, H. M. Smith, A. Mollón, and P. Helander. Comparison of particle trajectories and collision operators for collisional transport in nonaxisymmetric plasmas. Physics of Plasmas, 21(4), 2014.

[24] Z. Lin, W. M. Tang, and W. W. Lee. Gyrokinetic particle simulation of neoclassical transport. Physics of Plasmas, 2(8):2975–2988, 1995.

[25] Z. Lin, W. M. Tang, and W. W. Lee. Gyrokinetic particle simulation of neoclassical transport. Physics of Plasmas, 2(8):2975–2988, 1995.

[26] Robert G. Littlejohn. Variational principles of guiding centre motion. Journal of Plasma Physics, 29:111–125, 2 1983.

[27] J. Lore, W. Guttenfelder, A. Briesemeister, D. T. Anderson, F. S. B. Anderson, C. B. Deng, K. M. Likin, D. A. Spong, J. N. Talmadge, and K. Zhai. Internal electron transport barrier due to neoclassical ambipolarity in the helically symmetric experimenta). Physics of Plasmas, 17(5), 2010.

[28] H. Maaßberg, C. D. Beidler, and Y. Turkin. Momentum correction techniques for neoclassical transport in stellarators. Physics of Plasmas, 16(7), 2009.

[29] Seikichi Matsuoka, Shinsuke Satake, Ryutaro Kanno, and Hideo Sugama. Effects of magnetic drift tangential to magnetic surfaces on neoclassical transport in non-axisymmetric plasmas. Physics of Plasmas, 22(7):072511, 2015.

[30] Seikichi Matsuoka, Shinsuke Satake, Masayuki Yokoyama, Arimitsu Wakasa, and Sadayoshi Murakami. Neoclassical electron transport calculation by using δ f monte carlo method. Physics of Plasmas, 18(3):032511, 2011.

[31] Shinsuke SATAKE Yuji NAKAMURA Maxim Yu. ISAEV, Kiyomasa Y. WATANABE and Wilfred A. COOPER. Plasma and Fusion Research, 7:1403077, 2012.

[32] K. Miyamoto. Plasma Physics for Controlled Fusion. Science and Culture Publishing, 2012.

[33] S. Murakami, U. Gasparino, H. Idei, S. Kubo, H. Maassberg, N. Marushchenko, N. Nakajima, M. Romé, and M. Okamoto. 5-d simulation study of suprathermal electron transport in non-axisymmetric plasmas. Nuclear Fusion, 40(3Y):693, 2000.

[34] S. Satake, Y. Idomura, H. Sugama, and T.-H. Watanabe. Benchmark test of drift-kinetic and gyrokinetic codes through neoclassical transport simulations. Computer Physics Communications, 181(6):1069 – 1076, 2010.

[35] Shinsuke SATAKE, Ryutaro KANNO, and Hideo SUGAMA. Development of a non-local neoclassical transport code for helical configurations. Plasma and Fusion Research, 3:S1062–S1062, 2008.

[36] Shinsuke SATAKE, Masao OKAMOTO, Noriyoshi NAKAJIMA, Hideo SUGAMA, and Masayuki YOKOYAMA. Non-local simulation of the formation of neoclassical ambipolar electric field in non-axisymmetric configurations. Plasma and Fusion Research, 1:002–002, 2006.

[37] O. Sauter, C. Angioni, and Y. R. Lin-Liu. Neoclassical conductivity and bootstrap current formulas for general axisymmetric equilibria and arbitrary collisionality regime. Physics of Plasmas, 6(7):2834–2839, 1999.

[38] D. A. Spong. Generation and damping of neoclassical plasma flows in stellaratorsa). Physics of Plasmas, 12(5), 2005.

[39] D.A. Spong, S.P. Hirshman, J.F. Lyon, L.A. Berry, and D.J. Strickler. Recent advances in quasi-poloidal stellarator physics issues. Nuclear Fusion, 45(8):918, 2005.

[40] H. Sugama and W. Horton. Neoclassical electron and ion transport in toroidally rotating plasmas. Physics of Plasmas, 4(6):2215–2228, 1997.

[41] H. Sugama, S. Matsuoka, S. Satake, and R. Kanno. Radially local approximation of the drift kinetic equation. Physics of Plasmas, 23(4), 2016.

[42] H. Sugama and S. Nishimura. How to calculate the neoclassical viscosity, diffusion, and current coefficients in general toroidal plasmas. Physics of Plasmas, 9(11):4637–4653, 2002.

[43] M. Taguchi. A method for calculating neoclassical transport coefficients with momentum conserving collision operator. Physics of Fluids B, 4(11):3638–3643, 1992.

[44] V. Tribaldos, C. D. Beidler, Y. Turkin, and H. Maaßberg. Extended estimations of neoclassical transport for the tj-ii stellarator: The bootstrap current. Physics of Plasmas, 18(10), 2011.

[45] V Tribaldos and J Guasp. Neoclassical global flux simulations in stellarators. Plasma Physics and Controlled Fusion, 47(3):545, 2005.

[46] W. I. van Rij and S. P. Hirshman. Variational bounds for transport coefficients in threedimensional toroidal plasmas. Physics of Fluids B, 1(3):563–569, 1989.

[47] K. Watanabe, N. Nakajima, M. Okamoto, Y. Nakamura, and M. Wakatani. Nuclear Fusion, 32(9):1499, 1992.

[48] M. Yokoyama, S. Matsuoka, H. Funaba, K. Ida, K. Nagaoka, M. Yoshinuma, Y. Takeiri, O. Kaneko, and LHD Experiment Group. Considerations from the viewpoint of neoclassical transport towards higher ion temperature heliotron plasmas. Contributions to Plasma Physics, 50(6-7):586–589, 2010.

[49] M. Yokoyama, N. Nakajima, M. Okamoto, Y. Nakamura, and M. Wakatani. Roles of bumpy field on collisionless particle confinement in helical axis heliotrons. Nuclear Fusion, 40(2):261, 2000.